A VISCOELASTIC-VISCOPLASTIC ANALYSIS OF FIBER REINFORCED POLYMER COMPOSITES UNDERGOING MECHANICAL LOADING AND TEMPERATURE CHANGES

A Dissertation

by

JAEHYEUK JEON

Submitted to the Office of Graduate Studies of
Texas A&M University
in partial fulfillment of the requirements for the degree of

DOCTOR OF PHILOSOPHY

Chair of Committee,	Anastasia H. Muliana
Committee Members,	Debjyoti Banerjee
	Junuthula N. Reddy
	Stefan Hurlebaus
	Terry Creasy
Head of Department,	Andreas A. Polycarpou

August 2013

Major Subject: Mechanical Engineering

ABSTRACT

This study presents a combined viscoelastic (VE)-viscoplastic (VP) analysis for Fiber Reinforced Polymer (FRP) composites subject to simultaneous mechanical load and conduction of heat. The studied FRP composites consist of unidirectional fibers, which are considered as linearly elastic with regards to their mechanical response, and isotropic polymeric matrix, which shows viscoelastic-viscoplastic response under various stresses and temperatures. Due to the viscoelastic and viscoplastic behavior of the polymeric matrix, the overall FRP composites exhibit a combined time-dependent and inelastic behavior. A simplified micromechanical model, consisting of a unit-cell with four fiber and matrix subcells, is formulated to homogenize the overall heat conduction and viscoelastic-viscoplastic responses of the FRP composites. The micromechanical model is compatible with a displacement based finite element (FE) and is implemented at the Gaussian integration points within the continuum finite elements, which is useful for analyzing the overall time-dependent response of FRP composite structures under various boundary conditions. The Schapery nonlinear integral model combined with the Perzyna viscoplastic model is used to describe the viscoelastic-viscoplastic response of the polymer constituents. An integrated time integration algorithm is formulated at the micromechanics level in order to solve the nonlinear viscoelastic-viscoplastic constitutive model at the matrix subcells and obtain the overall nonlinear response of the FRP. The viscoelastic-viscoplastic micromechanical model is validated using experimental data on off-axis glass/epoxy FRP composites available in literature. The

overall response of the FRP composites determined from the simplified micromechanical model is also compared with the ones generated from microstructures of FRP with various fiber arrangements dispersed in homogeneous polymer matrix. The microstructural models of the FRP with detailed fiber arrangements are generated using FE. The effects of thermal stresses, due to the mismatches in the coefficient of thermal expansions of the fibers and polymeric matrix, and stress concentrations/discontinuities near the fiber and matrix interfaces on the overall thermo-mechanical deformation of FRP composites are studied using the two micromechanical models discussed above. Finally, an example of structural analysis is performed on a polymeric smart sandwich composite beam, having FRP skins and polymeric foam core with piezoelectric sensors integrated to the FRP skins, undergoing three point bending at an elevated temperature. The creep displacement is compared to experimental data available in literature.

DEDICATION

To my wife, Jeeyoung, and my family

ACKNOWLEDGEMENTS

"It is a pleasure to thank those who made this dissertation possible."

I am not certain that many graduate students are given the opportunity to have such precious advisors, mentors, and professors as I have had during my years earning a Ph.D.

First of all, I would like to thank my advisor, Dr. Muliana for her support and good feedback. After Dr. Morgan passed away, Dr. Creasy filled my advisor position and updated my research carrier by giving me several opportunities to do continuing project. After then, Dr. Muliana guided me to the field of computational mechanics. I appreciate her patience and wise guidance since then. I remember her providing me with a good advice in every meeting since 2010. She supports her students in creating and reaching their dreams by supporting their academic research.

I am heartily thankful to my committee members, Dr. Creasy, Dr. Reddy, Dr. Debjyoti, and Dr. Hurlebaus, whose encouragement, supervision, and support from the preliminary to the concluding level enabled me to develop an understanding of my research. They offered sharp insight on my dissertation and guided me with very useful information for updating my research.

I also thank Dr. Jeongsik Kim for his guidance to ABQUS and UMAT. When I begin this research, he taught me every detailed computational skill which makes me to succeed in my research topic.

I thank my parents for showing their faith in me by allowing me to pursue my dreams and providing me with all the support I needed to achieve them. I'm grateful to my father- and mother-in-law for always wishing the best for me. I also thank my uncle- and aunt-in-law in Oklahoma. They endured and survived the experience of graduate school and provided me with unending encouragement and support.

Finally, and most importantly, I would like to thank my wife, bible teacher and best friend, Jeeyoung. Her support, encouragement, quiet patience and unwavering love were undeniably the bedrock upon which the past six years of my life have been built. She was always there for me when I needed her. I also thank my children, Chowon, Sheenae, and Euiro for their love.

Lastly, I offer my regards and blessings to all those who supported me in any respect during the completion of this research. Whenever I felt depressed and confronted many challenges, I heard a voice that said, "I'll be there for you!" This voice came from my professors and friends. For everything you've done for me, I thank you.

NOMENCLATURE

BVP	Boundary Value Problem
CTE	Coefficient of Thermal Expansion
FE	Finite Element
FRP	Fiber Reinforced Polymer
FVF	Fiber Volume Fraction
GFRP	Glass Fiber Reinforced Polymer
HDPE	High Density Polyethylene
MOC	Method of Cells
PVC	Polyvinylchloride
PZT	Lead Zirconium Tinanate
RVE	Representative Volume Element
TCM	Thermo-rheologically Complex Material
TSM	Thermo-rheologically Simple Material
TTSP	Time-Temperature Superposition Principle
UC	Unit Cell
UV	Ultra Violet Ray
UEXPAN	User Subroutine to Define Incremental Thermal Strains
UMAT	User Subroutine to Define a Material's Mechanical Behavior
UMATHT	User Subroutine to Define a Material's Heat Transfer
V_f	Fiber Volume Fraction

VE	Viscoelastic
VP	Viscoplastic
WPC	Wood-Polypropylene Composite

TABLE OF CONTENTS

Page

LIST OF FIGURES

Page

LIST OF TABLES

CHAPTER I

INTRODUCTION

It was in the early 1940's that the development of Fiber Reinforced Polymer (FRP) composites began and till date they continuously have an important role in the development of advanced structures. The characteristics of FRP composites, which are lightweight, high stiffness and strength to weight ratios, good resistance to fatigue failure, and easily customized to meet desired performances, make them appealing in various engineering applications such as automobile, naval and aerospace structures, and sporting goods. FRP composites are also used for the main and secondary components of the civil infrastructures, such as storage tank, grating, retrofitting bridge, pipe, etc., which can reduce the overall weight of the structures. It is noted that the weight density of FRP composites is about 20% of that of steel and 60% of the weight density of concrete. Moreover, the excellent corrosion resistance of the FRP composites makes the FRP composite structures capable of resisting hostile environmental conditions such as extreme moistures and chemical reactions. Recent applications could also subject the FRP composites to various temperature changes: low to elevated temperatures such as in the wind power plant and turbine blades. Despite the enormous applications of the FRP composites, there are still challenges in designing and analyzing structures comprising of FRP composites especially when they are undergoing significant nonlinear time-dependent effects coupled with hostile environmental conditions.

FRP composites consist of two or more different kinds of materials (constituents), and they are orthotropic, or at least transversely isotropic, with regards to their mechanical and physical properties. When subjected to external mechanical and non-mechanical stimuli, the response of FRP composites depends strongly on the microstructural characteristics of the FRPs, i.e., fiber arrangements, compositions, and properties of the constituents, and directions of loading. FRP composites consisting of epoxy matrix show a pronounced time-dependent behavior due to the viscoelastic nature of the polymers. When these composites are subjected to high mechanical loadings and elevated temperatures, the polymeric matrix could experience an inelastic (viscoplastic) deformation, leading to time-dependent and inelastic overall response of the FRP structures. Furthermore, the time-dependent and inelastic response becomes more significant when the FRP is subjected to off-axis mechanical loadings due to the additional shear effect presence in the composites.

This study presents a micromechanical model for analyzing time-dependent and inelastic response of FRP composite materials and structures subject to various external mechanical and thermal stimuli. The micromechanical model is used to homogenize the response of FRP composites. The Fourier law is assumed to govern the conduction of heat through the composites. The Schapery nonlinear integral model is used for the viscoelastic response and is combined with the Perzyna viscoplastic model for the polymeric matrix. This time-dependent and inelastic homogenized response is integrated with finite element (FE) and used for analyzing and designing FRP structural components. The advantages of micromechanical modeling approaches are: they allow

incorporating microstructural characteristics in predicting overall response of composites, they are capable of determining nonlinear and inelastic response of the constituents due to the prescribed external stimuli, and they can provide a rigorous and robust prediction of the complex nonlinear response of the FRP composites.

This chapter presents a literature review of viscoelastic (VE) and viscoplastic (VP) response of polymers and FRP composites including the temperature effect. Micromechanics modeling approaches, which are one of the important aspects in this study, are also reviewed. Finally, the motivation and objectives of this research are discussed.

1.1. Literature Review

1.1.1 Existing studies on VE-VP response of polymers

Polymeric based FRP composites, when subjected to mechanical loading coupled with temperature and moisture changes, show an elastic behavior (instantaneous response) and significant viscous behavior (delayed response) due to the existence of the polymer matrix. Polymeric materials often exhibit viscoelastic (VE) solid response when subjected to mechanical loading. The response can be linear or nonlinear[1] depending on the severity of the loads and environmental conditions. Upon removal of the mechanical loads, the viscoelastic polymers could undergo fully recovery when sufficient time is given. However, it is also possible that in addition to the viscoelastic response the

[1] The linear response is considered when the proportionality and superposition between the input and the corresponding response can be made, otherwise the response is considered nonlinear.

polymers can experience plastic (viscoplastic, VP) deformations. Under such condition, removal of the mechanical loading leads to a permanent deformation.

There have been experimental and theoretical studies on understanding the VE and combined VE-VP behaviors of polymers. Creep-recovery tests have been conducted on polyurethane (Lai and Findley, 1973), oriented polypropylene monofilament (Ward and Onat, 1963), FM-73 polymer (Peretz and Weitsman, 1982, 1983), and Hercules 3502 epoxy resin (Harper and Weitsman, 1985) under various loading histories and isothermal conditions. The results show that the above polymers experience nonlinear viscoelastic behaviors in which the nonlinearity becomes more pronounced at higher stresses and elevated temperatures. Recent experimental studies of polyimide resins show nonlinear viscoelastic response at elevated temperatures (Bhargava, 2007; Falcone and Ruggles-Wrenn, 2009). It has also been observed that long-term exposure to elevated temperatures could lead to oxidation in the polymers. Creep-recovery tests performed on some polymers such as high-density polyethylene, HDPE, (Lai and Bakker, 1996), polycarbonate (Frank 1998), and aramid and polyester fibers (Chailleux and Davies, 2003, 2005) show combined VE and VP responses. The experiments were performed on relatively short period (30 minutes) at different stress levels and room temperature (293K). The response of the polymers depends on the magnitude of the applied stresses.

Constitutive models for VE response of isotropic materials with small and large deformation gradients has been developed based on the classical mechanics and thermodynamics framework; for examples the modified superposition principle (Findley

and Lai, 1967), multiple integral model (Green and Rivlin 1957), finite strain integral models (Pipkins and Rogers 1968), single integral models (Pipkins and Rogers 1968; Schapery 1969), thermo-mechanical theory of nonlinear viscoelastic model under non-isothermal condition (Coleman ,1964). Constitutive models for combined linear VE and plastic behaviors based on an overstress function have been formulated by Landau et al. (1960), Naghdi and Murch (1963), Drozdov (1999). The VE strain rates are time and loading history dependent, and the plastic strain rates depend only on loading path histories. Constitutive models for coupled linear elastic and VP behaviors have also been proposed such as over-stress rate-dependent plasticity, Perzyna (1966, 1971), Perzyna and Wojno (1975), Bodner and Partom (1975), and endochronic VP model based on an irreversible thermodynamics, Valanis et al. (1971). The Perzyna model has been used to predict the VP behavior of aramid and polyester fibers by Chailleux and Davies (2003, 2005). Recently, VP constitutive models of polymers based on an overstress function with nonlinear rate dependent have been proposed by Krempl and Ho (2000), Colak (2005), Hall (2005). Modeling combined VE-VP behaviors of polymers has been done by Schapery (1997), Frank and Brockman (2001), Drozdov and Christiansen (2008). The constitutive models in the above studies are described in terms of stress, temperature, moisture, time, and internal state variables. The internal state variables are attributed to the VE and VP strains.

Depending on the complexity of the time-dependent and inelastic constitutive models and prescribed boundary conditions, it might not be possible to obtain closed form analytical solutions of time-dependent field variables. It is due to this reason

several numerical techniques have been proposed in order to determine approximate solutions of boundary value problems involving time-dependent and inelastic material response. Several numerical algorithms have been formulated for solving the Schapery VE integral equations, such as Henriksen (1984), Lai and Bakker (1996), Kennedy (1998), Poon and Ahmad (1999), Haj-Ali and Muliana (2004), Muliana and Khan (2008) and Sawant and Muliana (2008). Zienkiewicz and Cormeau (1972, 1974), Wang et al. (1997), Simo and Hughes (1998), and Heeres et al. (2002) presented several numerical algorithms of linear elastic-VP Perzyna constitutive models. An integration algorithm within FE framework for a combined Schapery nonlinear VE and Perzyna VP model has been formulated by Kim and Muliana (2009). The semi-analytic integration method has been proposed by Hirsekorn et al. (2011) for solving the creep response of nonlinear viscoelastic and viscoplastic materials. In the above model, the nonlinearity is defined in terms of stress inputs and the Prony series expansion is used for the creep function. The proposed integration scheme is robust and stable for predicting VE-VP behaviors of materials for a wide range of retardation times.

1.1.2 Existing studies on VE-VP response of FRP composites

Unidirectional fibers merely show linearly elastic behaviors with a relatively high stiffness compared to the polymer matrix, which exhibits VE or combined VE-VP responses. When a unidirectional FRP composite is subjected to a mechanical load along the longitudinal fiber direction, the overall response of the FRP composites show mainly linearly elastic behavior with negligible nonlinearity or inelasticity. When off-axis

loadings are considered the overall response can show significant VE or combined VE-VP behaviors. Moreover, temperature, moisture, and aging effects can intensify the nonlinear time-dependent and inelastic response of the FRP composites.

Lou and Schapery (1971) have conducted uniaxial tensile creep-recovery tests on off-axis glass fiber-epoxy composites under isothermal conditions. The creep tests were performed at several stress levels with regards to the ultimate strength of the specimens. The results showed nonlinear viscoelastic behaviors for the off-axis specimens, which were modeled using a power law time-dependent function. The material parameters were calibrated for each off-axis specimens and stress levels. Dillard et al. (1987) analyzed nonlinear creep response of T300/934 FRP composites. The power law time-dependent function was used to fit the experimental data. Creep-recovery tests on graphite/epoxy T300/5208 composites with various fiber angles were conducted by Tuttle and Brinson (1986). The Schapery integral model was used to predict the long-term creep response of T300/5280.

Guedes and Marques (1998) reported an experimental work under creep-recovery, ramp loading and multiple relaxation tests on T300/5208 and IM7/5260 composites. They used the Schapery VE model and Zapas and Crissman VP model to predict the experimental results. It was reported that the results of analytical solutions have a good agreement with the experimental results. Megnis and Varna (2002) characterized time-dependent and inelastic response of glass-epoxy FRP composites from creep-recovery tests under isothermal condition. They compared the experimental results with analytical solutions. The difference between the creep strains obtained from

the experimental results of the off-axis specimens and predicted linear VE strains shows that the FRP composite experienced VP deformation. It was reported that the VP response is pronounced for the off-axis creep tests due to high shear stresses.

1.1.3 Temperature effects on viscoelastic FRP composites

The response of FRP composites depends also on the temperatures and other environmental factors such as moisture, aging, chemical reaction, and UV. High temperatures could degrade the properties of composites and the creep deformation (or relaxation stress) in FRP composites change with temperatures. Elevated temperatures accelerate the relaxation and creep in the polymer FRP composites. The time-dependent response of materials at various temperatures can be classified as thermo-rheologically simple (TSM) and thermo-rheologically complex materials (TCM). For TSM materials, the effect of temperature on the viscoelastic response can be incorporated through a time-scale shift factor since the temperature is assumed to affect only the transient part of the stress relaxation or creep deformation. For TCM materials, it was suggested that temperature changes alter the molecular structures of the polymers and influence the instantaneous, transient, and relaxed (equilibrium) moduli (and compliances) of the materials, Harper and Weitsman (1985); Caruthers and Cohen (1980); Wineman and Rajagopal (2000).

Tuttle et al. (1995) conducted cyclic thermo-mechanical loading tests on graphite-bismaleimide (IM7/5260) composites at various stress levels and temperatures. The experiment on the multi-angle composite laminate was done under a 50-hr cyclic

loading and isothermal conditions. The results showed nonlinear VE-VP responses under high temperature and stress levels. The experimental data were compared with the response obtained using the Schapery nonlinear VE integral model and VP functional proposed by Zapas and Crissman (1984). Experimental characterization on AS4/PEEK semi-crystalline polymer matrix composites (Wang et al., 1997) shows that the composite experiences elastic-VP behavior under thermo-mechanical loading. Tuttle, Pasricha, and Emery (1993) predicted the long-term response of IM7/5260 composites under cyclic thermo-mechanical loadings. Schapery's nonlinear VE model and a functional VP model were used to predict the time-dependent response under the long-term cyclic thermo-mechanical loading.

Muddasani et al. (2010) conducted creep tests to examine the nonlinear VE response of E-glass/polyester multi-layered composites at various temperatures: 227.4K-221.3K and stress levels: 0.2-0.6 of the ultimate tensile stress. The creep tests were performed on the uniaxial, transverse and 45^{o} off-axis specimens. The results show that creep behavior is more pronounced in the off- axis specimens under elevated temperatures. The nonlinearity in the specimens increases with increasing temperatures. They also analyzed the nonlinear VE response of the multilayered composites with temperature effect and showed that the studied composites belong to the TCM material. Chien and Tzeng (1993) investigated the thermal effect on the VE behavior of thick-walled composite cylinders. The VE response depends on the material properties, fiber orientations, and temperatures. It was concluded that the off-axis specimens experience significant VE response. The VE behavior of cylinders subjected to a uniform

temperature difference of 423K, which is below the glass transition temperature, 443K, is studied. Tamrakar et al. (2011) have studied time and temperature dependence on an extruded wood-polypropylene composite (WPC). The response is compared with the one of polyvinylchloride (PVC). The quasi-static and creep tests subjected to various temperatures were conducted and the degradation in the mechanical properties under elevated temperatures was characterized. Time-temperature superposition was also applied to predict the long-term creep response of both materials and the result shows the long-term creep compliance of WPC is incredibly higher than that of PVC.

Zhang and Hartwig (1997) investigated VE behavior of AS4/PEEK FRP composites subjected to low temperature under cyclic loading. The damping behavior depends mainly on the matrix properties. Mivehchi and Varvani-Farahani (2011) studied fatigue lives of FRP composites under various temperatures. The results show that temperature significantly influences the mechanical properties of FRP composites. Bradshaw and Brinson (1999) predicted the mechanical response of composite laminates under non-isothermal and aging effects. The hygrothermal strains were significantly high at early time and decreased as steady state condition is reached. Sawant and Muliana (2008) formulated a numerical algorithm for predicting overall nonlinear viscoelastic response of orthotropic materials. The nonlinearity was due to stresses and temperatures suitable for TCM materials. They used the numerical algorithm to predict thermo-viscoelastic response of various FRP composites under various fiber volume fractions, fiber orientations, and temperatures. Recent studies by Miyano et al. (2008), Nakada and Miyano (2009) and Cai et al. (2010) consider the coupled time-temperature effect on the

creep and fatigue behaviors of various fiber reinforced polymer (FRP) laminated composites and a honeycomb sandwich composite under bending. They adopted the time-temperature superposition principle (TTSP), coined to Leaderman (1943) and thermo-rheologically simple materials as per Schwartz and Staverman (1952), to obtain the long-term overall response of the composites by shifting the short-term creep/cyclic response at various environmental conditions.

1.1.4 Micromechanical models of FRP composite material

Various micromechanical models have been developed to predict the overall response of FRP composites with complex microstructural geometry. In this study, the micromechanical modeling approaches are classified into two groups. The first micromechanical modeling approach deals with obtaining the overall response of composites based on simplified microstructural characteristics, in which a representative volume element (RVE) of the composite is considered as the smallest unit-cell that can give a reasonable prediction. The size of RVE based on this approach depends on the responses being examined, i.e., elastic, plastic (Kouznetsova et al., 2001, Suquet, 1985). The second micromechanical modeling approach considers a RVE of the composite as a domain containing all possible microstructural configurations that exist in the composite. This concept can be employed by discretizing the microstructural model based on experimentally obtained microstructural images, see for example Shan and Gokhale (2002), and the overall response can be obtained by solving boundary value problems

(BVPs) using for example FE. This approach leads to a relatively large RVE and high computational costs, especially for nonlinear multi-field problems.

Several homogenized models, following the first micromechanical modeling approach, have been proposed; many of them are for linearly elastic response. A rule of mixture based on a uniform strain constraint of the composite was proposed by Voigt (1887), while rule of mixture based on a uniform stress constraint of the composite was considered by Reuss (1929). Several other micromechanical models for predicting linear elastic response in composites are: dilute-distribution method by Eshelby (1957), self-consistent model which uses a concept of effective medium theory and determines the mechanical properties of composites for infinite media by Hershey (1954), Kroner (1958), Budiansky and Wu (1962) and Hill (1965), concentric cylinder assemblage (CCA) method that describes cylindrical fibers surrounded by cylindrical matrix medium by Hashin and Rosen (1964), and the Mori-Tanaka method which is based on the Eshelby elasticity solution for incorporating inhomogeneity in an infinite medium and uses the average strains in the constituents caused by the fiber interaction effects by Mori and Tanaka (1973).

The above micromechanical models have been extended to predict elastic and inelastic responses of FRP. Budiansky (1965), Hill (1965), Walpole (1969) used the self-consistent model to study an elastic behavior of fibrous composites. Rosen and Hashin (1970) extended Levin's model of general anisotropic composites by using a variational approach. Laws (1973) studied thermo-elasticity problem in anisotropic composites using Hill's self-consistent approximation. Laws and Mclaughlin (1978) applied the self-

consistent method and a numerical inversion method to analyze viscoelastic response of particulate and fibrous composites. Dvorak and Bahei-El-Din (1979) used the self-consistent model to analyze elastic-plastic response of fibrous composites. Christensen and Lo (1979) proposed a three-phase cylindrical model of unidirectional FRP composites to analyze the effective mechanical properties. The Mori-Tanaka micromechanical model has been modified to derive the effective VE properties of three-phase composite and used to predict the VE response of FRP composites by Fisher and Brinson (2001).

A method of cells (MOC), 3D nonlinear micromechanical models, was developed by Aboudi (1991) to evaluate the effective elastic and plastic responses of FRP composites comprising of periodical rectangular fibers surrounded by matrix. Sadkin and Aboudi (1989) used the MOC with four-cell micromechanical model to analyze temperature effects on the VE response of unidirectional FRP composites. The MOC was then used by Haj-Ali and Pecknold (1996) to formulate a new numerical scheme of a simplified unit-cell model for fiber reinforced composites, derived from periodically distributed microstructures. Haj-Ali and Muliana (2003, 2004) extended the simplified unit-cell micromechanical model for modeling the time dependent behavior of FRP. Till date, limited micromechanical models for a combined time-dependent and inelastic response of FRP composites have been proposed. Aboudi (2005) has developed a micromechanical model to predict the VE-VP responses of multiphase materials. The VE-VP model developed by Frank and Brockman (2001) is implemented in the multiphase composites. Matsuda and Ohno (2011) presented a micromechanical model

for analyzing elastic-VP response of unidirectional and woven laminated composites. Representative unit-cell models were selected and FE meshes were generated on the selected unit-cells. An elasto-VP constitutive model for an isotropic material was used for the polymer matrix and a linear elastic transversely isotropic model was used for the fibers.

1.2 Motivation and Research Objective

Current studies have shown that FRP composites exhibit pronounced VE responses that strongly depend on temperatures. Most of studies concerning the effects of temperatures on the overall responses of FRP are done under isothermal conditions, neglecting the effect of thermal stresses due to temperature changes on the overall performance of the composites. During their service, most FRP composite structures experience continuous cycles of temperature changes in addition to mechanical loadings. However, understanding the time-dependent performance in FRP composite structures when the properties and responses of the constituents in the FRP composites change due to conduction of heat is currently lacking. FRP composites could undergo coupled VE-VP responses when subjected to relatively high mechanical loading; and only limited studies have considered the combined VE-VP responses of FRP composites.

The current study deals with the analysis of VE-VP behaviors of unidirectional FRP composites in which the response of the polymeric matrix depend on stresses and temperatures. A VE-VP micromechanical model of the FRP composite is developed based on a simplified unit-cell model consisting of four fiber and matrix subcells. The

Schapery nonlinear integral model is used for the VE response and is combined with the Perzyna VP model in order to describe the VE-VP response of polymeric matrix. A time integration algorithm is formulated at the micromechanics level in order to solve the nonlinear VE-VP constitutive model at the matrix subcells and obtain the overall nonlinear response of the FRP. The micromechanical model is compatible with a displacement based FE and can be used to analyze the VE-VP response of FRP composite structures. In order to verify the simplified micromechanical model FE meshes comprising of detailed fiber arrangements dispersed in a homogeneous and continuous polymeric matrix are generated. The response obtained from the detailed FE meshes is compared to the one obtained from the simplified micromechanical model. Furthermore, experimental data on the combined VE-VP response of FRP composite reported by Megnis and Varna (2002) are used to validate the simplified micromechanical model.

The above simplified micromechanical model is modified to determine the overall thermal expansion coefficient, thermal conductivity, and heat capacity of the FRP composites. The simplified micromechanical model with thermo-mechanical coupling effects is then integrated to FE framework and used to analyze coupled transient heat conduction and deformation in FRP composite structural components. The purpose is to examine the effect of temperatures and thermal stresses on the VE-VP behaviors of FRP composite

This dissertation consists of the following components: Chapter II presents a constitutive model for the combined VE-VP response of isotropic polymers. The effect

of temperatures on the overall VE-VP response is also studied. Chapter III discusses a simplified micromechanical model for analyzing VE-VP response of FRP composites. Chapter IV discusses a simplified micromechanical model incorporating the temperature effect. Sequentially coupled heat transfer and deformation in FRP composites is studied. Chapter V presents analyses of composite structures, i.e., sandwich composite beams having FRP laminated composite skins and polymeric foam core, undergoing heat conduction and mechanical loading. The integrated micromechanical model and FE framework is used for the analyses. Finally, summary, recapitulation of the present study and future works are discussed in Chapter VI.

CHAPTER II

COMBINED VISCOELASTIC-VISCOPLASTIC CONSTITUTIVE MODEL FOR ISOTROPIC POLYMERIC MATERIALS*

This chapter presents a constitutive model for a combined viscoelastic (VE) and viscoplastic (VP) response of isotropic polymeric material based on a small displacement gradient (linearized strain) theory. The nonlinear Schapery integral model is used for the VE part and the Perzyna model is considered for the VP component; thus the nonlinearity is due to the stress-dependent material parameters. In addition, the material parameters are allowed to vary with temperatures. The combined VE-VP constitutive model is solved numerically, which is compatible with a displacement based FE and is integrated to the simplified micromechanical model for FRP composites (discussed in Chapter III). A brief discussion on the VE-VP numerical algorithm, which has been developed by Kim and Muliana (2009), is presented in this chapter. In this study, the VE-VP numerical algorithm is modified to incorporate the temperature effect. Parametric studies on the effect of temperatures on the overall VE-VP response of polymers are also presented.

---

* Reprinted with permission from Jaehyeuk Jeon, Anastatia Muliana, "A Simplified Micromechanical Model for Analyzing Viscoelastic-Viscoplastic Response of Unidirectional Fiber Composites", J. Eng. Mater. Technology, DOI:10.1115/1.4006508, 2012, Copyright 2012 by ASME

2.1 Viscoelastic-viscoplastic Constitutive Model

In a small displacement gradient problem, the total strains and incremental strains can be additively decomposed into the VE, VP, and thermal components:

$$\begin{aligned}
&\varepsilon_{ij}^{t} = \varepsilon_{ij}^{ve,t} + \varepsilon_{ij}^{vp,t} + \varepsilon_{ij}^{th,t} \\
&\Delta\varepsilon_{ij}^{t} = \Delta\varepsilon_{ij}^{ve,t} + \Delta\varepsilon_{ij}^{vp,t} + \Delta\varepsilon_{ij}^{th,t} \qquad \forall\ t \geq 0 \\
&\varepsilon_{ij}^{t} = \varepsilon_{ij}^{t-\Delta t} + \Delta\varepsilon_{ij}^{t} \\
&= \varepsilon_{ij}^{ve,t-\Delta t} + \Delta\varepsilon_{ij}^{ve,t} + \varepsilon_{ij}^{vp,t-\Delta t} + \Delta\varepsilon_{ij}^{vp,t} + \varepsilon_{ij}^{th,t-\Delta t} + \Delta\varepsilon_{ij}^{th,t}
\end{aligned} \tag{2.1}$$

where the superscripts *ve*, *vp* and *th* denote the VE, VP, and thermal components, respectively, and Δ indicates the incremental component. Here, the time-dependence of variables is denoted with superscript of the time *t*. Thus, $\varepsilon_{ij}^{ve,t}$ and $\varepsilon_{ij}^{vp,t}$ are the VE and VP strains at current time *t*, respectively $\Delta\varepsilon_{ij}^{ve,t}$ and $\Delta\varepsilon_{ij}^{vp,t}$ are the incremental form of VE and VP strains at current time *t*, respectively. The current total mechanical strain is described in terms of the VE and VP components. An example of a uniaxial strain response during a creep-recovery history is illustrated in Figure 2.1. During creep, the elastic and plastic deformations are allowed to increase with time and upon removal of the mechanical stress only the elastic component of strain is recoverable, resulting in a residual (permanent) strain. The permanent strain after complete recovery is equal to the total VP strain accumulated during loading until time t_1.

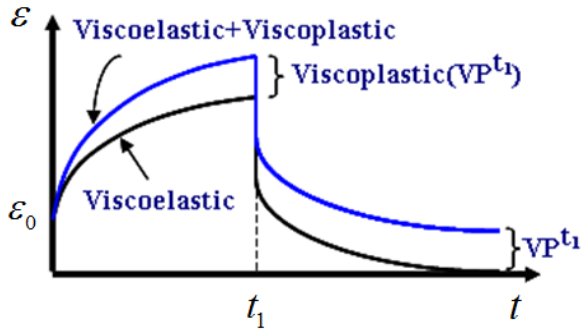

Figure 2.1 VE and VP strain response due to a creep-recovery loading history

The incremental thermal strain is given by $\Delta\varepsilon_{ij}^{th,t} = \alpha(T^t - T^{t-\Delta t})\delta_{ij}$, where α, T^t, and δ_{ij} are the linear coefficient of thermal expansion (CTE), temperature field at current time and Kronecker delta, respectively. In this study, we assume the constituents to be isotropic; thus, the CTE becomes a scalar quantity. The values of CTE can also vary with temperatures. In order to reduce complexity, the present study neglects the dissipation of energy from the VE and VP deformations so that the temperature changes in the body are due to the prescribed external thermal stimuli.

A nonlinear single-integral constitutive equation (Schapery, 1969), which is used for the VE component, is modified for a multi-axial loading. The current total VE strain consists of the deviatoric and volumetric strain components, written as

$$\varepsilon_{ij}^{ve,t} = e_{ij}^{ve,t} + \frac{1}{3}\delta_{ij}\varepsilon_{kk}^{ve,t} \tag{2.2}$$

$$e_{ij}^{ve,t} = \frac{1}{2}g_0(\bar{\sigma}^t, T^t)J_0 S_{ij}^t + \frac{1}{2}g_1(\bar{\sigma}^t, T^t)\int_0^t \Delta J^{(\psi^t - \psi^\tau)}\frac{d[g_2(\bar{\sigma}^\tau, T^t)S_{ij}^\tau]}{d\tau}d\tau \tag{2.3}$$

$$\varepsilon_{kk}^{ve,t} = \frac{1}{3}g_0(\bar{\sigma}^t, T^t)B_0\sigma_{kk}^t + \frac{1}{3}g_1(\bar{\sigma}^t, T^t)\int_0^t \Delta B^{(\psi^t - \psi^\tau)}\frac{d[g_2(\bar{\sigma}^\tau, T^t)\sigma_{kk}^\tau]}{d\tau}d\tau \tag{2.4}$$

J_o and B_o are the instantaneous elastic shear and bulk compliances, respectively. ΔJ and ΔB are transient shear and bulk compliances, respectively. The nonlinear parameters g_0, g_1, and g_2 are dependent on the current effective stress $\bar{\sigma}^t$ and temperature T^t. In the linear VE responses, g_0, g_1, and g_2 are unit, and stress-strain based constitutive equations can be interchanged. The above constitutive equations are suitable for small deformation gradient problems. In order to reduce the complexity in terms of calibrating time-dependent parameters, the corresponding linear elastic Poisson's ratio, ν, is taken as constant. The shear and bulk compliances are:

$$\begin{aligned} J_0 &= 2(1+\nu)D_0 \quad , & B_0 &= 3(1-2\nu)D_0 \\ \Delta J^{\psi^t} &= 2(1+\nu)\Delta D^{\psi^t} \quad , & \Delta B^{\psi^t} &= 3(1-2\nu)\Delta D^{\psi^t} \end{aligned} \tag{2.5}$$

For the transient part, a Prony series of exponential function is used for the time-dependent function, which for the uniaxial compliance is expressed as

$$\Delta D^{\psi^t} = \sum_{n=1}^{N} D_n (1 - \exp[-\lambda_n \psi^t]) \tag{2.6}$$

where the reduced-time (effective time) is

$$\psi^t \equiv \psi(t) = \int_0^t \frac{d\xi}{a(\bar{\sigma}^\xi, T^\xi)} \tag{2.7}$$

The parameter a ($\bar{\sigma}^t, T^t$) is time shift factors measured with respect to the reference stress and temperature. The integral models in Eqs. (2.3) and (2.4) are solved numerically using a recursive-iterative approach. Detailed recursive-iterative algorithm for the nonlinear VE responses can be found in Haj-Ali and Muliana (2004). The final form of the incremental VE strain by using the recursive-iterative scheme is

$$\Delta\varepsilon_{ij}^{ve,t} = \left[\bar{J}^{t}\sigma_{ij}^{t} + \frac{1}{3}\delta_{ij}\left\{\bar{B}^{t} - \bar{J}^{t}\right\}\sigma_{kk}^{t} \right] - \left[\bar{J}^{t-\Delta t}\sigma_{ij}^{t-\Delta t} + \frac{1}{3}\delta_{ij}\left\{\bar{B}^{t-\Delta t} - \bar{J}^{t-\Delta t}\right\}\sigma_{kk}^{t-\Delta t} \right] - A_{ij}^{t} - \frac{1}{3}B^{t}\delta_{ij} \tag{2.8}$$

$$\bar{J}^{t} = \frac{1}{2}\left[g_0^t J_0 + g_1^t g_2^t \sum_{n=1}^{N} J_n - g_1^t g_2^t \sum_{n=1}^{N} J_n \frac{1-\exp[-\lambda_n \Delta\psi^t]}{\lambda_n \Delta\psi^t} \right] \tag{2.9}$$

$$\bar{B}^{t} = \frac{1}{3}\left[g_0^t B_0 + g_1^t g_2^t \sum_{n=1}^{N} B_n - g_1^t g_2^t \sum_{n=1}^{N} B_n \frac{1-\exp[-\lambda_n \Delta\psi^t]}{\lambda_n \Delta\psi^t} \right] \tag{2.10}$$

$$A_{ij}^{t} = \frac{1}{2}\sum_{n=1}^{N} J_n (g_1^t \exp[-\lambda_n \Delta\psi^{t-\Delta t}] - g_1^{t-\Delta t}) q_{ij,n}^{t-\Delta t} + \frac{1}{2} g_2^{t-\Delta t} \sum_{n=1}^{N} J_n \times \left[g_1^{t-\Delta t}\left(\frac{1-\exp[-\lambda_n \Delta\psi^{t-\Delta t}]}{\lambda_n \Delta\psi^{t-\Delta t}} \right) - g_1^{t}\left(\frac{1-\exp[-\lambda_n \Delta\psi^{t}]}{\lambda_n \Delta\psi^{t}} \right) \right] S_{ij}^{t-\Delta t} \tag{2.11}$$

$$B^{t} = \frac{1}{2}\sum_{n=1}^{N} B_n (g_1^t \exp[-\lambda_n \Delta\psi^{t-\Delta t}] - g_1^{t-\Delta t}) q_{kk,n}^{t-\Delta t} + \frac{1}{2} g_2^{t-\Delta t} \sum_{n=1}^{N} B_n \times \left[g_1^{t-\Delta t}\left(\frac{1-\exp[-\lambda_n \Delta\psi^{t-\Delta t}]}{\lambda_n \Delta\psi^{t-\Delta t}} \right) - g_1^{t}\left(\frac{1-\exp[-\lambda_n \Delta\psi^{t}]}{\lambda_n \Delta\psi^{t}} \right) \right] \sigma_{kk}^{t-\Delta t} \tag{2.12}$$

$\bar{J}^{t}$ and $\bar{B}^{t}$ are the shear and bulk compliances, respectively, that depend on the effective stress and temperature at the current time *t*. History variables are included in A_{ij}^{t} and B^{t}. The shear and volumetric hereditary variables, respectively, $q_{ij,n}^{t-\Delta t}$ and $q_{kk,n}^{t-\Delta t}$ are stored and updated for the next time step. The current time hereditary variables updated from the previous time step are

$$q_{ij,n}^{t} = \exp[-\lambda_n \Delta\psi^t] q_{ij,n}^{t-\Delta t} + (g_2^t S_{ij}^t - g_2^{t-\Delta t} S_{ij}^{t-\Delta t}) \frac{1-\exp[-\lambda_{ij,n}\Delta\psi^t]}{\lambda_{ij,n}\Delta\psi^t} \tag{2.13}$$

$$q_{kk,n}^{t} = \exp[-\lambda_n \Delta\psi^t] q_{kk,n}^{t-\Delta t} + (g_2^t \sigma_{kk}^t - g_2^{t-\Delta t} \sigma_{kk}^{t-\Delta t}) \frac{1-\exp[-\lambda_{ij,n}\Delta\psi^t]}{\lambda_{ij,n}\Delta\psi^t} \tag{2.14}$$

Among the VP models, Perzyna's VP constitutive model, based on an overstress function, is used for the VP component. The VP strain (Perzyna 1966, 1971) for an isotropic material is written as

$$\dot{\varepsilon}_{ij}^{vp,t} = \dot{\lambda}^t \frac{\partial F(\bar{\sigma}^t, k^t)}{\partial \sigma_{ij}^t} \tag{2.15}$$

where $\dot{\varepsilon}_{ij}^{vp,t}$ is the VP strain rate at current time t and $\dot{\lambda}^t$ is the magnitude of the VP strain rate. The stress dependent yield function $F(\bar{\sigma}^t, k^t)$ is expressed in terms of the effective stress $\bar{\sigma}^t = \sqrt{\frac{3}{2} S_{ij}^t S_{ij}^t}$, where S_{ij}^t is the deviatoric stress components; the accumulated effective VP strain $\dot{k}^t = \int_0^t \dot{k}^s ds$, $\dot{k}^t = \sqrt{\frac{2}{3} \dot{\varepsilon}_{ij}^{vp,t} \dot{\varepsilon}_{ij}^{vp,t}}$. The normal direction at the stress point on the yield surface F is derived as vector $\partial F / \partial \sigma$ which is the direction of the VP strain rate. The VP yield function based on an overstress function for isotropic hardening materials at current time *t* is:

$$F(\bar{\sigma}^t, k^t) = \bar{\sigma}^t - \sigma_y^o - hk^t \tag{2.16}$$

The parameter σ_y^o is the initial yield stress measured from a uniaxial loading. The hardening material parameter, *h,* can also depend on the current effective stress $\bar{\sigma}^t$. In this study, the following form for the plastic multiplier is used:

$$\dot{\lambda}^t = \frac{1}{\eta_p} \left\langle \Phi(F) \right\rangle \tag{2.17}$$

where η_p is the viscosity constant during the viscoplastic deformation, < > represents the Macauley bracket, and the function $\Phi(F)$ is given as:

$$\Phi\left(F\right)=\left[\frac{\bar{\sigma}^{t}-\sigma_y^0-hk^{t}}{\sigma_y^0}\right]^n \tag{2.18}$$

The power *n* is the material constant that needs to be calibrated from experiments. The incremental form of the VP strain component is summarized as (see Kim and Muliana, 2009 for a detailed discussion):

$$\begin{aligned}
&\Phi\left(F\right)=\left[\frac{\bar{\sigma}^{t-\Delta t}+\bar{\sigma}^{t}-\sigma_y^0-hk^{t-\Delta t}-h\Delta k^{t}}{\sigma_y^0}\right]^n \\
&\Delta\lambda^{t}=\frac{\Delta t}{\eta_p}\left\langle\left[\frac{\bar{\sigma}^{t-\Delta t}+\bar{\sigma}^{t}-\sigma_y^0-hk^{t-\Delta t}-h\Delta k^{t}}{\sigma_y^0}\right]^n\right\rangle \\
&\Delta\varepsilon_{ij}^{vp,t}=\frac{\Delta t}{\eta_p}\left\langle\left[\frac{\bar{\sigma}^{t-\Delta t}+\bar{\sigma}^{t}-\sigma_y^0-hk^{t-\Delta t}-h\Delta k^{t}}{\sigma_y^0}\right]^n\right\rangle\frac{3}{2\bar{\sigma}^{t}}\left(\delta_{ik}\delta_{ji}-\frac{1}{3}\delta_{ij}\delta_{kl}\right)S_{kl}^{t}
\end{aligned} \tag{2.19}$$

When the stress components are prescribed, the corresponding incremental VE and VP strains can be immediately calculated and the total strain is then obtained from Eq. (2.1). In case the strain components are prescribed like in a displacement based FE it is necessary to calculate the current total stresses and VP strain component, which depends on the current total stresses. For this purpose, a trial incremental VP strain is determined from the stress at the previous time:

$$\Delta\varepsilon_{ij}^{vp,t}=\frac{\Delta t}{\eta_p}\left\langle\left[\frac{\bar{\sigma}^{t-\Delta t}-\sigma_y^0-hk^{t-\Delta t}}{\sigma_y^0}\right]^n\right\rangle\frac{3}{2\bar{\sigma}^{t-\Delta t}}\left(\delta_{ik}\delta_{ji}-\frac{1}{3}\delta_{ij}\delta_{kl}\right)S_{kl}^{t-\Delta t} \tag{2.20}$$

The trial incremental stress is now written as:

$$\Delta\sigma_{ij}^{t,tr} = C_{ijkl}\left(\Delta\varepsilon_{ij}^{t} - \Delta\varepsilon_{ij}^{vp,t(tr)} - \Delta\varepsilon_{ij}^{th,t}\right) \tag{2.21}$$

and the total trial stress is $\sigma_{ij}^{t(tr)} = \sigma_{ij}^{t-\Delta t} + \Delta\sigma_{ij}^{t(tr)}$. Based on this trial stress, the incremental VE and VP strains are calculated using Eqs. (2.8) and (2.19), respectively. The residual incremental strains and plastic multiplier are now determined:

$$\mathbf{R}\varepsilon_{ij}^{t} = \Delta\varepsilon_{ij}^{e,t} - \Delta\varepsilon_{ij}^{vp,t} - \left(\Delta\varepsilon_{ij}^{t} - \Delta\varepsilon_{ij}^{th,t}\right) \tag{2.21}$$

$$\mathbf{R}\lambda^{t} = \Delta\lambda^{t} - \frac{\Delta t}{\eta_p}\left\langle\left[\frac{\bar{\sigma}^{t-\Delta t} + \bar{\sigma}^{t} - \sigma_y^0 - hk^{t-\Delta t} - h\Delta k^{t}}{\sigma_y^0}\right]^n\right\rangle \tag{2.22}$$

The Perzyna model depends on the plastic multiplier $\Delta\lambda^t$, which at current time remains as an unknown variable. To determine the total stress in the VE-VP model, we need to minimize each component of the residual tensors, $\mathbf{R}\varepsilon_{ij}^{t}$ and $\mathbf{R}\lambda^{t}$. This study uses the Newton-Raphson iterative method in order to minimize the residual components. Once the convergence is achieved, the consistent tangent stiffness matrix is calculated.

$$C_{ijkl}^{t} = \left[\frac{\partial\mathbf{R}\varepsilon_{ij}^{t}}{\partial\Delta\sigma_{kl}^{t}}\right]^{-1}; \frac{\partial\mathbf{R}\varepsilon_{ij}^{t}}{\partial\Delta\sigma_{kl}^{t}} = S_{ijkl} + \frac{2}{3}\frac{\Delta\lambda^{t}}{\left(\bar{\sigma}^{t}\right)^2} I'_{ijmn}\left(\bar{\sigma}^{t} I'_{mnkl} - \frac{3}{2\bar{\sigma}^{t}} S_{mn}^{t} S_{pq}^{t} I'_{pqkl}\right) \tag{2.23}$$

where $I'_{ijkl} = \delta_{ik}\delta_{ji} - \frac{1}{3}\delta_{ij}\delta_{kl}$.

2.2 Implementation of VE-VP Models with Experimental Verification

The combined VE-VP constitutive model is used to predict the mechanical response of high-density polyethylene (HDPE) under various loading histories. The experimental data were obtained from Lai and Bakker (1995). The VE-VP constitutive model is implemented in ABAQUS FE using user material subroutine UMAT. Extensive verifications of the VE-VP numerical algorithm, in absence of temperature effects, can be found in Kim and Muliana (2009). The time-dependent material parameters in Eq. (2.6), the Prony series coefficients of HDPE, are given in Table 2.1. The elastic modulus of HDPE is 4535MPa. Poisson's ratio of the tested HDPE is 0.3. The stress-temperature dependent nonlinear VE parameters in Eqs. (2.3) and (2.4) are given in Figure 2.3(a). The stress dependent VP hardening parameters of the Perzyna model are shown in Figure 2.3(b). The Perzyna VP parameters, η_p (fluidity) and n (power) are calibrated to 35 [MPa/s] and 1.36, respectively by fitting the experimental data of HDPE. The initial yield stress σ_y^0 of the Perzyna VP model is calibrated to 1MPa. The above material parameters are obtained at the reference (room) temperature, T_0.

The numerical algorithm of the Schapery VE and Perzyna VP model is verified with experimental data of a two-step loading, which are shown in Figure 2.2. The first step loading is 10MPa for 1800 seconds and the next step loading is followed to 8, 6, 4, 2, and 0MPa, respectively, for 1800 seconds. In the case of low stress level of the second step loading, the numerical results are fitted better than the case of relatively high stress level of second step loading. Based on the results of the numerical model fitting to experimental data, the constitutive model at reference temperature, only stress

dependent, and the numerical methods have been verified for the isotropic polymeric material.

Table 2.1 Prony series coefficients for the HDPE

n	λ_n [s^{-1}]	D_n x 10^4 [MPa^{-1}]
1	1	2.23
2	10^{-1}	2.27
3	10^{-2}	1.95
4	10^{-3}	3.5
5	10^{-4}	5.5
6	10^{-5}	5.5

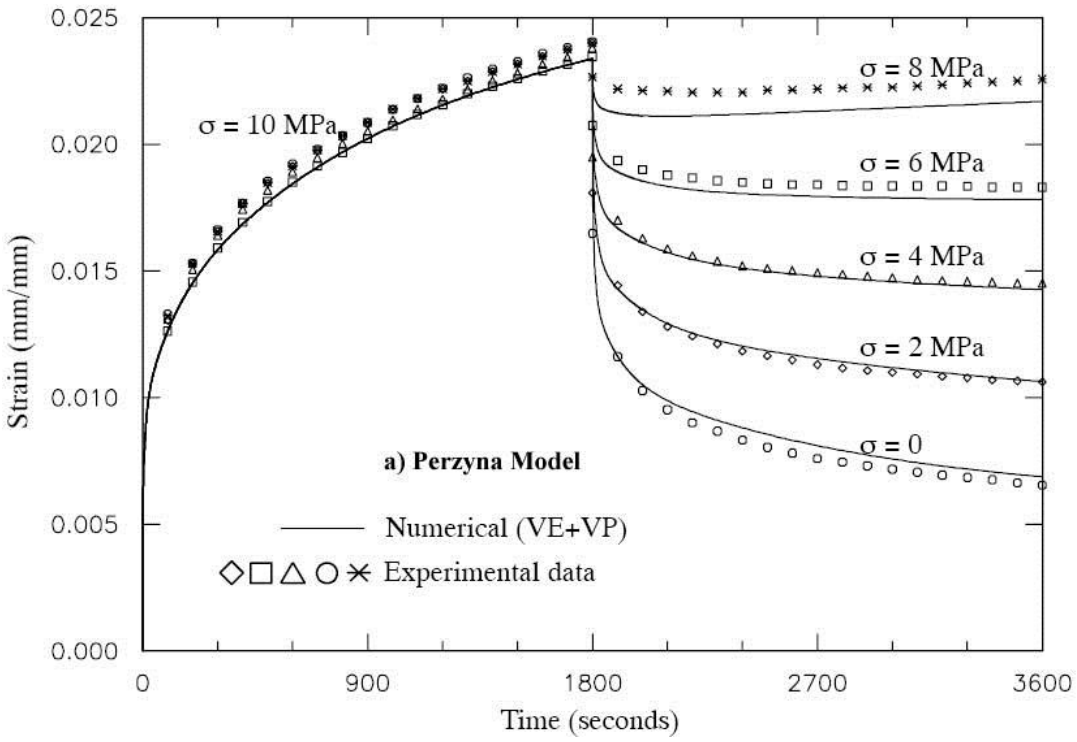

Figure 2.2 Total strains from the two-step loading histories Perzyna Model (Kim, J.S., Muliana, A.H., 2009)

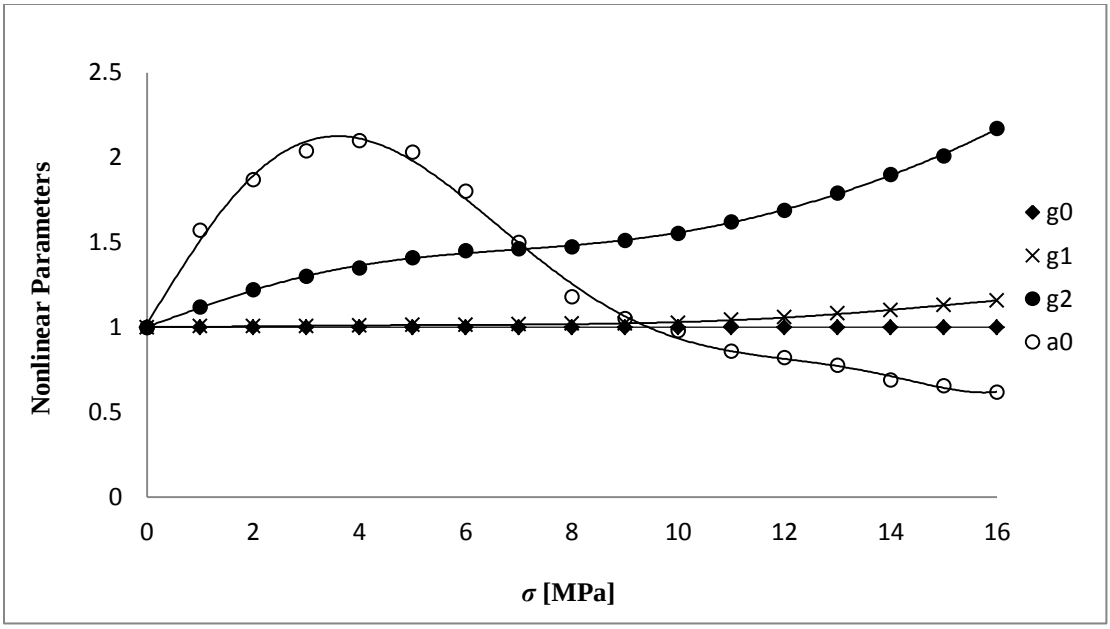

(a)

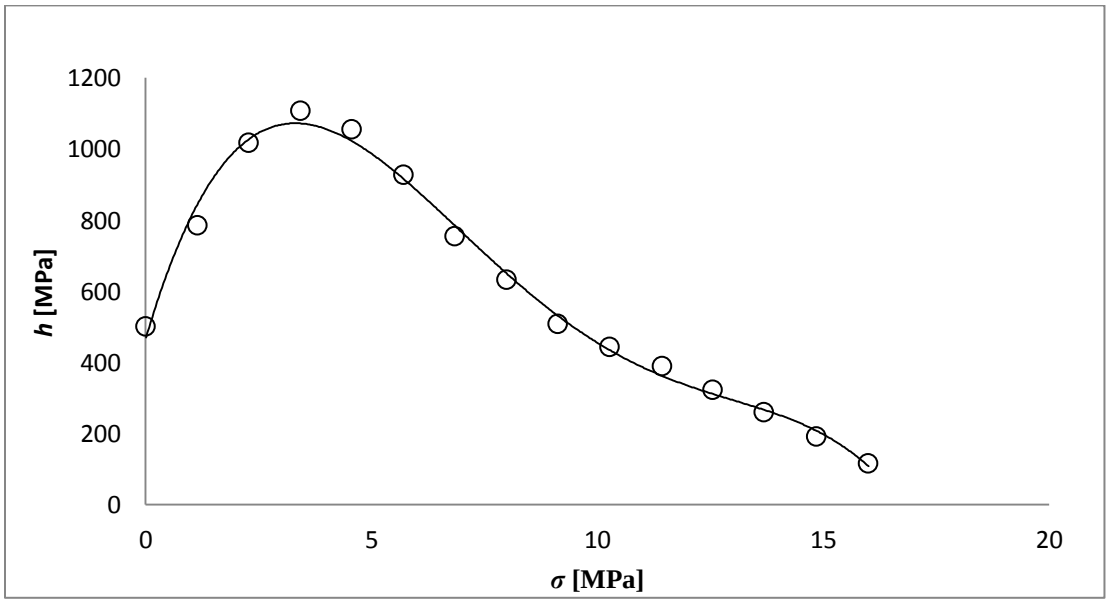

(b)

Figure 2.3 (a) Nonlinear parameters of the Schapery VE model (Lai and Bakker, 1995) and (b) Stress dependent hardening parameters for the Perzyna VP model

2.3 Temperature-dependent VE-VP Model

The combined Schapery and Perzyna model is modified to incorporate the effect of temperature on the overall time-dependent and inelastic material response. The material parameters in the VE-VP model are allowed to vary with temperatures. Since experimental data on the detailed temperature-dependent VE-VP response of polymers are currently lacking, the current section presents parametric studies on understanding the effect of temperature changes on the overall VE-VP response. Martienssen and Warlimont (2005) reported the elastic moduli of HDPE at room temperature up to 333K. The linear elastic modulus is decreasing as the temperature increases, as shown in Figure 2.4(a). At 333K the elastic modulus drops to 29.8% of the elastic modulus at the reference temperature, 296K. The corresponding compliance at this temperature range is also given in Figure 2.4(b). The $g_0(T)$ of the HDPE can now be calibrated from the elastic compliance.

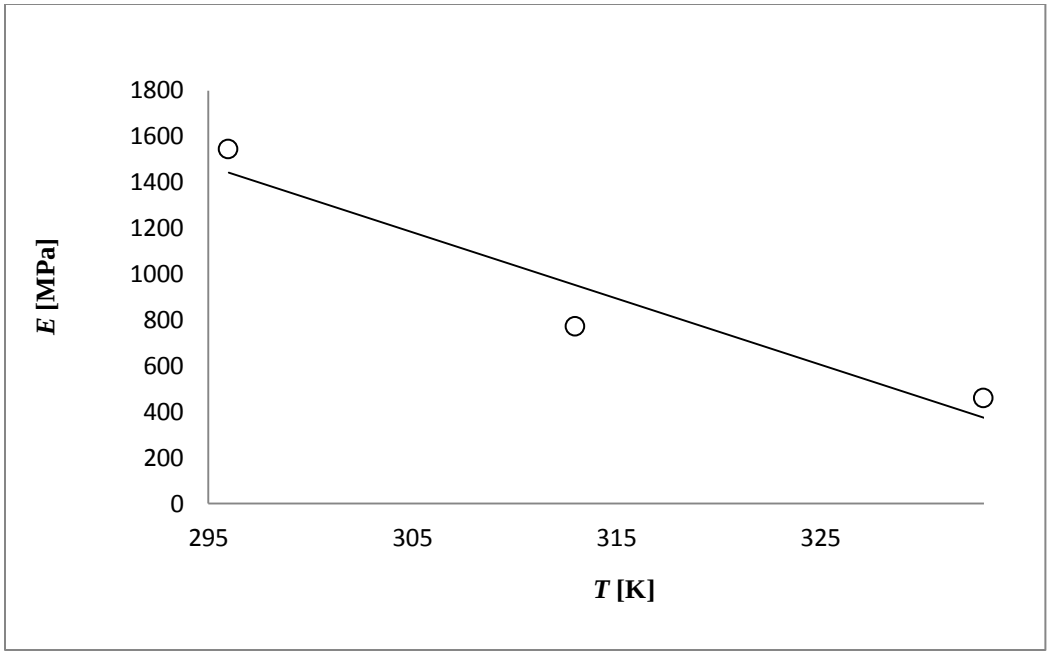

(a) elastic modulus

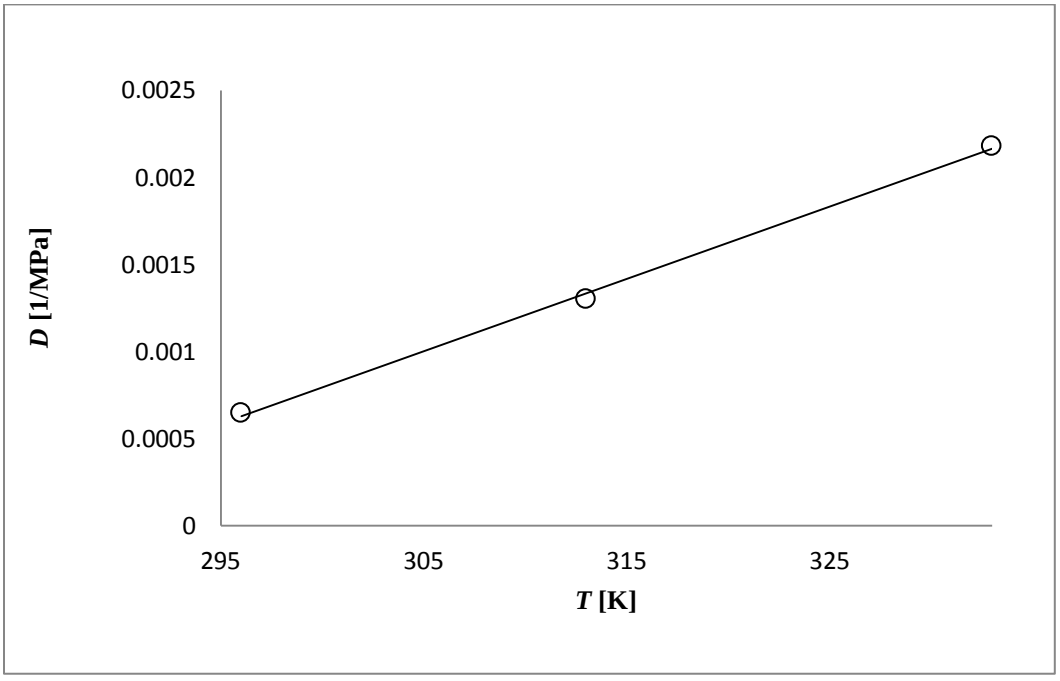

(b) compliances

Figure 2.4 Elastic Modulus and Compliances versus temperature

The temperature dependent material parameters for the VE part for HDPE are expressed by the following functions:

$$g_0(T) = 1 + \beta \frac{T - T_0}{T_0} \tag{2.24}$$

$$g_1(T) = g_2(T) = 1 \tag{2.25}$$

$$a^T(T) = \exp(-\gamma \frac{T - T_0}{T_0}) \tag{2.26}$$

where T_0 is the reference temperature, which is 296K; temperature T are in Kelvin, The material constants β=18.91 and γ=40, respectively. The curves of $g_0(T)$ and $a^T(T)$ are shown in Figures 2.5 and 2.6, respectively.

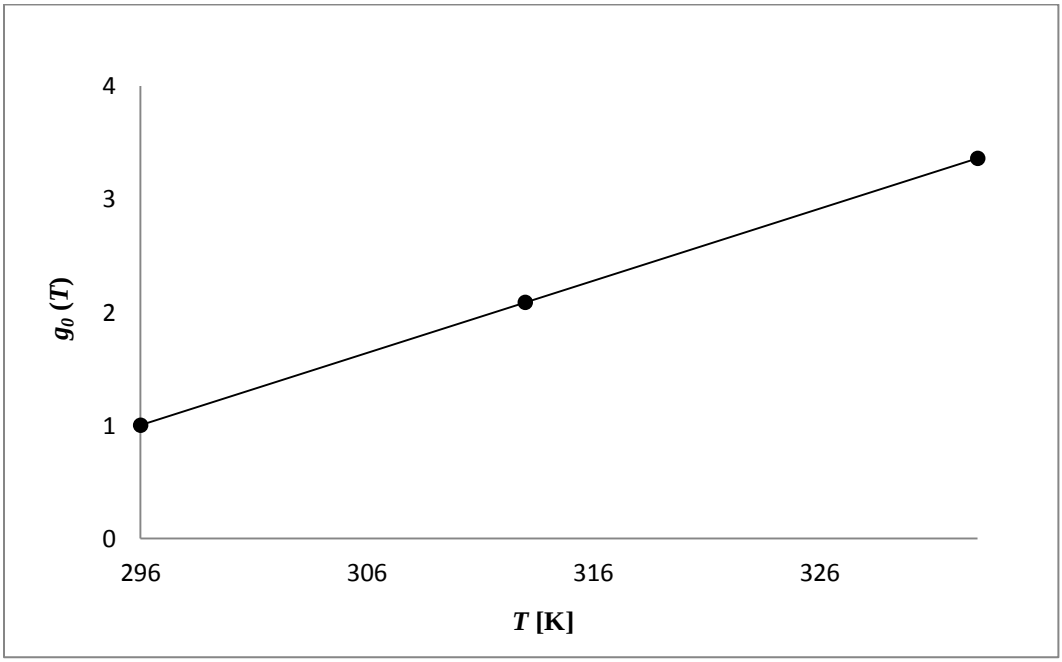

Figure 2.5 Linear function $g_0(T)$ versus temperature

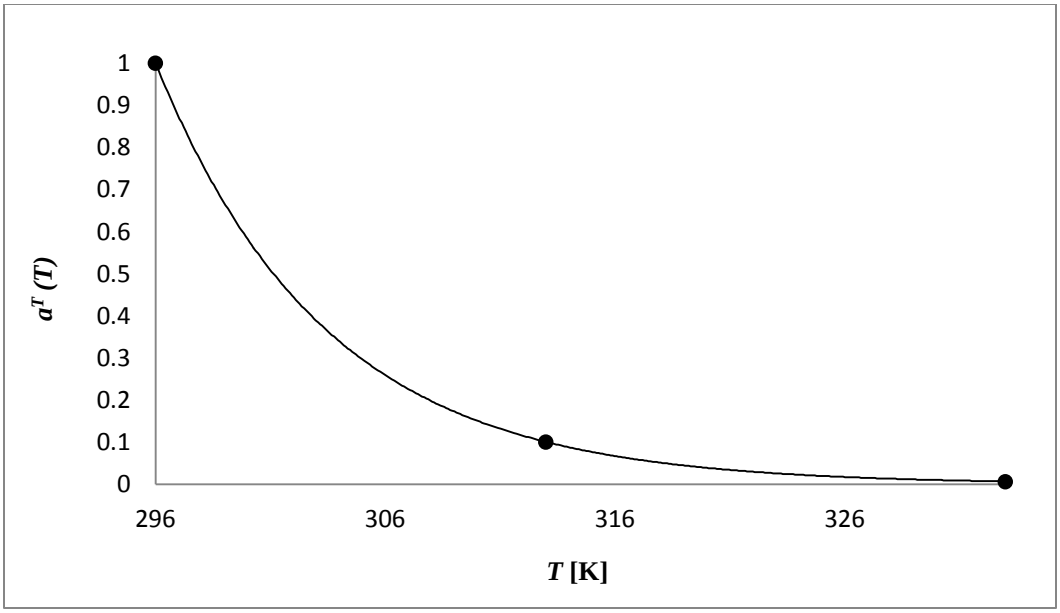

Figure 2.6 Exponential function $a^T(T)$ versus temperature

Based on the degradation of the temperature dependent elastic modulus, it is assumed that the VP parameters such as fluidity, $\eta_p(T)$, and yield stress, $\sigma_y^0(T)$, degrade with the temperature increase following the degradation in the elastic modulus; while the hardening parameters, *h*, and power, *n*, are assumed constant (temperature-independent). Since the elastic modulus decreases to 49.9% at 313K and 29.8% at 333K from the value at the reference temperature, the fluidity, $\eta_p(T)$, and yield stress, $\sigma_y^0(T)$ at the three temperatures are shown in the Table 2.2.

Table 2.2 Viscoplastic parameters with temperature

T [K]	η_p [MPa/s]	σ_y^0 [MPa]
296	35	1
313	17.465	0.499
333	10.43	0.298

Figure 2.7 illustrates the effect of $g_0(T)$ and $a^T(T)$ on the creep recovery strains at temperatures 296K, 313K, and 333K. The creep strain is higher at elevated temperatures, which is expected. The increase in the instantaneous strain is due to the parameter $g_0(T)$ while the increase in the rate of creep and recovery strains is due to the parameter $a^T(T)$. As seen in the recovery period, at 333K the response shows faster strain recovery. The parametric study is now performed on understanding the effect of temperature-dependent fluidity, $\eta_p(T)$, and yield stress, $\sigma_y^0(T)$ on the overall VE-VP response. The corresponding creep-recovery strains due to $\eta_p(T)$ and $\sigma_y^0(T)$ are shown in Figures 2.8 and 2.9. The creep strain increases significantly at elevated temperatures since by decreasing the fluidity and initial yield stress the materials flow easily with the deformations. The recovery period based on the overstress VP model is unaffected by $\eta_p(T)$ and $\sigma_y^0(T)$, which should be expected since the plastic deformation is only formed during loading.

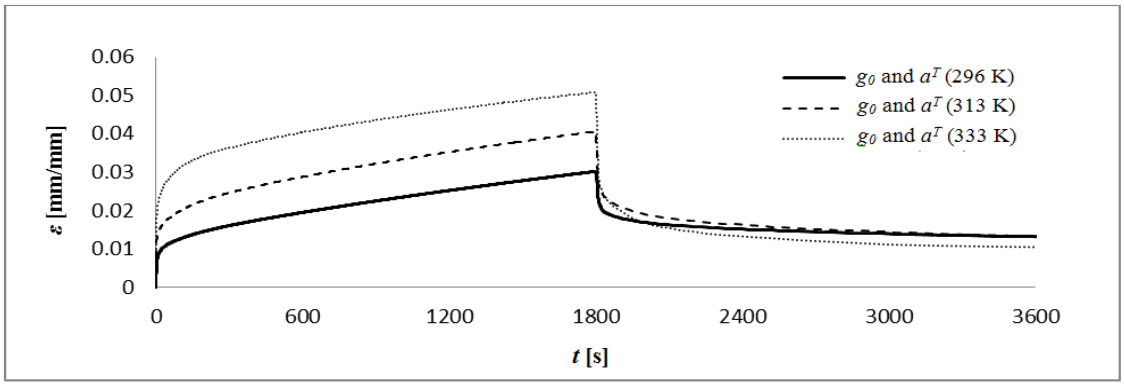

Figure 2.7 Creep Recovery Strain by the effect of $g_0(T)$ and $a^T(T)$

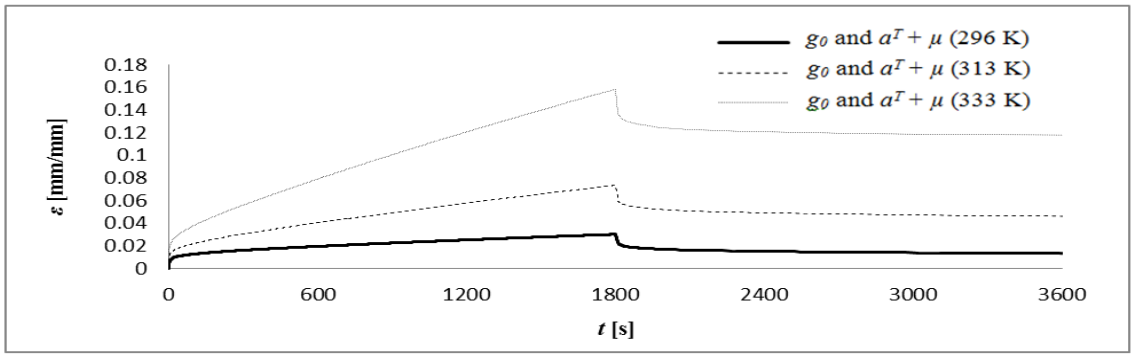

Figure 2.8 Creep Recovery Strain by the effect of $\eta_p(T)$ (Fluidity)

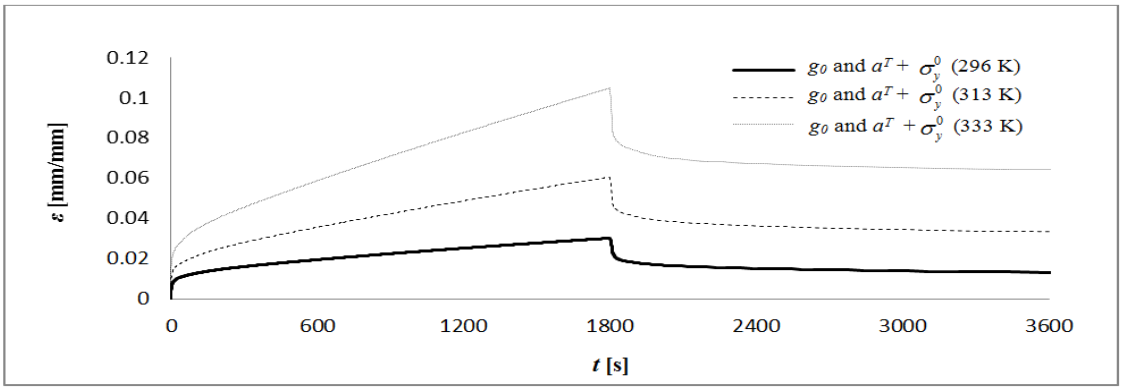

Figure 2.9 Creep Recovery Strain by the effect of $\sigma_y^0(T)$ (Yield Stress)

From the above discussions, the nonlinear VE-VP constitutive model and its numerical implementation are capable of simulating the time-dependent and inelastic response of isotropic materials under various stress inputs and temperatures. This constitutive model is used for the polymeric matrix system in the FRP composites and the overall time-dependent and inelastic response of FRP composites is obtained using micromechanical model (Chapter III).

CHAPTER III

MICROMECHANICAL MODEL FOR FRP COMPOSITES*

This chapter presents a micromechanical model for predicting the overall VE-VP response of FRP composites, having unidirectional elastic fibers dispersed in polymeric matrix. A composite representative volume element (RVE) is defined by a rectangular fiber placed in a rectangular matrix medium. The changes in the micro-structural geometries of the FRP composites during the deformation can be ignored due to the small displacement gradient assumption. A unit-cell consisting of one fiber and three matrix sub-cells is modeled due to the two-plane symmetry of the RVE (Figure 3.1). The first sub-cell represents a fiber constituent, while sub-cells 2, 3, and 4 represent a matrix constituent. The total volume of the unit-cell is equal to one, and each volume of the sub-cells depends on the volume fraction of fibers. The fiber direction is aligned to x_1-direction, and the other directions x_2 and x_3 are transverse fiber directions. The fiber is assumed to be transversely isotropic and linear elastic, while the matrix is assumed to be isotropic with VE-VP response. The outcome of the micromechanical model is a homogenized VE-VP response of FRP composites. The micromechanical model is compatible with a displacement based FE and is implemented in ABAQUS user subroutine material UMAT. The homogenized VE-VP response obtained from the

---

* Reprinted with permission from Jaehyeuk Jeon, Jeongsik Kim, Anastatia Muliana, "Modeling Time-dependent and Inelastic Response of Fiber Reinforced Polymer Composites", Computational Materials Science, Vol.70, pp.37~50, 2013, Copyright 2013 by Elsevier

simplified micromechanical model is validated using experimental data reported by Megnis and Varna (2002) on off-axis glass FRP composites. Furthermore, microstructural models of FRP comprising of longitudinal fibers dispersed randomly in a homogeneous VE-VP polymeric matrix are generated for FRP at different fiber volume contents using FE, termed as FE microstructural models. The VE-VP response from the simplified micromechanical model is compared to the ones from the FE microstructural models.

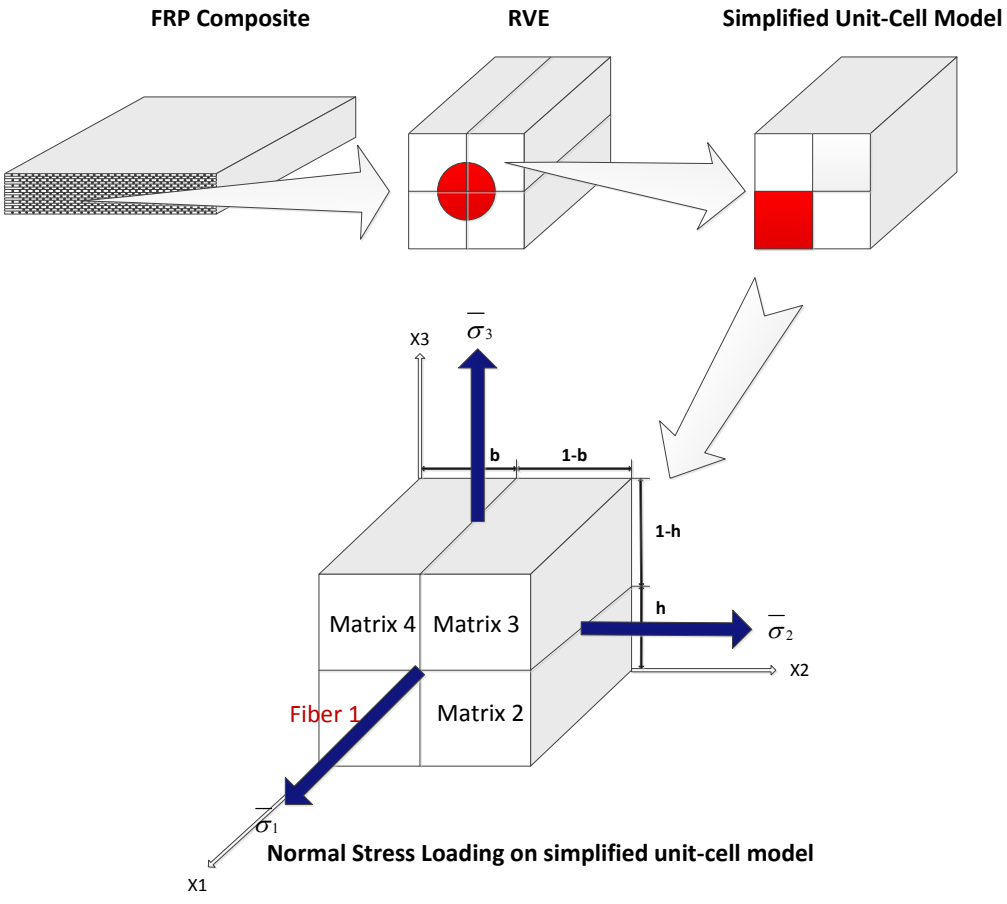

Figure 3.1 Unit-Cell Micromechanical Model for FRP composite

3.1 Micromechanical Formulation for FRP Composite

The formulation of the four-cell micromechanical model of a unidirectional medium is expressed in terms of the average stresses and strains in the subcells. The approximated (average) stresses and strains of the FRP are formed using a volume averaging scheme:

$$\bar{\sigma}_{ij}^{t} = \frac{1}{V}\sum_{\alpha=1}^{N} \int_{V^{(\alpha)}} \sigma_{ij}^{(\alpha),t}(x_k^{(\alpha)})dV^{(\alpha)} \approx \frac{1}{V}\sum_{\alpha=1}^{N} V^{(\alpha)}\sigma_{ij}^{(\alpha),t} \qquad i, j = 1,2,3 \tag{3.1}$$

$$\bar{\varepsilon}_{ij}^{t} = \frac{1}{V}\sum_{\alpha=1}^{N} \int_{V^{(\alpha)}} \varepsilon_{ij}^{(\alpha),t}(x_k^{(\alpha)})dV^{(\alpha)} \approx \frac{1}{V}\sum_{\alpha=1}^{N} V^{(\alpha)}\varepsilon_{ij}^{(\alpha),t} \qquad i, j = 1,2,3 \tag{3.2}$$

where $\sigma_{ij}^{t}(x_k)$ and $\varepsilon_{ij}^{t}(x_k)$ are the components of stress and strain fields in the representative unit-cell model. $\bar{\sigma}_{ij}^{t}$ and $\bar{\varepsilon}_{ij}^{t}$ indicate the effective stresses and strains at current time. The stresses and deformations are assumed spatially uniform in each sub-cell. The stress $\sigma_{ij}^{(\alpha),t}$ and strain $\varepsilon_{ij}^{(\alpha),t}$ are the average stress and strain in each sub-cell at current time. Traction continuity and displacement compatibility at the interfaces between sub-cells are satisfied in an average sense. The superscript (α) denotes the sub-cell number and N is the total number of sub-cells. In this case, N equals to four. The unit-cell total volume V is defined as:

$$V = \sum_{\alpha=1}^{N} V^{(\alpha)} \tag{3.3}$$

The micromechanical relations are expressed in terms of incremental stress and strain components. The incremental forms of the effective stress and strain tensors at the current time are $\bar{\sigma}_{ij}^{t} = \bar{\sigma}_{ij}^{t-\Delta t} + \Delta\bar{\sigma}_{ij}^{t}$ and $\bar{\varepsilon}_{ij}^{t} = \bar{\varepsilon}_{ij}^{t-\Delta t} + \Delta\bar{\varepsilon}_{ij}^{t}$, respectively. The volume averaging

schemes in Eqs. (3.1) and (3.2) are then used to obtain the overall incremental stress and strain components. Hill (1965) defined the concentration matrices for linear elastic composites in order to relate the effective strain and/or stress to the stress and/or strain in the constituents. In this study, the micromechanical model is compatible with displacement based FE structural analyses, in which the effective strains $\bar{\varepsilon}_{ij}^{t} = \bar{\varepsilon}_{ij}^{t-\Delta t} + \Delta\bar{\varepsilon}_{ij}^{t}$ are the independent known variables at time *t*. Thus, the concentration matrices ($\mathbf{B}^{(\alpha),t}$) are formulated to relate the effective incremental strain of the unit cell to the incremental strains in the sub-cells:

$$\Delta\varepsilon_{ij}^{(\alpha),t} = \mathbf{B}_{ijkl}^{(\alpha),t}\Delta\bar{\varepsilon}^{t} \tag{3.4}$$

The above equation describes a linear relationship between the global (average) and local field variables. Substituting Eq. (3.4) to the average strain in Eq. (3.2), in terms of incremental forms, gives:

$$\Delta\bar{\varepsilon}_{ij}^{t} = \frac{1}{V}\sum_{\alpha=1}^{N} V^{(\alpha)}\mathbf{B}_{ijkl}^{(\alpha),t}\Delta\bar{\varepsilon}_{kl}^{t} \tag{3.5}$$

Equation (3.5) is valid for an arbitrary average strain increment $\Delta\bar{\boldsymbol{\varepsilon}}^{t}$ such that the $\mathbf{B}^{(\alpha),t}$ matrices should satisfy the following constraint:

$$\frac{1}{V}\sum_{\alpha=1}^{N} V^{(\alpha)}\mathbf{B}_{ijkl}^{(\alpha),t} = \delta_{ik}\delta_{jl} \tag{3.6}$$

leading to:

$$\frac{1}{V}\sum_{\alpha=1}^{N} V^{(\alpha)}(\mathbf{B}_{ijkl}^{(\alpha),t} - \delta_{ik}\delta_{jl}{}_{kl}^{t}) = 0 \tag{3.7}$$

The linearized constitutive equation is used in each sub-cell (see Chapter II), which is written as:

$$\Delta\sigma_{ij}^{(\alpha),t} = C_{ijkl}^{(\alpha),t}\Delta\varepsilon_{kl}^{(\alpha),t} = C_{ijkl}^{(\alpha),t}\mathbf{B}_{klrs}^{(\alpha),t}\Delta\bar{\varepsilon}_{rs}^{t} \tag{3.8}$$

where $C^{(\alpha),t}$ is the consistent tangent stiffness matrix of the sub-cell (α) at current time *t*. Substituting Eq. (3.8) into Eq. (3.1), the effective incremental stress is expressed as:

$$\Delta\bar{\sigma}_{ij}^{t} = \frac{1}{V}\sum_{\alpha=1}^{N} V^{(\alpha)} C_{ijkl}^{(\alpha),t}\mathbf{B}_{klrs}^{(\alpha),t}\Delta\bar{\varepsilon}_{rs}^{t} \tag{3.9}$$

The unit-cell effective tangent stiffness matrix $\bar{C}^{t}$ at time t is express as follows:

$$\bar{C}_{ijrs}^{t} = \frac{1}{V}\sum_{\alpha=1}^{N} V^{(\alpha)} C_{ijkl}^{(\alpha),t}\mathbf{B}_{klrs}^{(\alpha),t} \tag{3.10}$$

The volume of the unit-cell (Figure 3.1) is taken as one. The volume of the sub-cell 1 represents the fiber volume fraction (FVF) of the composite. The magnitude of side lengths *h* and *f* are always less than one. In this study, the fiber subcell with a square cross-section is considered (*h*=*f*). The volumes of the four sub-cells are then shown as:

$$V^{(1)} = fh,\ V^{(2)} = h(1-f),\ V^{(3)} = f(1-h),\ V^{(4)} = (1-h)\ (1-f) \tag{3.11}$$

The 3D nonlinear constitutive models of the fiber and matrix are separately used in the fiber and matrix sub-cells. The response of the fiber in the first sub-cell is linear elastic and transversely isotropic, on the other hand, the response of the isotropic polymeric matrix is VE-VP. The traction continuity and displacement compatibility are satisfied within the micromechanical model that is based on perfect bond on the interfaces between the sub-cells. The following equations (micromechanical relations)

satisfy the displacement compatibility of homogenized unit-cell for a unidirectional composite medium:

$$\Delta\bar{\varepsilon}_{11}^{t} = \Delta\varepsilon_{11}^{(1),t} = \Delta\varepsilon_{11}^{(2),t} = \Delta\varepsilon_{11}^{(3),t} = \Delta\varepsilon_{11}^{(4),t} \tag{3.13}$$

$$\Delta\bar{\varepsilon}_{22}^{t} = \frac{V^{(1)}}{V^{(1)}+V^{(2)}}\Delta\varepsilon_{22}^{(1),t} + \frac{V^{(2)}}{V^{(1)}+V^{(2)}}\Delta\varepsilon_{22}^{(2),t} \tag{3.14}$$

$$\Delta\bar{\varepsilon}_{22}^{t} = \frac{V^{(3)}}{V^{(3)}+V^{(4)}}\Delta\varepsilon_{22}^{(3),t} + \frac{V^{(4)}}{V^{(3)}+V^{(4)}}\Delta\varepsilon_{22}^{(4),t} \tag{3.15}$$

$$\Delta\bar{\varepsilon}_{33}^{t} = \frac{V^{(1)}}{V^{(1)}+V^{(3)}}\Delta\varepsilon_{33}^{(1),t} + \frac{V^{(3)}}{V^{(1)}+V^{(3)}}\Delta\varepsilon_{33}^{(3),t} \tag{3.16}$$

$$\Delta\bar{\varepsilon}_{33}^{t} = \frac{V^{(2)}}{V^{(2)}+V^{(4)}}\Delta\varepsilon_{33}^{(2),t} + \frac{V^{(4)}}{V^{(2)}+V^{(4)}}\Delta\varepsilon_{33}^{(4),t} \tag{3.17}$$

$$\Delta\bar{\gamma}_{12}^{t} = \frac{V^{(1)}}{V^{(1)}+V^{(2)}}\Delta\gamma_{12}^{(1),t} + \frac{V^{(2)}}{V^{(1)}+V^{(2)}}\Delta\gamma_{12}^{(2),t} \tag{3.18}$$

$$\Delta\bar{\gamma}_{12}^{t} = \frac{V^{(3)}}{V^{(3)}+V^{(4)}}\Delta\gamma_{12}^{(3),t} + \frac{V^{(4)}}{V^{(3)}+V^{(4)}}\Delta\gamma_{12}^{(2),t} \tag{3.19}$$

$$\Delta\bar{\gamma}_{13}^{t} = \frac{V^{(1)}}{V^{(1)}+V^{(3)}}\Delta\gamma_{13}^{(1),t} + \frac{V^{(3)}}{V^{(1)}+V^{(3)}}\Delta\gamma_{13}^{(3),t} \tag{3.20}$$

$$\Delta\bar{\gamma}_{13}^{t} = \frac{V^{(2)}}{V^{(2)}+V^{(4)}}\Delta\gamma_{13}^{(2),t} + \frac{V^{(4)}}{V^{(2)}+V^{(4)}}\Delta\gamma_{13}^{(4),t} \tag{3.21}$$

$$\Delta\bar{\gamma}_{23}^{t} = V^{(1)}\Delta\gamma_{23}^{(1),t} + V^{(2)}\Delta\gamma_{23}^{(2),t} + V^{(3)}\Delta\gamma_{23}^{(3),t} + V^{(4)}\Delta\gamma_{23}^{(4),t} \tag{3.22}$$

The traction continuity leads to:

$$\Delta\bar{\sigma}_{11}^{t} = V^{(1)}\Delta\sigma_{11}^{(1),t} + V^{(2)}\Delta\sigma_{11}^{(2),t} + V^{(3)}\Delta\sigma_{11}^{(3),t} + V^{(4)}\Delta\sigma_{11}^{(4),t} \tag{3.23}$$

$$\Delta\sigma_{22}^{(1),t} = \Delta\sigma_{22}^{(2),t} \tag{3.24}$$

$$\Delta\sigma_{22}^{(3),t} = \Delta\sigma_{22}^{(4),t} \tag{3.25}$$

$$\Delta\sigma_{33}^{(1),t} = \Delta\sigma_{33}^{(3),t} \tag{3.26}$$

$$\Delta\sigma_{33}^{(2),t} = \Delta\sigma_{33}^{(4),t} \tag{3.27}$$

$$\Delta\tau_{12}^{(1),t} = \Delta\tau_{12}^{(2),t} \tag{3.28}$$

$$\Delta\tau_{12}^{(3),t} = \Delta\tau_{12}^{(4),t} \tag{3.29}$$

$$\Delta\tau_{13}^{(1),t} = \Delta\tau_{13}^{(3),t} \tag{3.30}$$

$$\Delta\tau_{13}^{(2),t} = \Delta\tau_{13}^{(4),t} \tag{3.31}$$

$$\Delta\bar{\tau}_{23}^{t} = \Delta\tau_{23}^{(1),t} = \Delta\tau_{23}^{(2),t} = \Delta\tau_{23}^{(3),t} = \Delta\tau_{23}^{(4),t} \tag{3.32}$$

The concentration matrices are determined by using the micromechanical relations (Eqs. (3.13)-(3.32)) and the constitutive relation in Chapter II. Equations (3.13-3.32) consist of two groups of strain vectors satisfying the displacement compatibility equations and the equilibrium relations, which are written in Eqs. (3.33) and (3.34). The residual vectors $\mathbf{R}_{\varepsilon}^{t}$ and $\mathbf{R}_{\sigma}^{t}$ in Eqs. (3.33) and (3.34) arise from imposing the displacement compatibility and equilibrium relations, respectively, with linearized stress-strain relations. In this study, the strain components in each subcell are taken as independent field variables. Thus, there are 24 strain components that require forming 24 equations. In the linear elastic case, these residual vectors are zero, while in the nonlinear and inelastic case the linearized micromechanical relations result in non-zero residuals. The linearized micromechanical relations cannot be satisfied with nonlinear response of the matrix subcells. In order to minimize the residual, an iterative correction scheme is

formulated at the global and local levels. The numerical scheme is briefly shown in Figure 3.2.

$$\underset{(13x1)}{\left\{ \mathbf{R}_{\varepsilon}^{t} \right\}} = \underset{(13x24)}{\left[\mathbf{A}_{1}^{t} \right]} \underset{(24x1)}{\left\{ \begin{matrix} \Delta\varepsilon^{(1),t} \\ \Delta\varepsilon^{(2),t} \\ \Delta\varepsilon^{(3),t} \\ \Delta\varepsilon^{(4),t} \end{matrix} \right\}} - \underset{(13x6)}{\left[\mathbf{D}_{1} \right]} \underset{(6x1)}{\{\Delta\bar{\varepsilon}^{t}\}} \tag{3.33}$$

$$\underset{(11x1)}{\left\{ \mathbf{R}_{\sigma}^{t} \right\}} = \underset{(11x24)}{\left[\mathbf{A}_{2}^{t} \right]} \underset{(24x1)}{\left\{ \begin{matrix} \Delta\varepsilon^{(1),t} \\ \Delta\varepsilon^{(2),t} \\ \Delta\varepsilon^{(3),t} \\ \Delta\varepsilon^{(4),t} \end{matrix} \right\}} - \underset{(11x6)}{\left[\mathbf{O} \right]} \underset{(6x1)}{\{\Delta\bar{\varepsilon}^{t}\}} \tag{3.34}$$

$$\underset{(24x6)}{\left[\begin{matrix} \mathbf{B}^{t,(1)} \\ \mathbf{B}^{t,(2)} \\ \mathbf{B}^{t,(3)} \\ \mathbf{B}^{t,(4)} \end{matrix} \right]} = \underset{(24x24)}{\left[\begin{matrix} \mathbf{A}^{t}{}_{1} \\ \mathbf{A}^{t}{}_{2} \end{matrix} \right]^{-1}} \underset{(24x6)}{\left[\begin{matrix} \mathbf{D}_{1} \\ \mathbf{O} \end{matrix} \right]} \tag{3.35}$$

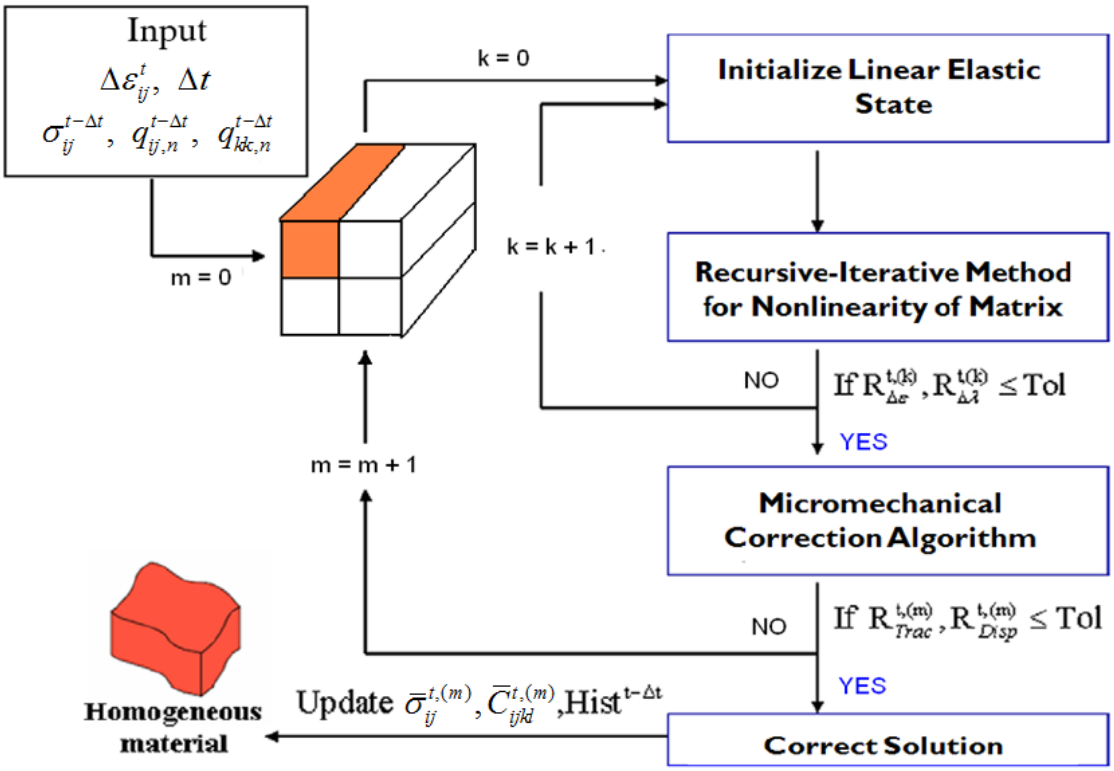

Figure 3.2 A numerical algorithm for the simplified VE-VP micromechanical model

3.2 Detailed FE Micromechanical Models for FRP Composites

In FRP composites, fibers are not necessarily of the same size nor are they positioned regularly in the matrix medium. In order to examine the effects of fiber arrangements in the polymeric matrix, microstructural geometries of FRP composites are generated using FE. The detailed FE microstructural models describe the configuration of fibers and matrix. Figure 3.2 shows the micromechanical models with microstructural details for composites with 10%, 20%, 50% fiber volume fractions. For each fiber volume fraction, two kinds of microstructural configurations, i.e., uniform and random fiber distributions, are considered. The effects of different fiber arrangements on the

overall time-dependent response and stress/strain field of the composites are studied. In addition, FE micromechanical models are considered for composites with 40%, 54%, 67%, 75% fiber volume contents with uniform fiber arrangements. The fibers in the micromechanical models with detailed fiber arrangements have the same diameter. The detailed micromechanical models are generated using 3D continuum elements. These micromechanical models have a total of 73728-247290 elements. A convergence study is conducted in order to determine sufficient numbers of elements in each micromechanical model with detailed fiber arrangements. The numbers of fibers in the cubic RVE depend on the volume fraction of fiber. Like in the unit-cell model, a linear elastic material response is used for the fibers and the VE-VP material response (Chapter II) is considered for the polymeric matrix. It is assumed that the interfaces between fibers and matrix are bonded perfectly. Incorporating detailed fiber arrangements in a homogeneous matrix allows capturing the variations in the field variables and localized stresses within the composite microstructures. The ultimate goal is to examine the effect of variations in the field variables and localized stresses on the overall (average) time-dependent and inelastic response of FRP composites.

3.3 Comparison of the Homogenized Unit-cell Model and FE Micromechanical Models

The overall VE-VP response obtained from the homogenized micromechanical model, having four sub-cells, is compared with the one of micromechanical models having detailed fiber arrangements generated using FE, as seen in Figure 3.3. Carbon fiber is used for the fiber constituent and the matrix properties are based on HDPE

reported by Kim and Muliana (2009). The linear elastic properties of the carbon fibers (T300) are given in Table 3.1, which is reported by Miyagawa et al. (2005). The VE-VP properties of the HDPE matrix are given in Chapter II. Figure 3.3 shows the detailed FE micromechanical models with 10%, 20%, 50% fiber volume fractions. For each fiber volume fraction, two kinds of microstructural configurations, i.e., uniform and random fiber distributions, are considered. The detailed micromechanical models are generated using 3D continuum elements.

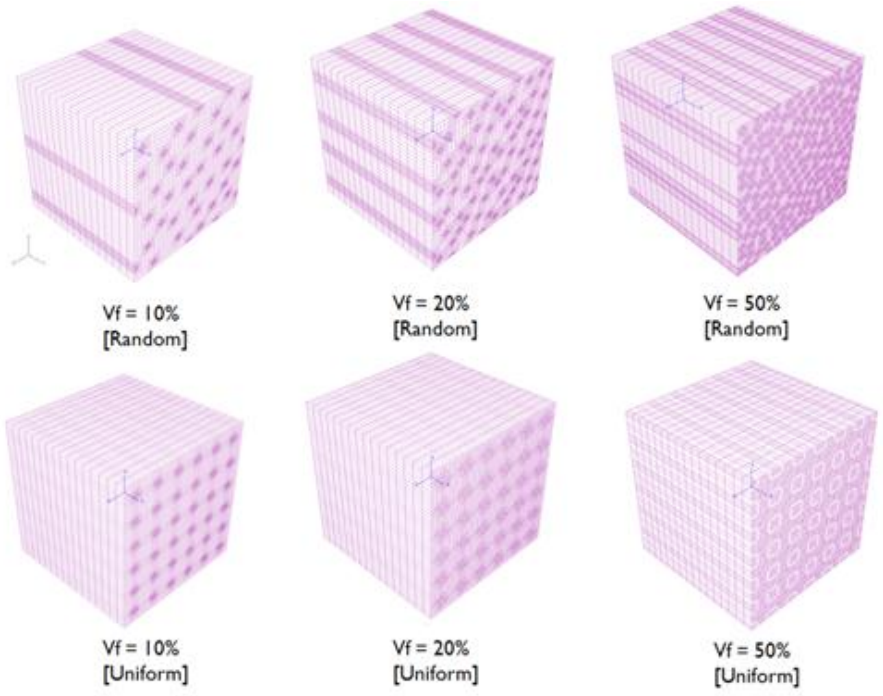

Figure 3.3 FE meshes of micromechanical models with detailed fiber arrangements

Table 3.1 Mechanical Properties of Carbon Fibers

Carbon Fiber	E_{11} [GPa]	$E_{22}=E_{33}$ [GPa]	$G_{12}=G_{13}$ [GPa]	G_{23} [GPa]	$\nu_{12}=\nu_{13}$	ν_{23}
(T300)	230	10.4	27.3	3.08	0.256	0.3

First, the effective linear elastic moduli of the FRP composites with 10%, 20%, 50% fiber volume fractions generated from the UC and detailed FE micromechanical models are compared, which are summarized in Table 3.2 and illustrated in Figure 3.4. The reported moduli are along the fiber longitudinal direction and transverse to the fiber direction. It is seen that the effective elastic moduli of the FRP composites obtained from the unit-cell and FE heterogeneous micromechanical models with uniform and random fiber array are comparable. The differences (in percent) of the effective elastic moduli of the two models, shown in Table 3.2, slightly increase with increasing the fiber volume contents from 10% to 50%. The reason of the increasing differences is probably due to interaction between fibers that could lead to stress-concentration effects. In the simplified unit-cell model, fiber is assumed fully surrounded by the matrix and interactions between fibers are not considered. In the composites with detailed microstructural arrangements, the spacing between fibers decreases as the fiber volume contents increase, which can result in localized stresses as reported by Muliana and Sawant (2009). The uniform fiber arrangements for the composites with 10 and 20% fiber volume fractions show less difference than the random fiber arrangements. The spacing between fibers in the composite models with random fiber arrangements is

irregular that can result in higher possibility of the stress concentration due to narrow space between the fibers, which is more realistic microstructural representations. Figure 3.5 shows the effective stress (von Misses stress) fields of a composite with 10% fiber volume content loaded along and transverse to the fiber axis. In both loadings, a uniaxial stress 10MPa is applied. It is seen that when the composite is loaded in the transverse fiber direction, more variations of the stress fields in the matrix are observed. However, for the composites with 10% fiber volume content, the variations are relatively small. Figure 3.6 illustrates the effective stress contours for composites with 20 and 50% fiber volume contents loaded in the transverse fiber direction. As fiber volume content increases, the spacing between fibers decreases, resulting in higher stresses localized in these regions.

The axial and transverse elastic moduli of the detailed micromechanical models for 40%, 54%, 67%, 75% fiber volume contents of FRP composites with uniform fiber configuration are shown in Table 3.3. The moduli of the FRP composites obtained from the detailed micromechanical models are comparable to the ones obtained from the unit cell model with relatively small differences. Figure 3.7 shows the overall elastic moduli for all studied volume contents generated from the unit-cell model and detailed micromechanical model with uniform fiber arrangements. It is seen that the effective elastic moduli from the two micromechanical models are in a good agreement, indicating a minimum effect of the localized stresses on the overall elastic moduli of FRP composites.

Table 3.2 Comparisons of the Effective Elastic Moduli

	V_f [%] (Fiber Volume Fraction)	10		20		50	
	Fiber Array	Effective Elastic Modulus [GPa]	Diff. %	Effective Elastic Modulus [GPa]	Diff. %	Effective Elastic Modulus [GPa]	Diff. %
E_{11}	Unit Cell	27.08	0	49.63	0	117.27	0
	Detailed FE [Uniform]	26.49	2.19	48.46	2.35	112.23	4.49
	Detailed FE [Random]	26.41	2.47	48.32	2.63	114.02	2.77
E_{22}	Unit Cell	5.22	0	5.64	0	7.13	0
	Detailed FE [Uniform]	5.21	0.15	5.62	0.43	6.99	2.00
	Detailed FE [Random]	5.20	0.33	5.59	0.96	6.98	2.10

Table 3.3 Comparisons of the Effective Elastic Moduli for Unit-cell and Detailed Micromechanical Models with Uniform Fiber Arrangements

Loading Direction	Axial Loading [E-Moduli]			Transverse Loading [E-Moduli]		
Model	Unit-Cell [GPa]	Detailed FE [GPa]	% Difference	Unit-Cell [GPa]	Detailed FE [GPa]	% Difference
V_f =40%	94.72	92.42	2.49%	6.60	6.49	1.58%
V_f=54%	126.63	123.55	2.49%	7.37	7.18	2.57%
V_f =67%	154.85	151.02	2.53%	8.11	7.92	2.44%
V_f =75%	173.63	169.33	2.54%	8.64	8.44	2.42%

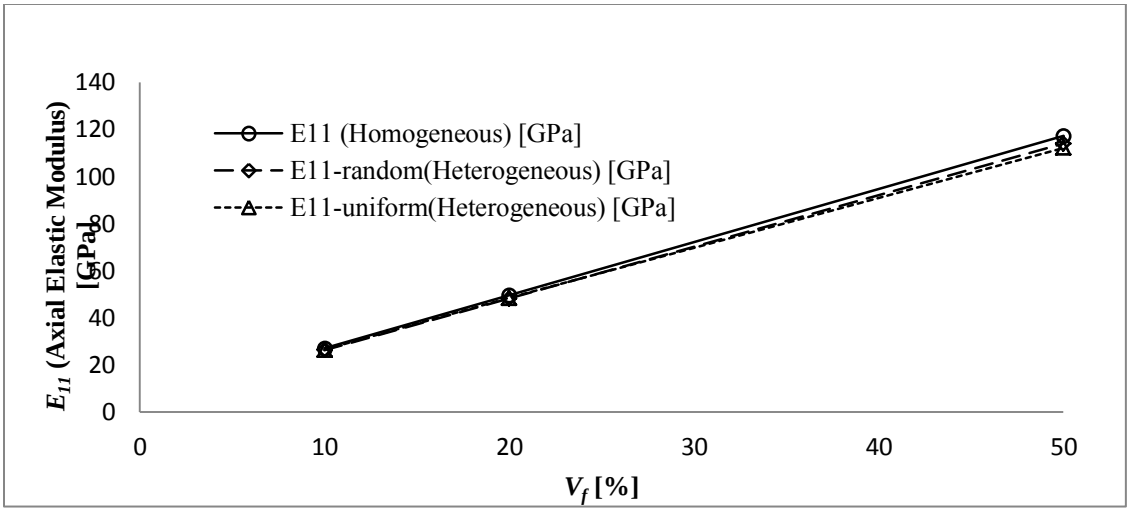

(a)

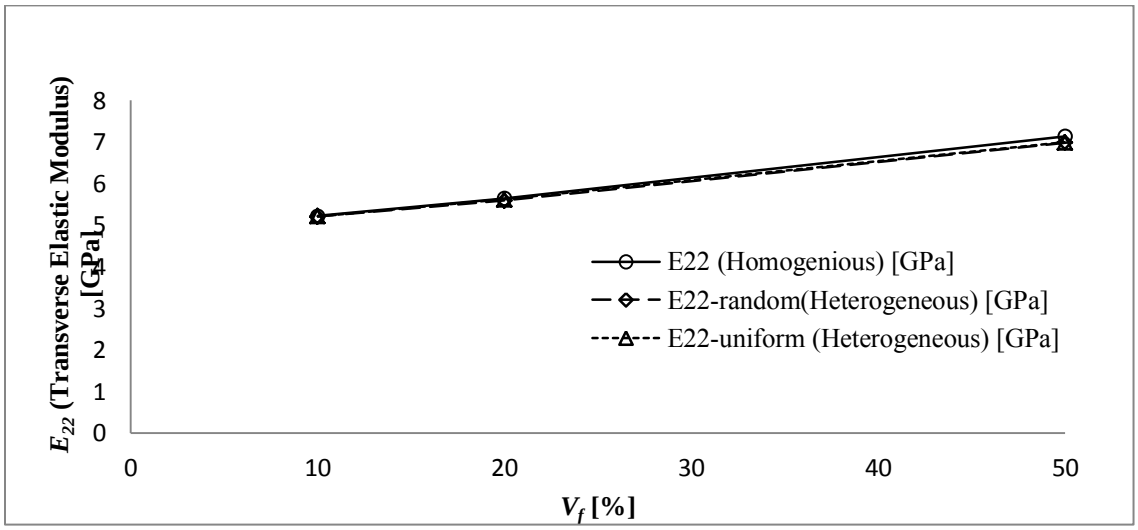

(b)

Figure 3.4 (a) Effective elastic moduli along and (b) transverse fiber directions

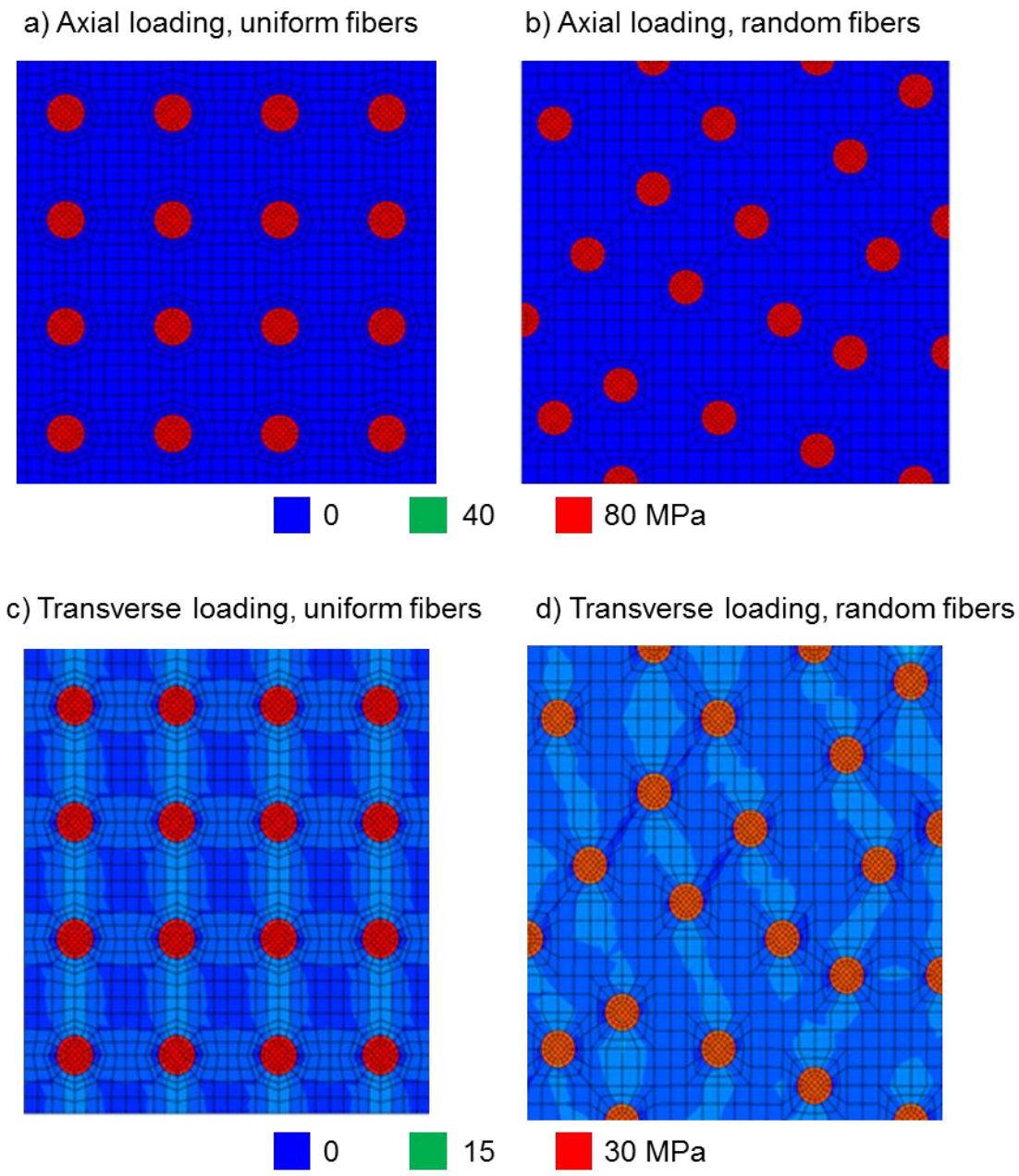

Figure 3.5 Stress contours of composites with 10% fiber volume content under uniaxial stress 10MPa

a) V_f= 20%, uniform fibers

b) V_f= 20%, random fibers

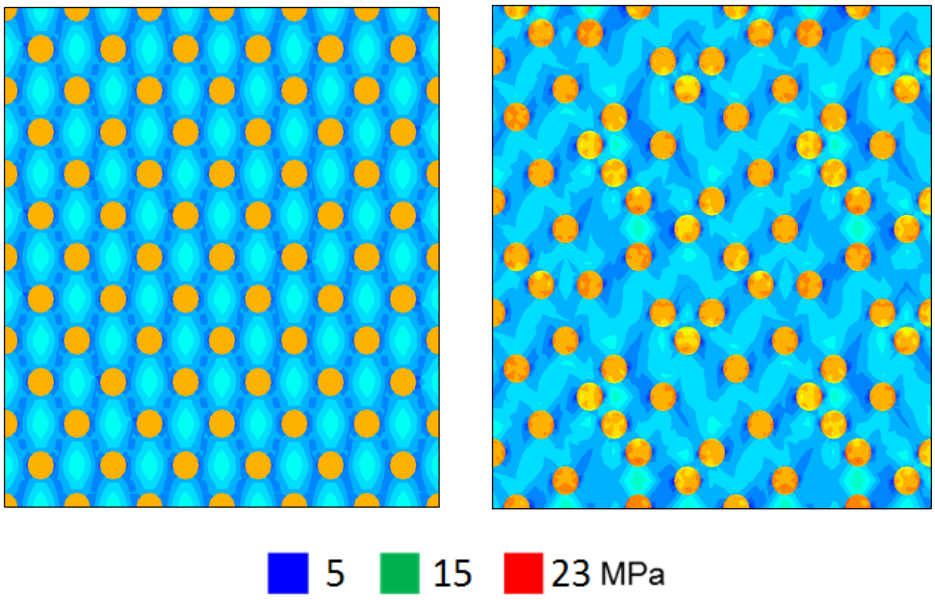

c) V_f= 50%, uniform fibers

d) V_f= 50%, random fibers

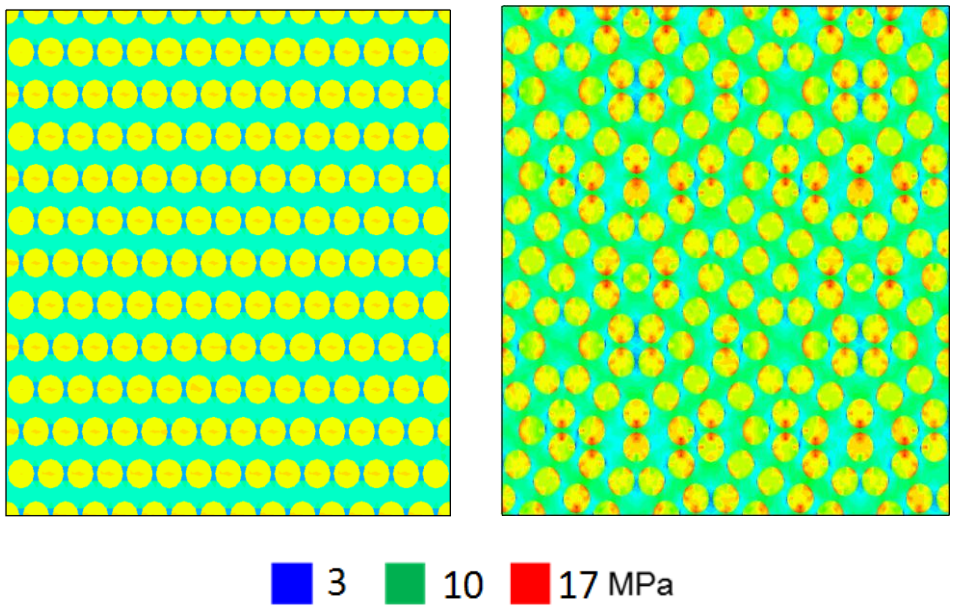

Figure 3.6 Stress contours of composites with 20 and 50% fiber volume contents loaded in the transverse fiber direction

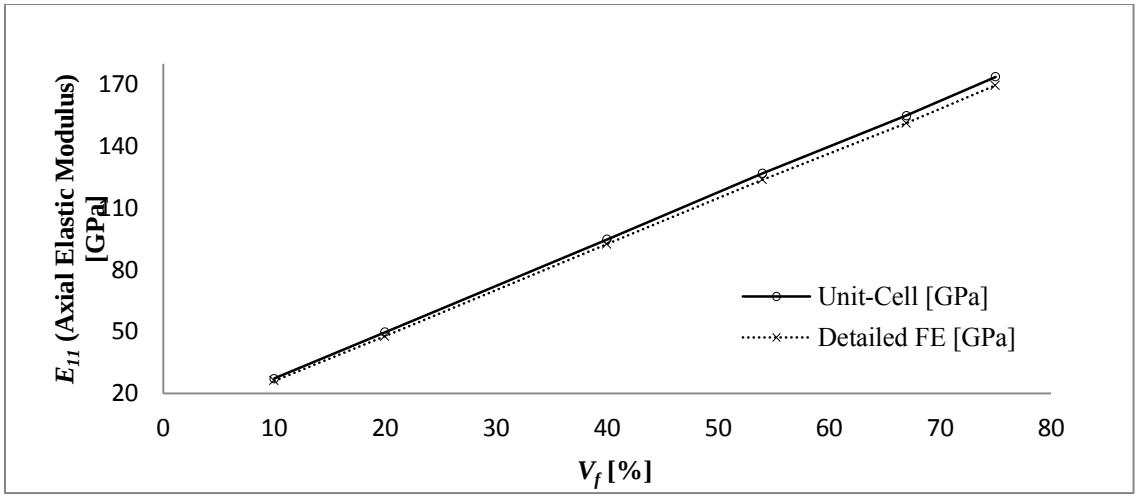

(a)

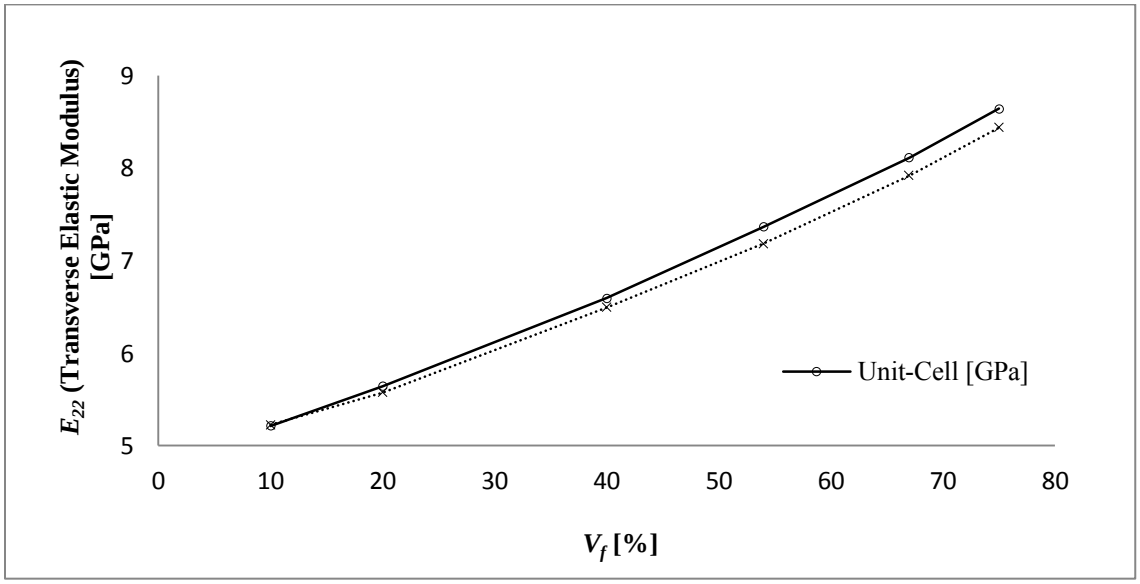

(b)

Figure 3.7 Effective elastic moduli of FRP composites with different fiber volume contents: (a) along the fiber direction and (b) transverse to the fiber directions

Next, the creep-recovery response under a constant uniaxial stress of 10MPa applied along the longitudinal fiber direction is considered. The creep is done for 1800

seconds followed by 1800-second recovery. The creep-recovery loading with stress of 3MPa is considered in the transverse fiber directions in order to avoid the high localized stresses in the matrix between the fibers. The VE-VP responses obtained from the two micromechanical models are compared. The UC model is integrated to one continuum 3D element and the homogenized (overall) response is sampled at each material (Gaussian) integration point. In the case of micromechanical models with detailed fiber arrangements, the VE-VP constitutive models discussed in Chapter II are implemented at the material points within the matrix finite elements. In order to examine the efficiency of the two-micromechanical modeling approaches, computing (central processing unit, CPU) times during the creep-recovery analyses for the composites with 10, 20, and 50% fiber volume contents are monitored, as reported in Table 3.4. The CPU times are reported for the creep-recovery analyzes with a uniaxial stress applied in the fiber and transverse directions. As expected the computing time required in the UC model is much less than the one of the FE micromechanical models with microstructural details. It is noted that the micromechanical models with the combined VE-VP response results in much higher computing time than when only the VE response is considered, which is due to more iterations needed in solving the VE+VP response.

The corresponding strains during the creep-recovery loadings for the composites with 10-75% fiber volume contents, when the VE is considered for the polymeric matrix, are shown in Figures 3.8-3.10. The strains determined from the UC and micromechanical models with detailed fiber arrangements are relatively close with a percentage difference at time 1800 seconds is given in Tables 3.5 and 3.6. The detailed

micromechanical models with uniform fiber arrangements are considered. When the composite is loaded along the axial fiber direction, the fiber carries the majority of the loads and the time-dependent behavior of the matrix is insignificant. On the other hand, for loading in the transverse fiber direction the matrix carries relatively high mechanical loading, resulting in pronounced time-dependent response. The effective stress contours for composites with 54, 67, and 75% fiber volume contents loaded in the transverse direction under an overall stress level 3MPa are illustrated in Figure 3.11. The contours are obtained at 1800 seconds. It is seen that localized stresses are shown in the composites. These localized stresses are higher than the nominal stress prescribed on the boundary of the micromechanical models. The stress-dependent viscoelastic constitutive model for the matrix results in higher strain response which significantly increases the localized stresses in the composites. The detailed micromechanical models are capable in capturing the detailed variations of the stress and strain fields, while the UC model is limited in incorporating the different stress and strain fields in the matrix. It is noted that in the UC model, the variations of the stress and strain fields in the matrix are captured by the three sub-cells and each sub-cell has uniform stress and strain fields. Table 3.6 presents the percent differences in the overall strains determined from the UC and detailed micromechanical models for composites with 40, 54, 67, and 75% fiber volume contents. It is seen that the highest difference is for the composites with 67% fiber volume contents loaded in the transverse fiber direction which is probably due to the significant effects of the localized stresses on the matrix dominated response. However, for the composite with 75% fiber volume content under the transverse loading, percent

differences between the responses obtained from the UC and detailed micromechanical models decrease. This is probably due to the relatively dense fibers in that the linear elastic fibers would carry significant amount of the mechanical load.

Table 3.4 CPU time for VE and VE+VP in homogeneous and heterogeneous models

	FE Models	V_f [%]	Total	CPU Time [s]	
			Elements	Fiber Dir.	Transverse Dir.
VE	Unit-cell model	10	1	2.1	75.4
		20	1	2	75.6
		50	1	1.6	168.7
	Detailed FE model	10	73728	41170 [11 hr]	534776 [149 hr]
		20	73728	10952 [3 hr]	164220 [46 hr]
		50	137490	25724 [7 hr]	20632 [6 hr]
VE+VP	Unit-cell model	10	1	1.9	78.6
		20	1	1.9	79.7
		50	1	1.8	3836.6
	Detailed FE model	10	73728	92753 [26 hr]	11059224 [128 days]
		20	73728	137217 [38 hr]	2095620 [24 days]
		50	137490	24582 [7 hr]	3539790 [41 days]

Table 3.5 Percent difference of the strains from the unit-cell and FE micromechanical models

Fiber Array		Time [s]	Loading Direction	Strain	Difference %		
					V_f= 10%	V_f= 20%	V_f = 50%
Unit-cell Model / Detailed FE Model	VE	1800	Fiber	ε_{11}	2.43%	2.49%	4.45%
				ε_{22}	2.05%	1.82%	5.52%
			Transverse	ε_{11}	1.67%	1.79%	4.86%
				ε_{22}	1.99%	2.03%	5.37%
	VE+VP	1800	Fiber	ε_{11}	2.42%	2.49%	4.46%
				ε_{22}	2.05%	1.82%	5.54%
			Transverse	ε_{11}	0.02%	6.31%	5.02%
				ε_{22}	0.31%	3.90%	5.69%

Table 3.6 Percent difference of the strains from the unit-cell and FE micromechanical models with uniform detailed fiber arrangements

Loading Direction	Model		$V_f = 40\%$	$V_f = 54\%$	$V_f = 67\%$	$V_f = 75\%$
Axial Loading	ε_{11} [mm/mm]	Unit-Cell	1.08E-04	8.01E-05	6.51E-05	5.79E-05
	(1800 s)	Detailed FE	1.11E-04	8.21E-05	6.68E-05	5.94E-05
	% Difference		2.53%	2.54%	2.53%	2.53%
Transverse Loading	ε_{22} [mm/mm]	Unit-Cell	1.73E-03	1.26E-03	9.17E-04	7.27E-04
	(1800 s)	Detailed FE	1.77E-03	1.34E-03	9.87E-04	7.58E-04
	% Difference		2.47%	6.05%	7.12%	4.10%
Number of Elements			244590	240630	234360	247290
Fiber Arrangement			12x12	13x15	15x16	15x18
Arrangement Ratio			1	0.867	0.938	0.833

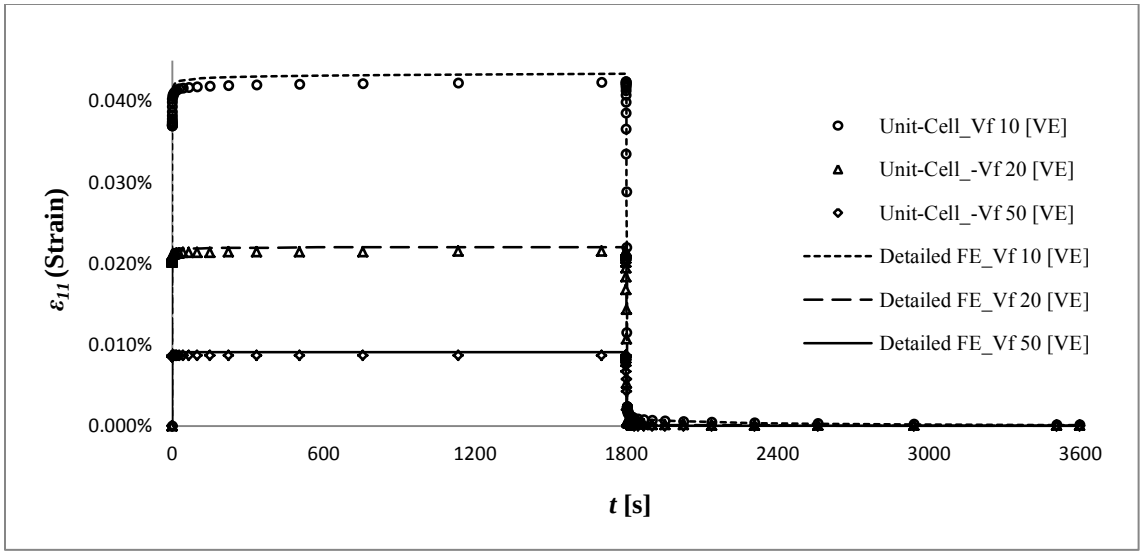

(a) creep recovery strain for fiber direction loading [10MPa]

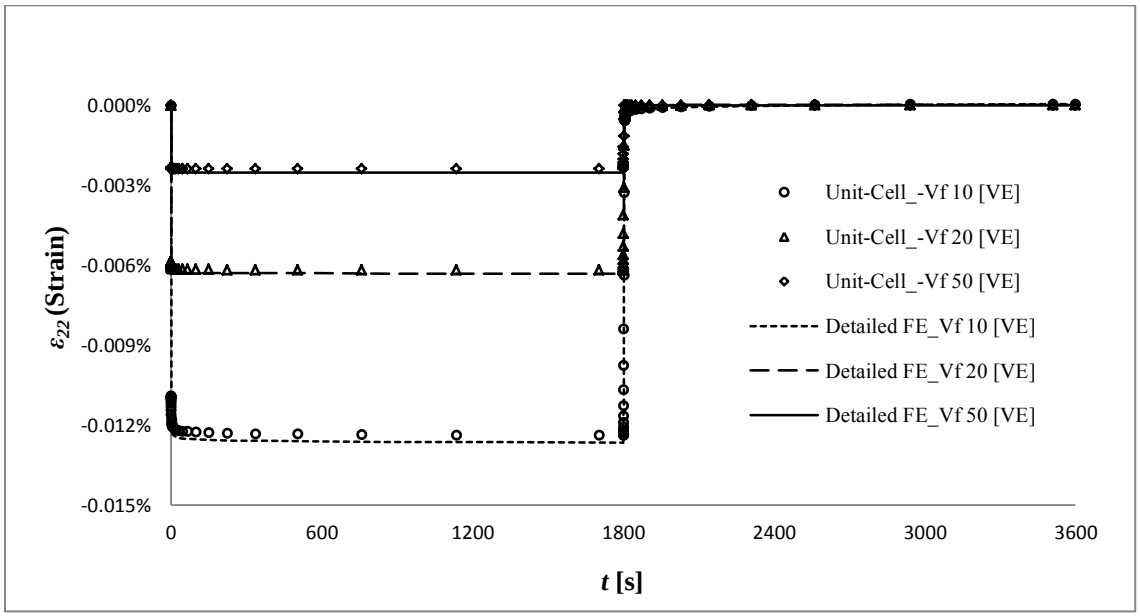

(b) creep recovery strain for corresponding fiber direction loading [10MPa]

Figure 3.8 Creep-Recovery for VE in fiber direction loading

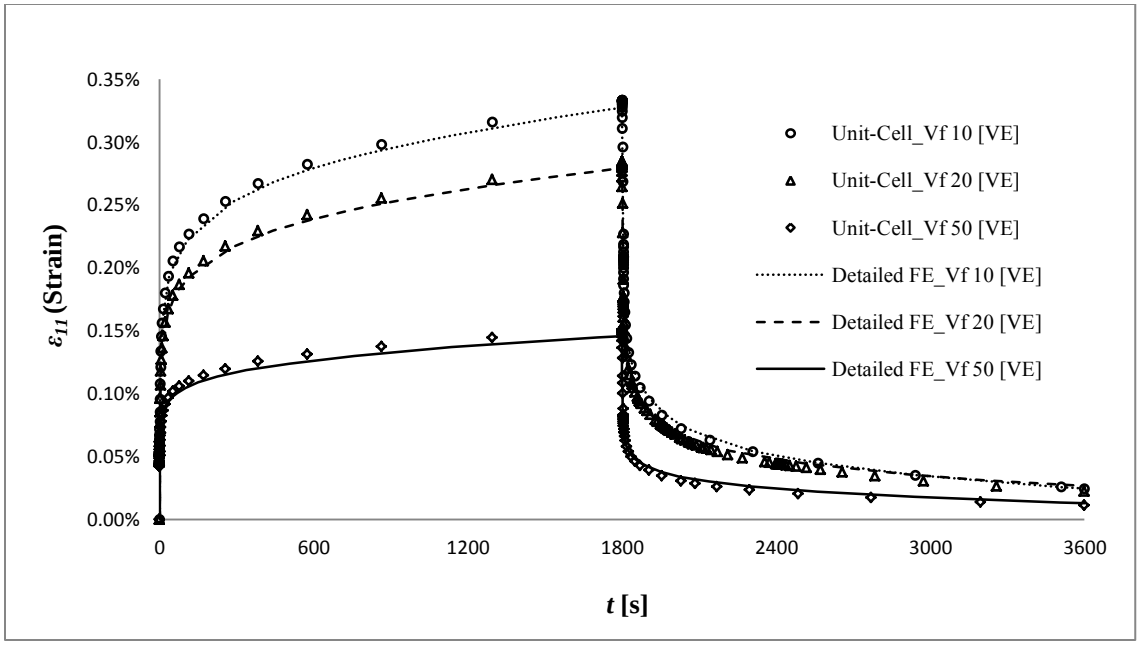

(a) creep recovery strain for transverse direction loading [3MPa]

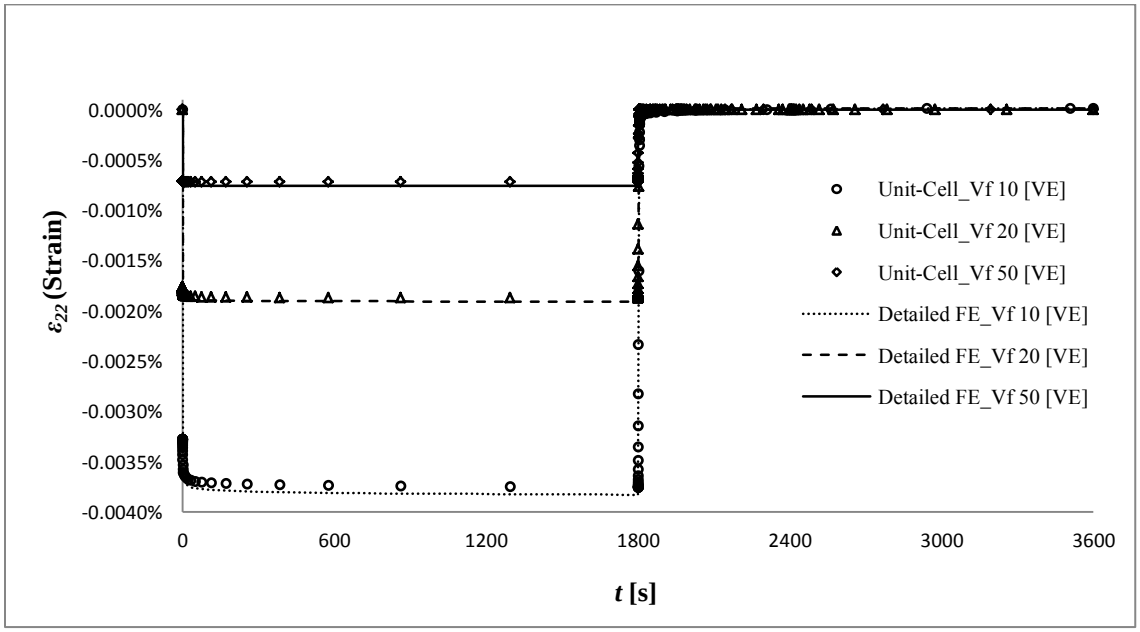

(b) creep recovery strain for corresponding transverse direction loading [3MPa]

Figure 3.9 Creep-Recovery for VE in transverse direction loading

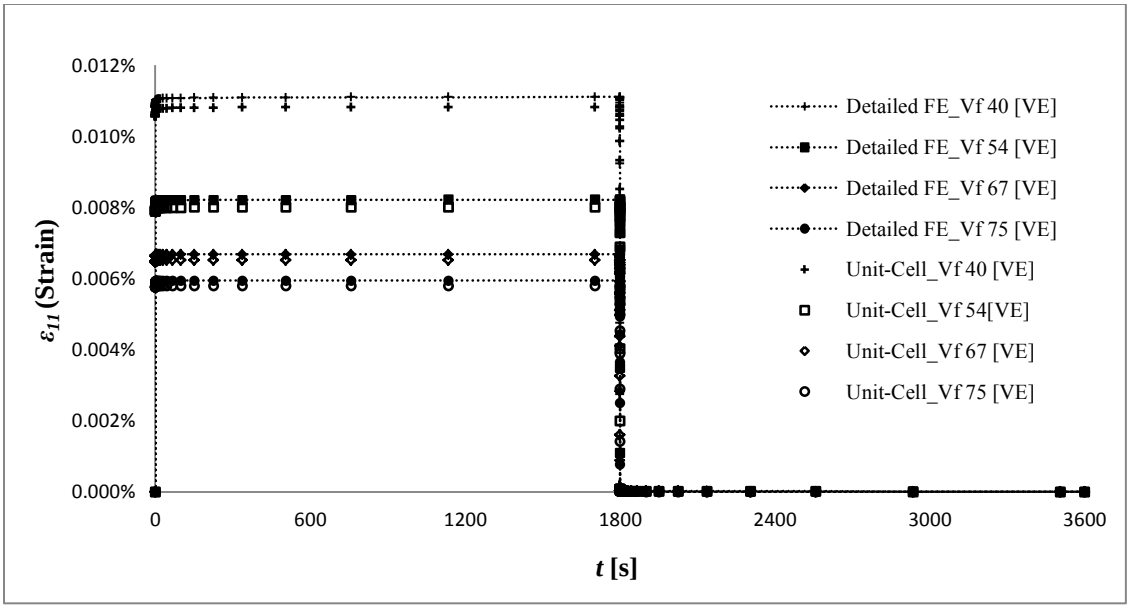

(a) creep recovery strain for fiber direction loading [10MPa]

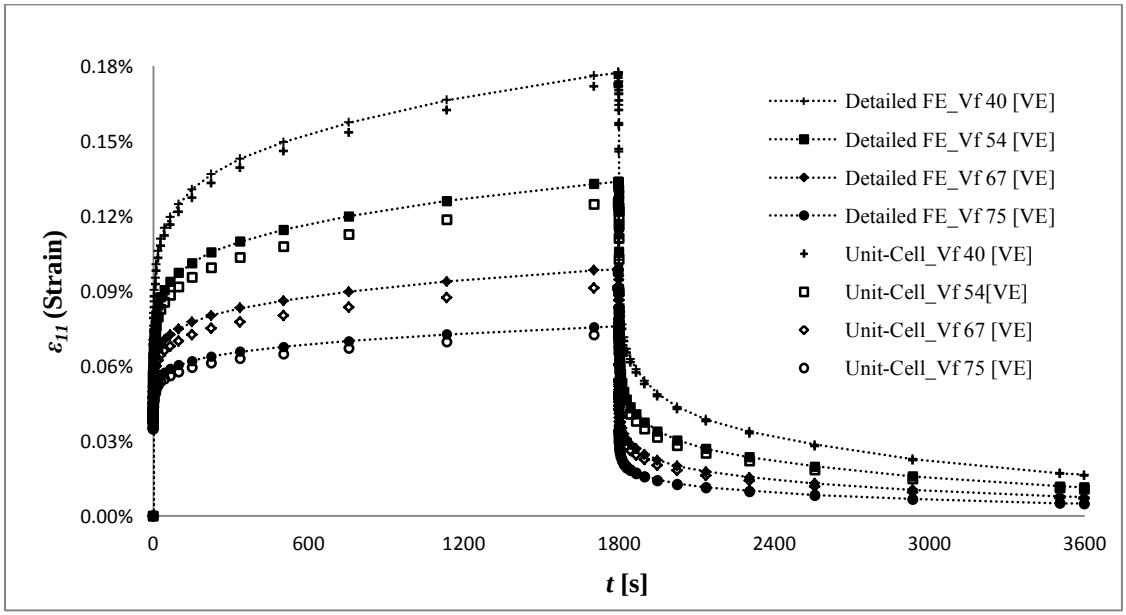

(b) creep recovery strain for transverse direction loading [3MPa]

Figure 3.10 Creep-Recovery for VE in along and transverse to the fiber direction loading

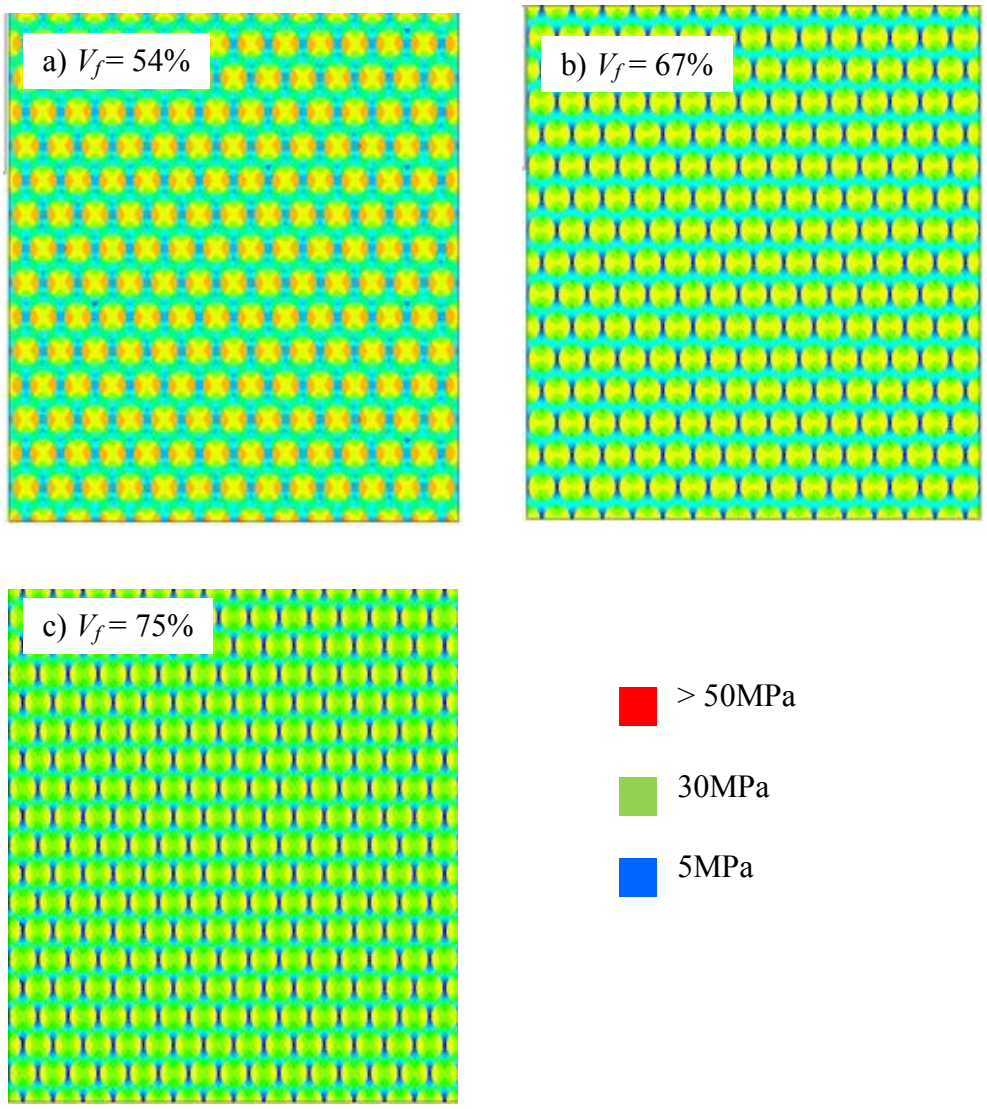

Figure 3.11 Stress contours of composites with 54, 67 and 75% fiber volume contents loaded in the transverse fiber direction for creep behavior at 1800 seconds

Figure 3.12 shows the comparisons of the strains in the UC and micromechanical models with detailed fiber arrangements considering VE and VE-VP behaviors under 10MPa applied along the axial fiber direction. The responses are obtained for composites with 10, 20, and 50% fiber volume contents. Again due to

relatively small amounts of stresses experienced by the matrix, insignificant VP deformations are observed as seen by the nearly similar VE and VE-VP responses. However, when the load 3MPa is applied in the transverse fiber direction, as shown in Figure 3.13, the effect of time-dependent and inelastic response on the overall performance of FRP becomes significant. The higher the fiber volume fraction is, the less the time-dependent and inelastic effects are, which should be expected. Table 3.5 also presents percent difference in the corresponding strains from the UC and FE microstructural models. Consistent with the elastic moduli, the differences (in percent) of the effective time-dependent and inelastic strains obtained of the two models generally increase with increasing the fiber volume contents from 10% to 50%. It is noted that for the 20% fiber volume fraction, the percent difference in the effective time-dependent and inelastic strains of two models are slightly larger than the one of the 50% fiber volume fraction which could be due to arrangement of fibers. Further investigation on understanding the effect of microstructural arrangements on the overall response of the FRP composites is necessary by varying the fiber distributions and sizes, and conducting statistical analysis, which are not the scope of this study. This study highlights that the localized stresses within the microstructures of the composites can influence the overall response of the composites.

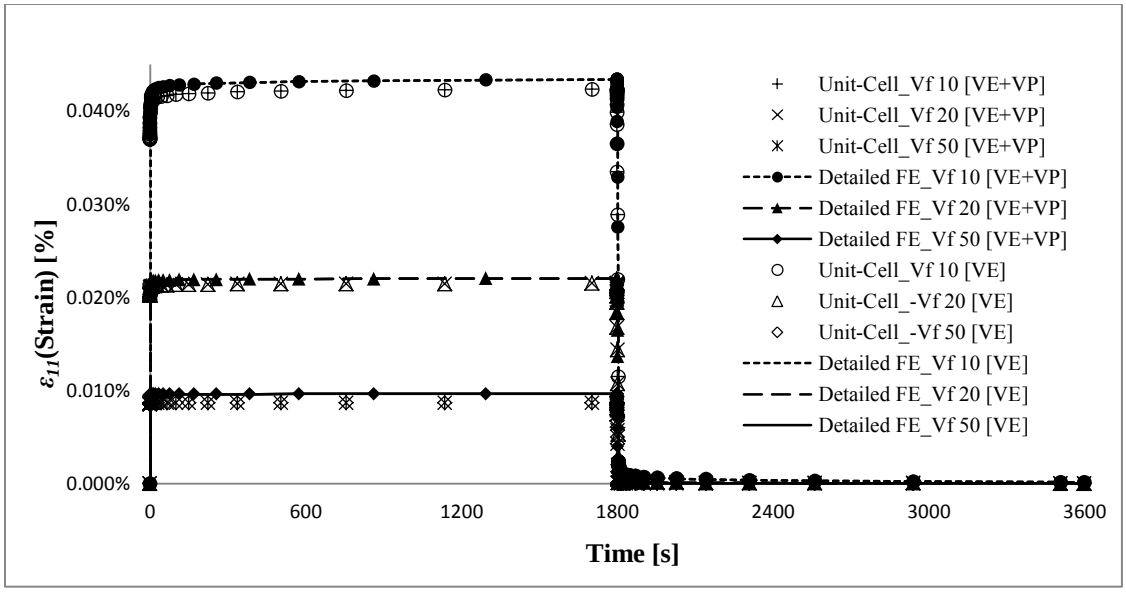

(a) creep recovery strain for fiber direction loading [10MPa]

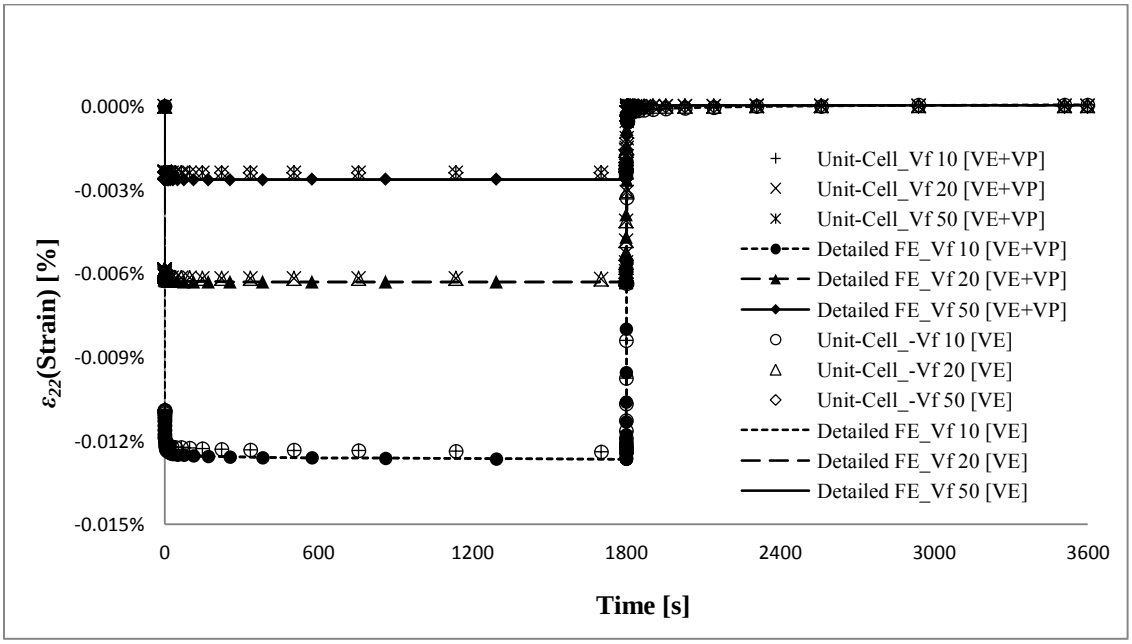

(b) creep recovery strain for fiber direction loading [10MPa]

Figure 3.12 Creep-Recovery for VE and VE-VP response in fiber direction loading

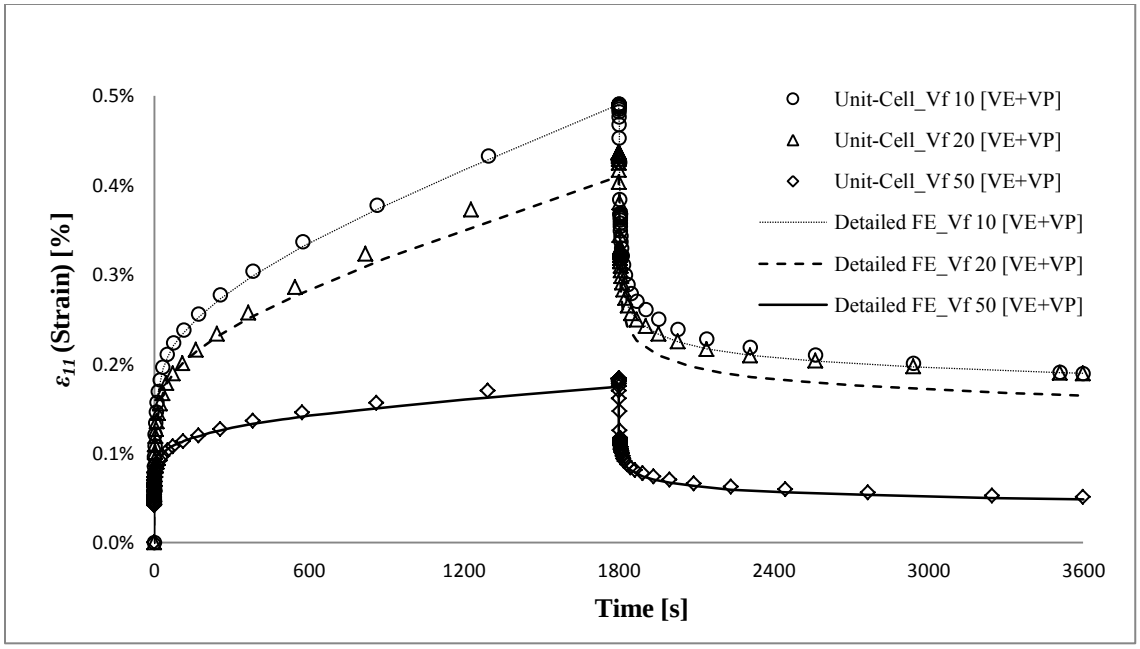

(a) creep recovery strain for transverse direction loading - VE+VP [3MPa]

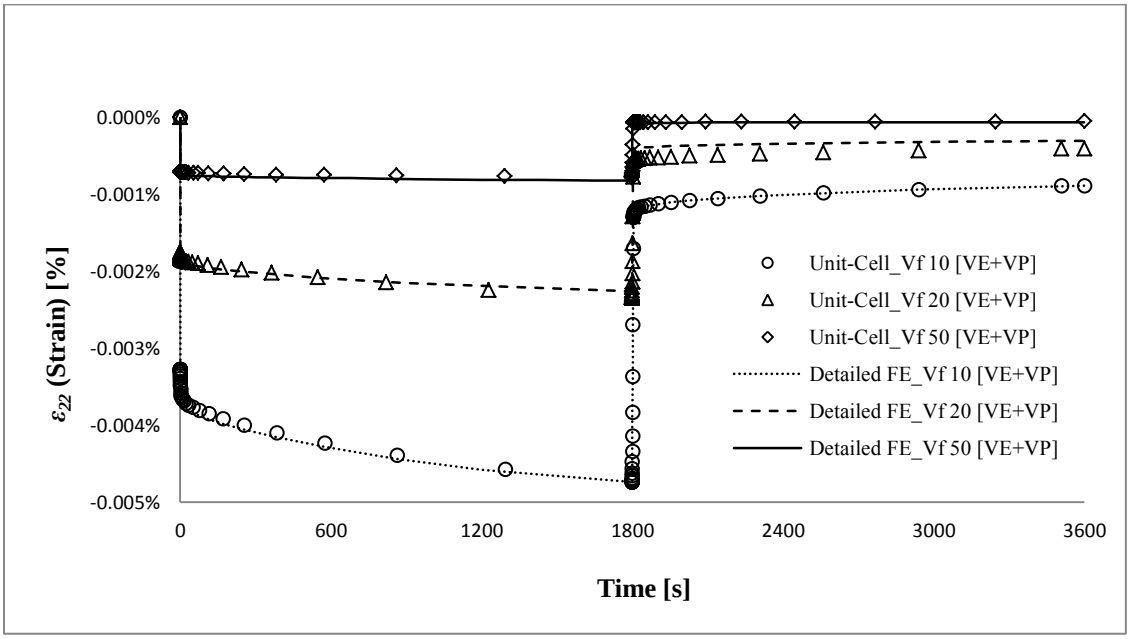

(b) creep recovery strain for transverse direction loading - VE+VP [3MPa]

Figure 3.13 Creep-Recovery in transverse direction loading for VE-VP response

3.4 Numerical Verification of Unit-cell Micromechanical Model with Experimental Data for Unidirectional FRP Composite

Experimental data on the VE-VP response of glass FRP unidirectional composites reported by Megnis and Varna (2003) are used to verify the simplified unit-cell micromechanical model. The tests were performed on several off-axis specimens: 20^o, 30^o, 45^o, 90^o and 0^o, and stress levels. The linear elastic properties of the E-glass fiber in the fiber direction were obtained from Matweb (1997). The elastic properties of the fibers in the transverse direction and the linear elastic modulus of the matrix, epoxy, were calibrated by fitting the instantaneous response of the 0^o and 90^o creep tests in Figures 3.14-3.16. To calibrate the shear modulus of the linear elastic fibers, the instantaneous strains from the off-axis creep tests, i.e., 20^o, 30^o, and 45^o fibers shown in Figures 3.17-3.19 were used. The properties of fiber and polymer matrix are shown in Table 3.7. The time-dependent extensional compliance for the linear viscoelastic matrix is given in Table 3.8. These properties were calibrated by fitting the compliance data under a small stress loading reported in Megnis and Varna (2003). The VP parameters in the Perzyna's model were characterized by fitting the shear strain experimental data of the off-axis specimens at high stress levels shown in Figures 3.17-3.19. The initial yield stress σ_y^0 is taken as 27.876MPa. The calibrated values of the fluidity η_p and the power n are 0.9 [MPa/s] and 1.2, respectively. The stress dependent hardening parameters $h(\bar{\sigma}^t)$ are shown in Figure 3.14. In this study, we take the viscosity parameter constant, while the rate of plastic deformation can vary with stresses. The non-constant hardening parameters are associated with the rates of plastic deformation during the creep tests, as

discussed by Kim and Muliana (2009). An alternative model could have been done by considering the following form of the magnitude of the VP strain rate $\dot{\lambda} = \frac{1}{\eta_p(\bar{\sigma})}\langle \Phi(F) \rangle e^{-\frac{t}{\eta_p(\bar{\sigma})}}$, in which the fluidity parameter depends on the effective stress.

The remaining data of the off-axis specimens that were not used in the calibration are used to validate the micromechanical model. It is seen in Figure 3.15 that creep response of the uniaxial specimen under 130MPa shows nearly elastic response. The plots are shown for the axial and corresponding transverse strains. Since the fibers carry most of the external load the overall VE-VP response is negligible. The creep response of the transverse specimen (90^o) under 50MPa stress is illustrated in Figure 3.16. The micromechanical model with only a VE effect is sufficient in capturing the experimental strains, which is due to a relatively low stress applied to the composites. The fiber volume content of the composite is 56%, resulting in smaller stress transferred to the polymeric matrix and insignificant VP effect. The VP effect is more pronounced for the off-axis composites, i.e., 20^o, 30^o, and 45^o, loaded under sufficiently high stresses shown in Figures 3.17-3.19. It is seen that the micromechanical model with only viscoelastic effect underestimates the creep response. The significant VP effect is due to a relatively high effective stress in the matrix when the shear deformation is pronounced like in the off-axis composite specimens, as also stated in Varna et al. (1997, 1999). Percent errors between the experimental data and VE-VP micromechanical model are reported in Table 3.9. The values were calculated at the last data point. The percent errors of the off-axis specimens are generally higher than the ones of the uniaxial and

transverse specimens. The reason could be due to the VP material parameters, which were calibrated by matching the overall off-axis creep response of the composites. It is perhaps necessary to characterize the VP properties of the epoxy matrix by conducting a series of creep-recovery test of this matrix like the one studied by Lai and Bakker (1995). Nevertheless, the present micromechanical model is capable of predicting the VE-VP response of the FRP composites experiment data at various off-axis angle and stress levels.

Table 3.7 Elastic properties of fiber and polymer matrix

Mechanical Properties of E-Glass Fibers							Epoxy Matrix	
V_f	E_{11}	$E_{22}=E_{33}$	$v_{12}=v_{13}$	v_{23}	$G_{12}=G_{13}$	G_{23}	E	v
[%]	[GPa]	[GPa]			[GPa]	[GPa]	[GPa]	
56	72	32	0.2	0.2	38	38	4.25	0.448

Table 3.8 Time-dependent compliance of the polymeric matrix

n	D_n x 10^{-5} [S^{-1}]	λ_n [MPa^{-1}]
1	3.85	1
2	3.851	1.7 x 10^{-1}
3	3.852	1.8 x 10^{-2}
4	3.853	8.0 x 10^{-4}
5	3.854	1.0 x 10^{-4}
6	3.855	1.0 x 10^{-5}

Table 3.9 Percent errors between experiment data and VE+VP micromechanical model

Time [h]	Loading Angles	Strain	Experiment Data	VE+VP Model	Error [%]
381	0 ° (From Fiber Direction)	ε_{11}	0.0032	0.0031	2.25
		ε_{22}	-0.001	-0.001	0.07
410	90 ° (From Fiber Direction)	ε_{11}	0.0042	0.0042	0.09
		ε_{22}	-0.0004	-0.0004	3.64
380	45 ° (From Fiber Direction)	ε_{11}	0.0054	0.0051	5.11
		ε_{12}	-0.0023	-0.0025	8.02
403	30 ° (From Fiber Direction)	ε_{11}	0.0113	0.0098	12.91
		ε_{12}	-0.0127	-0.0138	9.43
380	20 ° (From Fiber Direction)	ε_{11}	0.0059	0.005	15.97
		ε_{12}	-0.0069	-0.0074	6.76

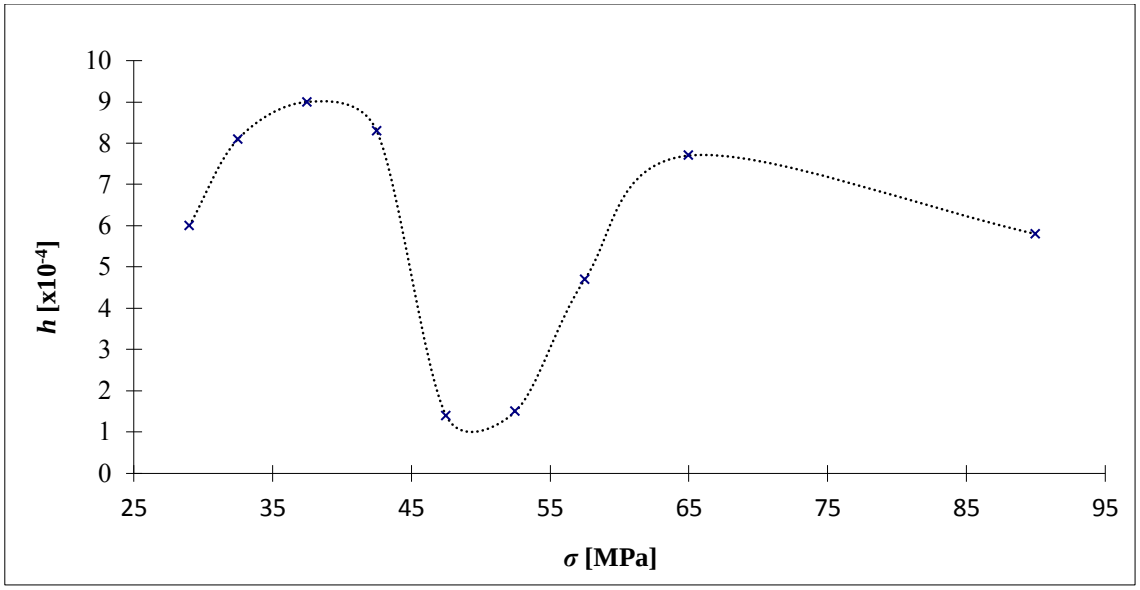

Figure 3.14 Hardening parameters of Perzyna model (calibrated from the viscoplastic creep strains)

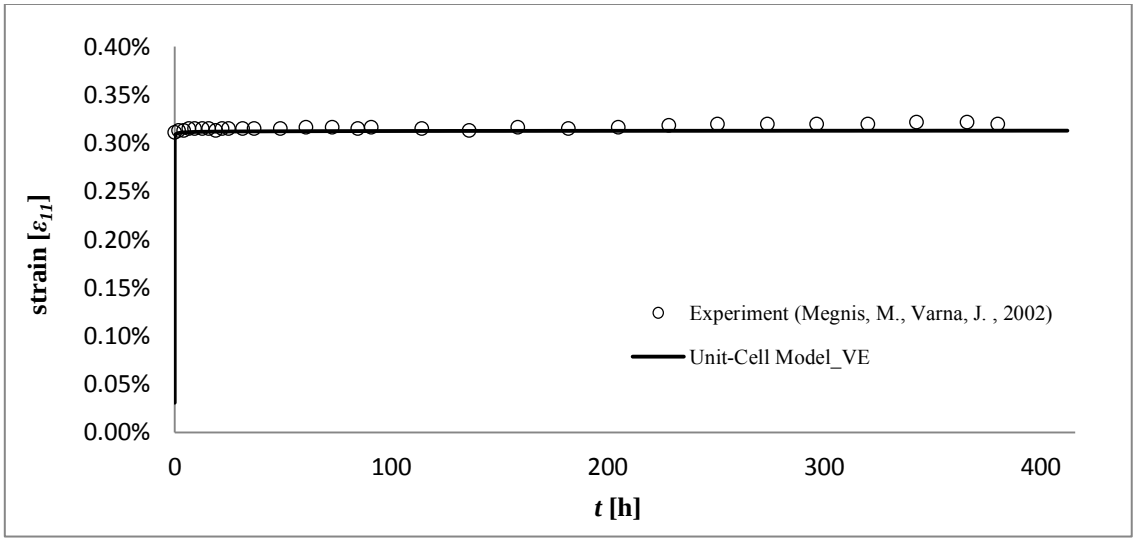

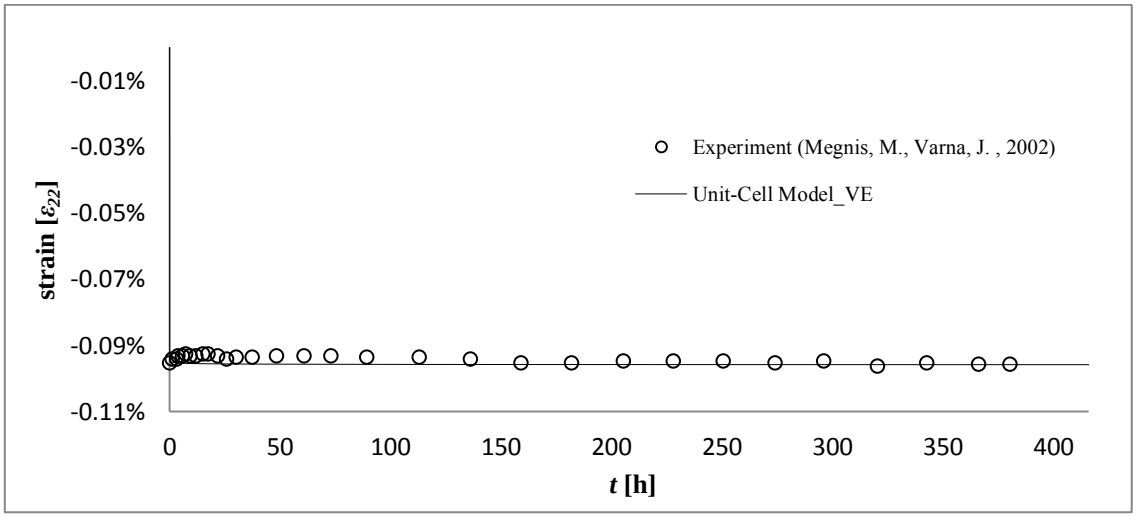

Figure 3.15 Creep strain for $[0]_m$ laminate. (o) experiment strain data, (—)calculated viscoelastic strain. Applied stress [130MPa] (fiber direction).

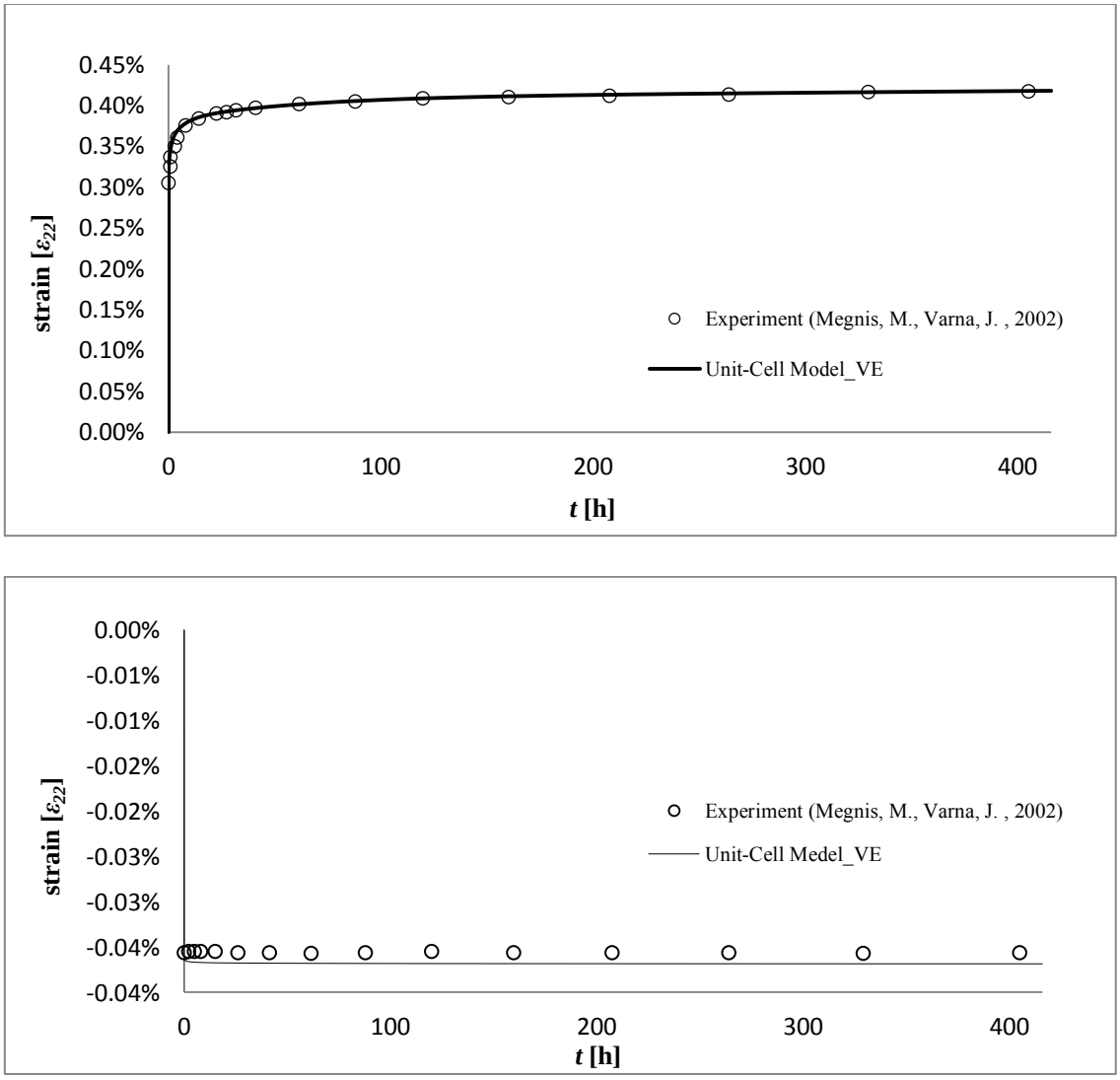

Figure 3.16 Creep strain for $[90]_m$ laminate. (o) experiment strain data, (—)calculated viscoelastic strain. Applied stress [50MPa] (Transverse of fiber direction).

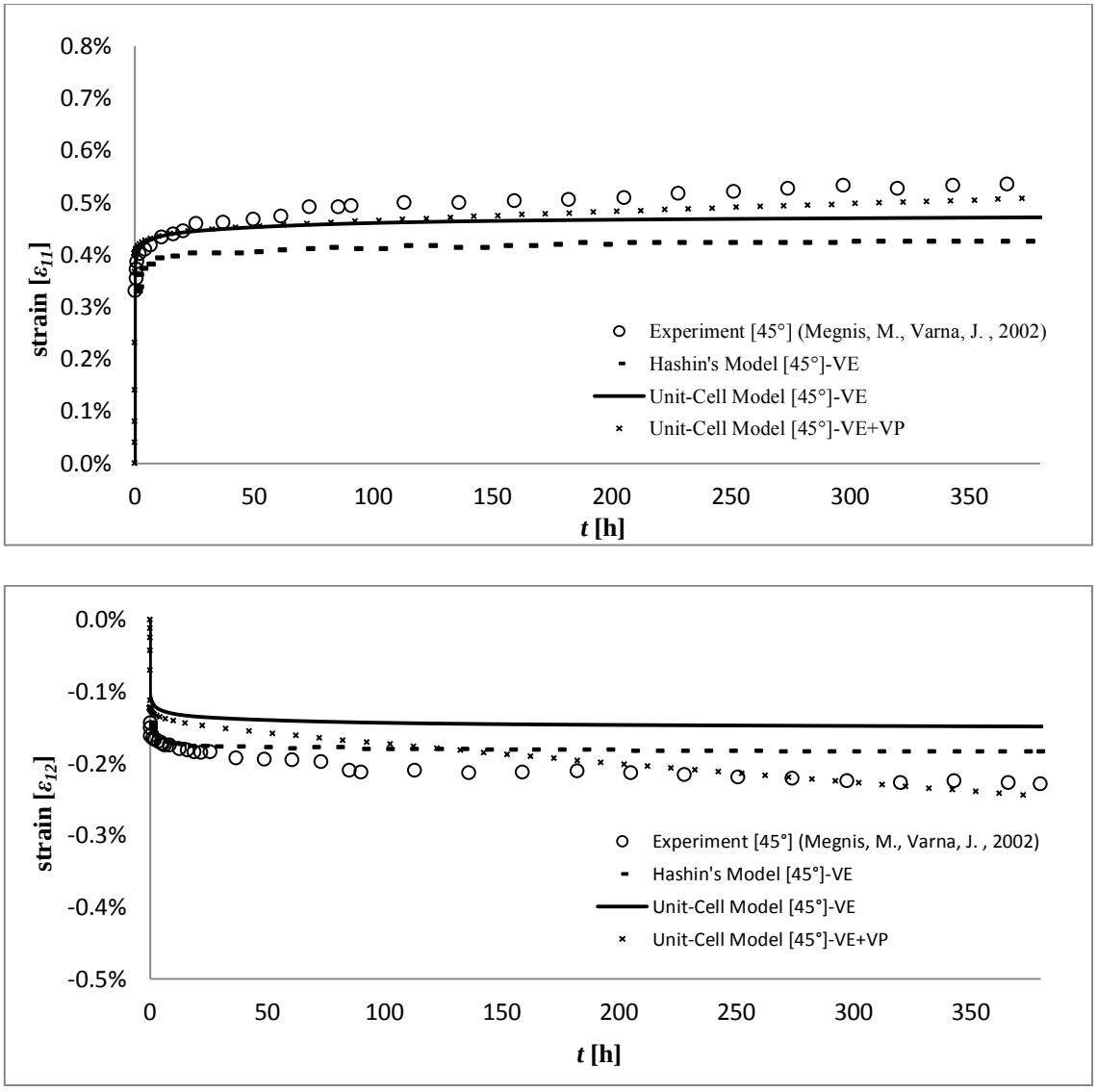

Figure 3.17 Creep strain for $[45]_m$ laminate. Applied stress [50MPa] is local direction

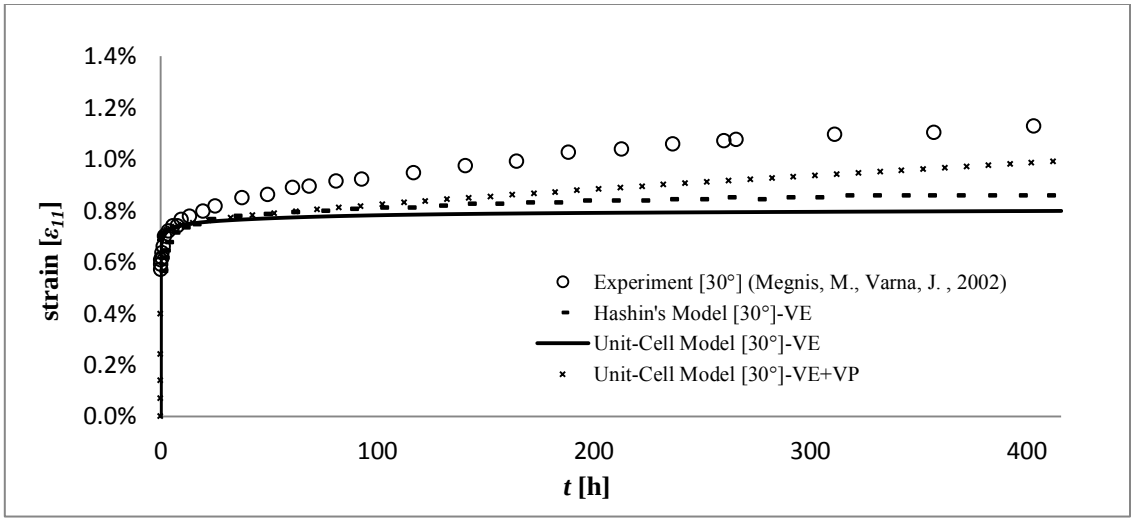

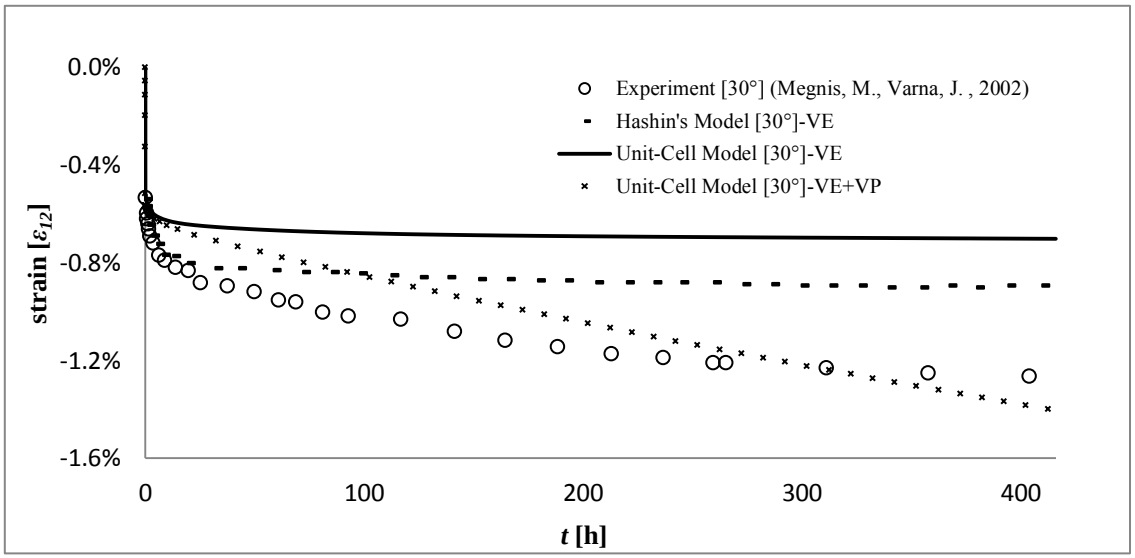

Figure 3.18 Creep strain for $[30]_m$ laminate. Applied stress [115MPa] is local direction

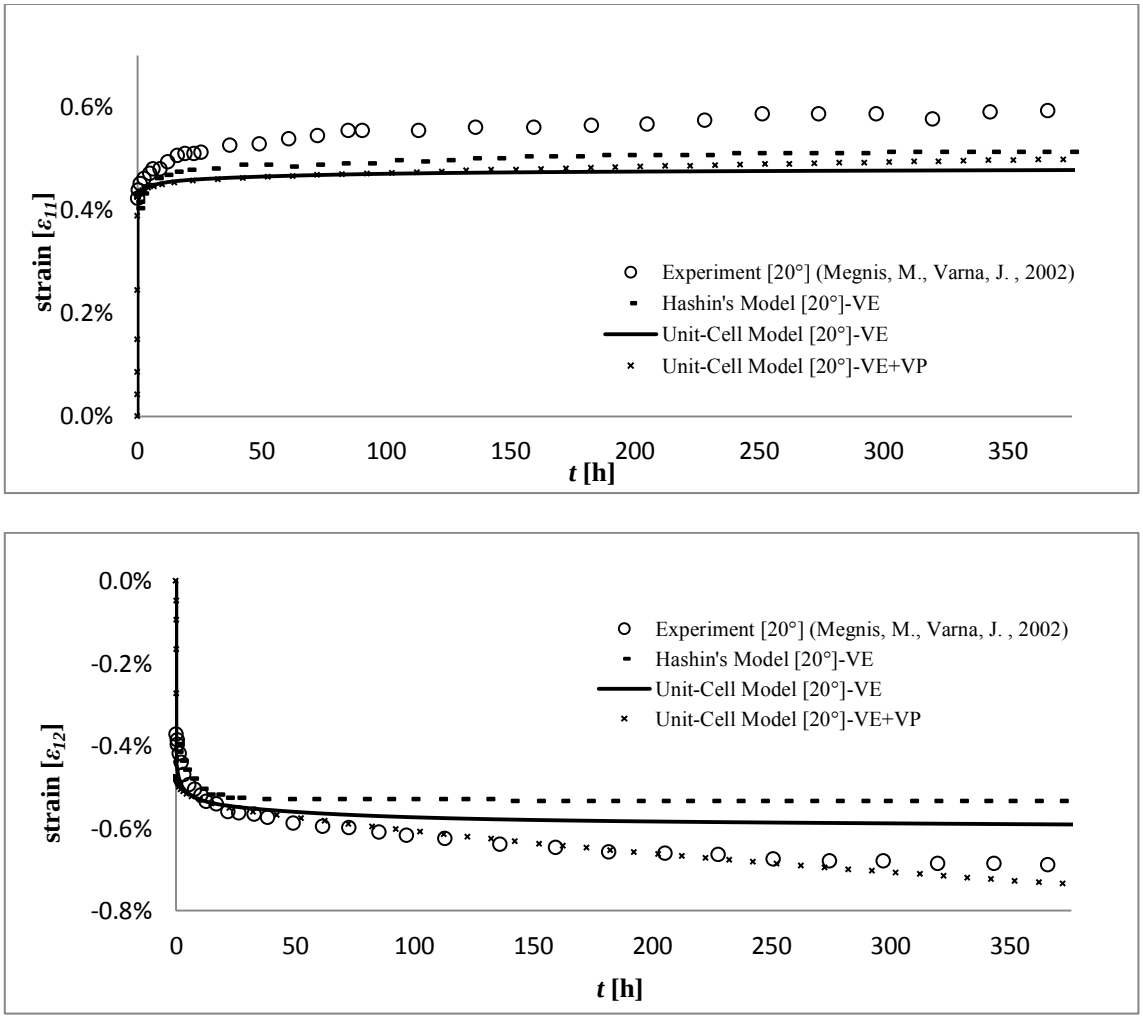

Figure 3.19 Creep strain for $[20]_m$ laminate. Applied stress [100MPa] is local direction

CHAPTER IV

COUPLED MECHANICAL AND THERMAL ANALYSES OF FRP COMPOSITES

Fiber reinforced polymer (FRP) composites are widely used in many engineering applications involving wide temperature changes such as in aircraft structural components, turbine blades, retrofitting nuclear reactor containment concrete structures, etc. Under external mechanical loadings and extreme temperature changes the FRP composites experience coupled thermal-mechanical responses. For example, temperature changes in FRP composites lead to internal thermal stresses in the fiber and polymeric matrix; at elevated temperatures the polymeric matrix show pronounced viscoelastic or viscoplastic response that causes stress relaxation (and simultaneous creep deformation) in the polymeric matrix; and continuous changes of the stress fields in the matrix constituent influence the overall performance of FRP structures. The existence of high thermal stresses might result in formation of cracks and/or inelastic deformations in the constituents. Understanding the effect of temperature changes on the overall performance of FRP composites becomes important for better designing FRP composite materials and structures.

This chapter presents analyses of coupled heat conduction and deformations in FRP composites through the use of integrated micromechanical models and FE method. Micromechanical models presented in Chapter III are modified for determining the effective (overall) thermal and mechanical properties of the FRP composites. These micromechanical models are implemented within continuum elements in FE framework.

The first section of this chapter discusses micromechanical formulation for heat conduction analyses in FRP composites, followed by micromechanical models for thermo-mechanical deformations.

4.1 Heat Conduction Analyses of FRP Composites

4.1.1 Micromechanical formulation of heat conduction

The unit-cell model, discussed in Chapter III, is now used for determining the thermal properties and analyzing heat conduction in FRP composites. The unit-cell model consists of four fiber and matrix subcells and a volume averaging scheme is used to obtain the average (effective) field variables of the FRP composites. The spatial variation of the temperature gradient and heat flux vectors in each subcell is assumed uniform. The volume averaged heat flux and temperature gradient are given as:

$$\bar{q}_i = \frac{1}{V}\sum_{m=1}^{N}\int_{V^{(m)}} q_i^{(m)}(x_k^{(m)})\, dV^{(m)} \approx \frac{1}{V}\sum_{m=1}^{N} V^{(m)} q_i^{(m)} \qquad \text{,where } i,k = 1,2,3 \tag{4.1}$$

$$\bar{\varphi}_i = \frac{1}{V}\sum_{m=1}^{N}\int_{V^{(m)}} \varphi_i^{(m)}(x_k^{(m)})\, dV^{(m)} \approx \frac{1}{V}\sum_{m=1}^{N} V^{(m)} \varphi_i^{(m)} \qquad \text{,where } \bar{\varphi}_i = \frac{\partial \bar{T}}{\partial x_i} \tag{4.2}$$

$q_i^{(m)}$ is the component of the heat flux in subcell (m), $\varphi_i^{(m)}$ is the component of the temperature gradient and N is the number of subcells. The variables $\bar{q}$ and $\bar{\varphi}$ are the effective heat flux and temperature gradient, respectively. It is assumed that the Fourier law governs the heat conduction in the composites; the dissipation in the composites, the

radiation, and the velocity of the composite bodies can be ignored. The transient heat conduction in the composite media is governed by the following equation:

$$\overline{\rho c}\,\frac{d\overline{T}}{dt} = -\overline{q}_{i,i} \tag{4.3}$$

The effective heat capacity $\overline{\rho c}$ is assumed as:

$$\overline{\rho c} = \frac{1}{V}\sum_{m=1}^{N}\int_{V^{(m)}} \rho c^{(m)}(x_k^{(m)})\, dV^{(m)} \approx \frac{1}{V}\sum_{m=1}^{N} V^{(m)}\rho c^{(m)} \tag{4.4}$$

The above equation for the heat conduction will be solved incrementally:

$$\overline{\rho c}\,\frac{d\overline{T}}{dt} \approx \overline{\rho c}\,\frac{\Delta\overline{T}^{t}}{\Delta t}; \quad \overline{T}^{t} \approx \overline{T}^{t-\Delta t} + \Delta\overline{T}^{t} \tag{4.5}$$

The superscript in the above equation indicates the time associated to the field variables. The incremental form of the effective heat flux at the current time is:

$$\overline{q}_i^{t} \approx \overline{q}_i^{t-\Delta t} + \Delta\overline{q}_i^{t} \tag{4.6}$$

The incremental form of the heat flux linearized constitutive equation of the composite is:

$$\Delta\overline{q}_i^{t} = -\overline{K}_{ij}^{t}\Delta\overline{\varphi}_j^{t} \tag{4.7}$$

where $\overline{K}_{ij}^{t}$ is the components of the effective thermal conductivity tensor which can depend on current temperature and $\Delta\overline{\varphi}_j^{t} = \dfrac{\partial\Delta\overline{T}^{t}}{\partial x_j}$ is the incremental temperature gradient.

The micromechanical formulation is expressed in terms of linearized incremental relations. In order to relate the effective field variables to the field variables in each

subcell, the concentration matrix $F_{ij}^{(m)}$ will need to be formulated as discussed in Chapter III:

$$\Delta\varphi_i^{(m),t} = \mathbf{F}_{ij}^{(m),t}\Delta\bar{\varphi}_j^t \tag{4.8}$$

The incremental heat flux in each subcell is related to the incremental temperature gradient in each subcell through the subcell's thermal conductivity:

$$\Delta q_i^{(m),t} = -k_{ij}^{(m),t}\Delta\varphi_j^{(m),t} \tag{4.9}$$

Using Eqs. (4.8), (4.9) and the volume averaging scheme in Eq. (4.1), the effective thermal conductivity in the composite is expressed as:

$$\overline{K}_{ik}^t = \frac{1}{V}\sum_{m=1}^{N} V^{(m)} k_{ij}^{(m),t}\mathbf{F}_{jk}^{(m),t} \tag{4.10}$$

In order to define the concentration matrix $\mathbf{F}_{ij}^{(m)}$ for the FRP composites, the micromechanical relations and constitutive equations for all subcells are imposed. Detailed micromechanical relations for analyzing heat conduction in FRP composites can be found in Muliana and Kim (2010). The above micromechanical models are implemented at each material (Gaussian) point in 3D continuum finite elements which will be used to analyze heat conduction in homogenized composite media. For this purpose a user material subroutine UMATHT of ABAQUS FE code is used.

4.1.2 Numerical Implementation

The above micromechanical models lead to response of FRP composites as homogenized bodies, which give a crude approximation of the field variables (average

values). This will be used for analyzing response of large-scale composite structures. In reality, composites are heterogeneous bodies, whose responses depend strongly on the microstructural characteristics such as sizes, shapes, and arrangements of the inclusions, and the properties of the constituents. The heterogeneity in the microstructures often causes significant localized field variables, such as stress or heat flux concentration at the interfaces between fibers and matrix, which can influence the overall response of the FRP composites. The above micromechanical models can incorporate the detailed nonlinear constitutive models for all constituents and simplified (idealized) geometry of the microstructures in the composites, but they are limited in capturing the effects of detailed microstructural characteristics and localized field variables on the overall response of the composites. In order to examine the response obtained from the simplified micromechanical models to the ones determined with more realistic microstructures, FRP microstructural models with several fibers arranged in the homogeneous matrix are generated for composites with different fiber volume contents (see Figure 4.1 as an example). These FRP microstructural models are meshed using 3D continuum finite elements and FE method is used to obtain solutions in terms of field variables due to prescribed boundary conditions.

The FRP microstructural models with cubic geometries of side length 6 mm are considered. The cross sectional area of one cylindrical fiber is 0.1 mm^2, and the fiber volume fraction is proportional to the volume of the entire fibers to the volume of the cubic medium. The fibers are arranged uniformly in the matrix medium. The studied FRP composites are made of E-glass fiber and epoxy matrix. The transient heat

conduction analyses are performed for FRP with different fiber volume fractions, 10, 20, 40, 50, 67, 75%. For each fiber volume fraction, transient heat conductions along the unidirectional fiber (longitudinal) and transverse to the fiber directions are performed until steady state condition is reached within the given tolerance. The tolerance is defined in terms of temperature gradient $\frac{\partial T}{\partial x_i}$, and steady state condition is numerically achieved when the maximum temperature gradient is less than 0.1 K/mm. The corresponding temperature profiles, $T(x_1, x_2, x_3, t)$, are obtained by solving the following governing equation $\rho c \frac{dT}{dt} = -q_{i,i}$ for the heterogeneous medium and at the interfaces between fibers and matrix, temperature is assumed continuous. The initial and boundary conditions for the heat conduction along the longitudinal and transverse fiber directions are given as follows:

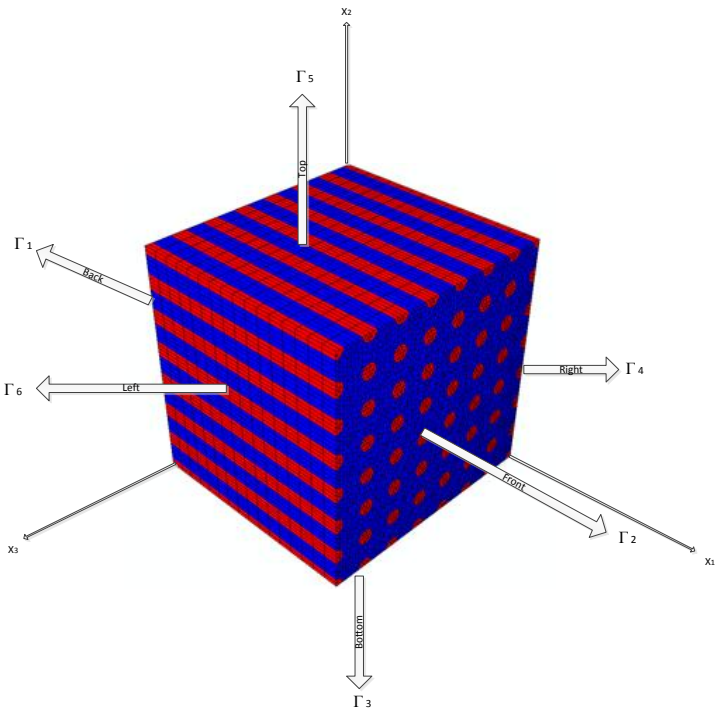

For conduction along the axial fiber direction:

$$T(0, x_2, x_3, t) = 393\text{K}$$

$$T(x_1, x_2, x_3, 0) = 293\text{K}\ ,\ 0 \le x_1, x_2, x_3 \le 6$$

$$\frac{\partial T}{\partial x_i}(x_1, x_2, x_3, t) = 0 \ \text{ on } \ \Gamma_2, \Gamma_3, \Gamma_4, \Gamma_5, \Gamma_6$$

For conduction along the transverse fiber direction:

$$T(x_1, 0, x_3, t) = 393\text{K}$$

$$T(x_1, x_2, x_3, 0) = 293\text{K}\ ,\ 0 \le x_1, x_2, x_3 \le 6$$

$$\frac{\partial T}{\partial x_i}(x_1, x_2, x_3, t) = 0 \ \text{ on } \ \Gamma_1, \Gamma_2, \Gamma_4, \Gamma_5, \Gamma_6$$

Figure 4.1 Surface boundary of microstructure of FRP composites

The properties of the E-glass fiber and epoxy matrix in the FRP composite material are given in Tables 4.1 and 4.2.

Table 4.1 E-glass fiber and epoxy matrix physical properties

Constituents	Density (kg/m^3)	Specific heat (J/kg K)
E-glass	2600	840
epoxy	1250	1110

Table 4.2 E-glass fiber and epoxy matrix thermal conductivity

Thermal Conductivity (W/m K)	k_{11} (longitudinal)	k_{22}=k_{33} (transverse)
E-glass	1.1	1.1
epoxy	0.188	

Heat conduction in the longitudinal (axial) fiber direction

The times to reach steady state condition in the transient heat conduction analyses of FRP composites with several fiber volume contents are presented in Table 4.3. The responses of FRP composites form the simplified micromechanical (unit-cell) model are compared to the ones with detailed microstructural characteristics. The percent differences in the steady state times from the unit-cell model and FRP

micromechanical models with detailed microstructural characteristics are within 2.61%. For low fiber volume fractions, such as 10 and 20%, the simplified unit-cell model shows good agreements with the FRP models with microstructural details. However, for the composites with higher fiber volume fractions higher deviations are observed in the steady state times. It is noted that the thermal conductivity of fibers is higher than that of the matrix; thus, conduction along the fibers tends to be faster than the conduction along the matrix. For the FRP composites with low fiber volume contents, spacing between fibers are relatively large compared to the FRP composites with higher fiber volume contents. In such condition, the influences of heat conduction in the matrix regions between fibers on the overall conduction due to the macroscopic temperature gradients are relatively small. The simplified micromechanical (unit-cell) model does not incorporate the possible effects of heat conductions between fibers. On the other hand, the conduction between fibers might accelerate the overall heat conduction in the composites, indicated by lower steady state time when FRP with microstructural details are considered. For the FRP composites with relatively high fiber volume fractions, the percent differences in the steady state times between the unit-cell models and FRP models with microstructural details become smaller, which might be because the thermal conductivity of the fiber dominates the overall heat conduction in the composite media.

The temperature fields at several instants of time during the transient heat conduction along the axial fiber direction in the FRP composite media are shown in Figure 4.2. The responses of 10% fiber volume fraction, illustrating 3-D temperature distribution, and the cross sections of temperature distribution at several instants of time

are shown for FRP composites with 10, 50, and 75% fiber volume contents. The temperature profiles obtained from the unit-cell model and micromechanical model with microstructural details are in reasonably good agreements. The FRP models with microstructural details show slight waviness in the temperature fields around the fibers due to its capability of capturing variations in the localized temperature profiles from the differences in the thermal conductivities of fibers and matrix. The unit-cell model presents average temperature profiles in homogenized composites.

Table 4.3 Steady state times during transient heat transfer analyses

Direction of heat conduction	Model	Fiber Volume Fraction [%]					
		10	20	40	50	67	75
Steady State time (Axial) [s]	Unit-Cell	220	191.5	157.5	146	131.5	126
	Detailed FE	219	189	153.5	143.5	129	124
% Difference		0.46%	1.32%	2.61%	1.74%	1.94%	1.61%
Steady State time (Trans) [s]	Unit-Cell	263	253.5	226.5	209.5	179	163
	Detailed FE	254	240	214	206.5	173.5	154
% Difference		3.54%	5.63%	5.84%	1.45%	3.17%	5.84%

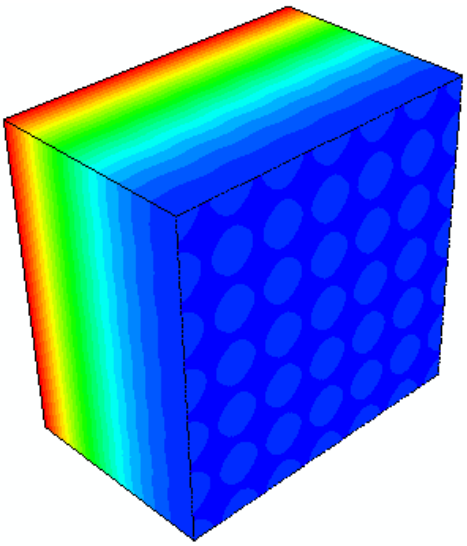

V_f = 10% - AXIAL (3-D Heat Conduction of Detailed FE Model at 10 Seconds)

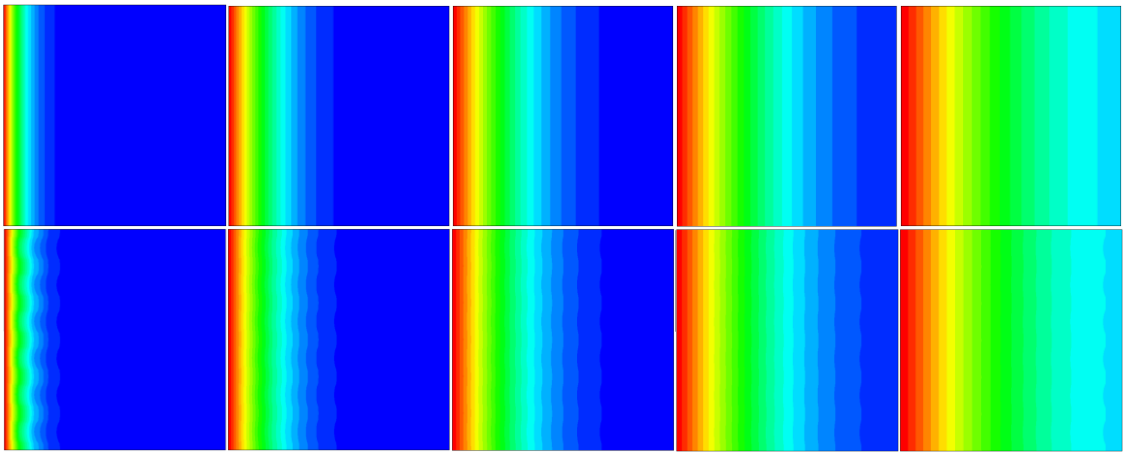

V_f = 10% (AXIAL)

Figure 4.2 Temperature contours for axial heat conduction

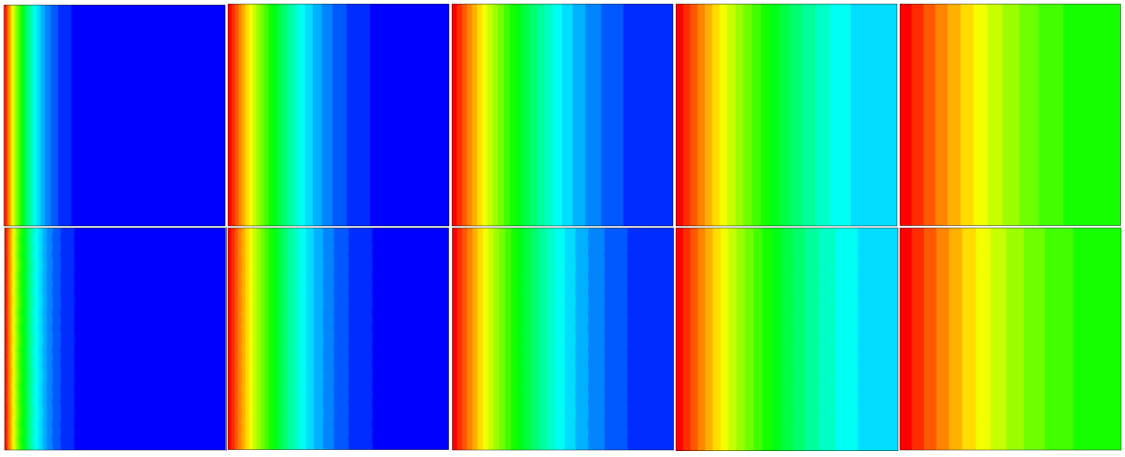

1s 5s 10s 20s 40s

V_f = 50% (AXIAL)

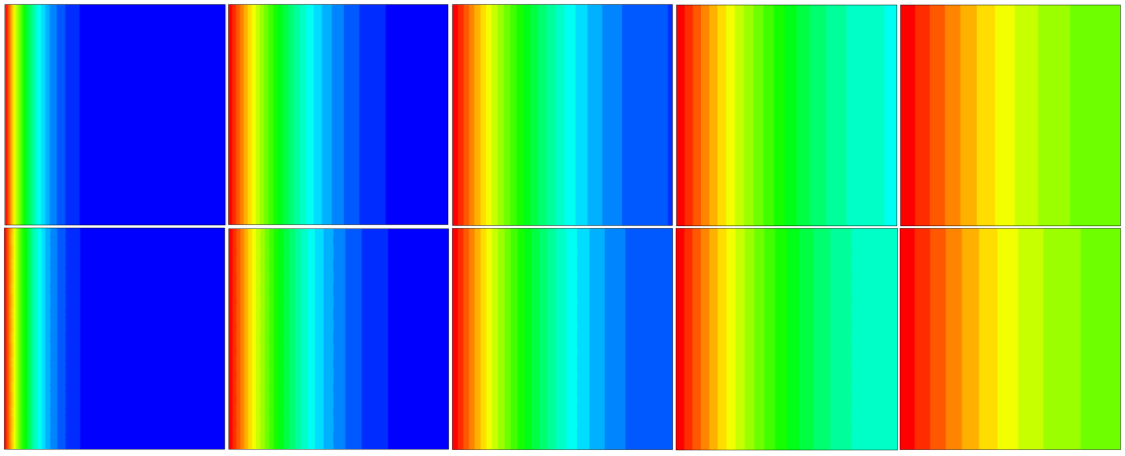

1s 5s 10s 20s 40s

V_f = 75% (AXIAL)

393 K 360 K 320 K 293 K

Figure 4.2 Continued

Heat conduction in the transverse fiber direction

The steady state times for the transient heat conduction along the transverse fiber direction for FRP composites with several fiber volume contents are given in Table 4.3. The calculated steady state times due to conduction along the transverse fiber direction are higher than the ones for the conduction along the axial fiber direction. This is due to the low thermal conductivity of the matrix, which slows down the heat conduction in the transverse fiber direction. The corresponding temperature profiles for FRP composites with 10, 50, and 75% fiber volume contents are illustrated in Figure 4.3. The wavy shapes in the temperature profiles around the fibers are more distinctive due to the matrix thermal resistance. The wavy shapes are more distinctive in lower volume contents. The heat conduction in the matrix regions is relatively slow due to the relatively low thermal conductivity in matrix. The conduction in the fibers occurs faster until it reaches the interface of matrix, which is shown by the wavy shapes. Overall, the temperature profiles generated from the unit-cell model and FRP models with microstructural details are in good agreements. It is concluded that for several case studies presented here, the unit-cell model gives reasonably good averages of the heat conduction performance of the FRP composites.

Figure 4.4 depicts the temperature distributions along the conduction lengths of the FRP composites with different fiber volume contents, corresponding to the temperature field contours in Figures 4.2 and 4.3. It is seen that the temperature distributions from the unit-cell model are comparable to the ones from the micromechanical models with detailed microstructures. However, the unit-cell model

results in smooth and continuous temperature distributions with continuous temperature gradients due to the homogenized responses of the FRP composites.

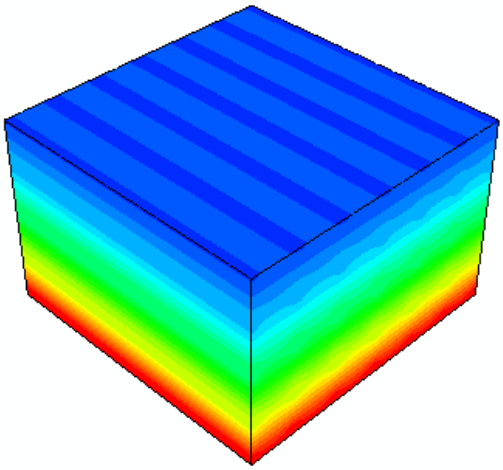

V_f = 10% - TRANS (3-D Heat Conduction of Detailed FE Model at 20 Seconds)

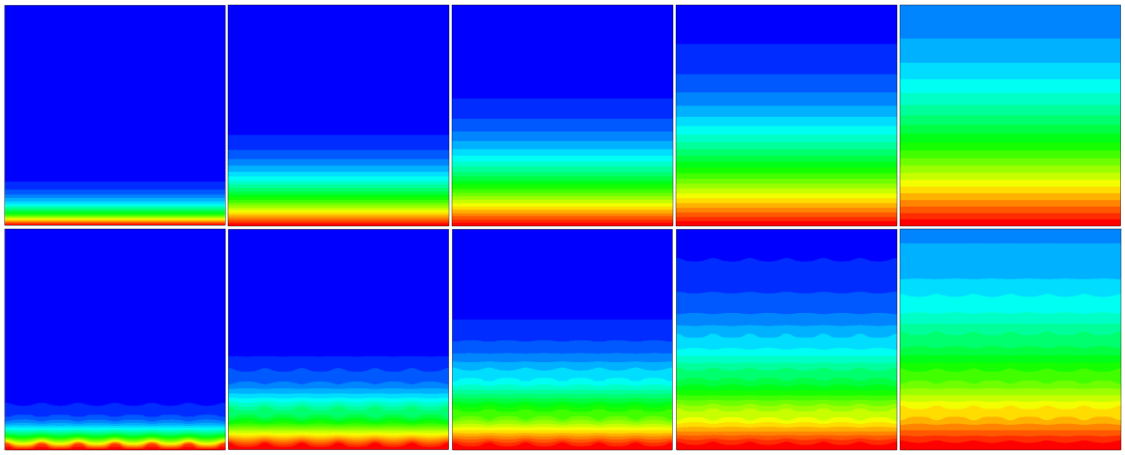

1s 5s 10s 20s 40s

V_f = 10% (TRANS)

Figure 4.3 Temperature contours for transverse heat conduction

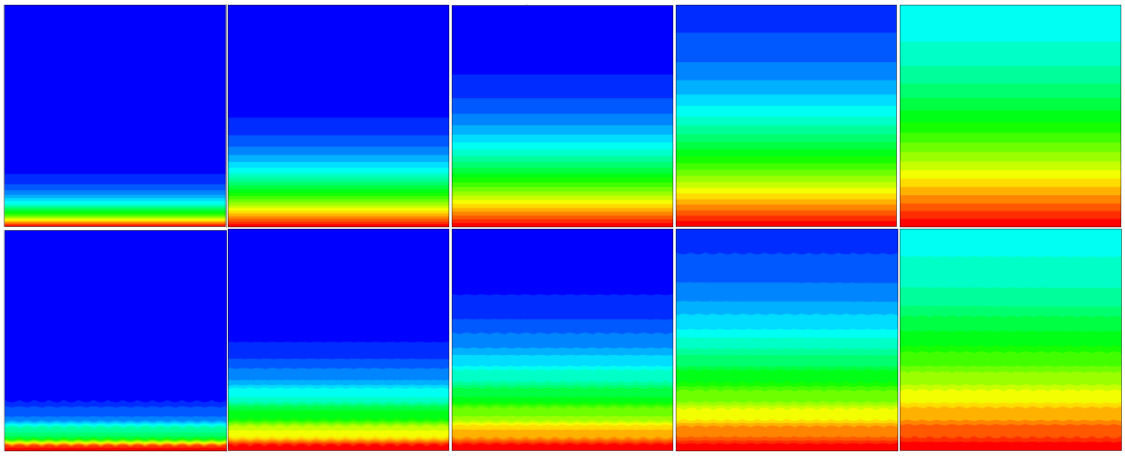

1s 5s 10s 20s 40s

V_f = 50% (TRANS)

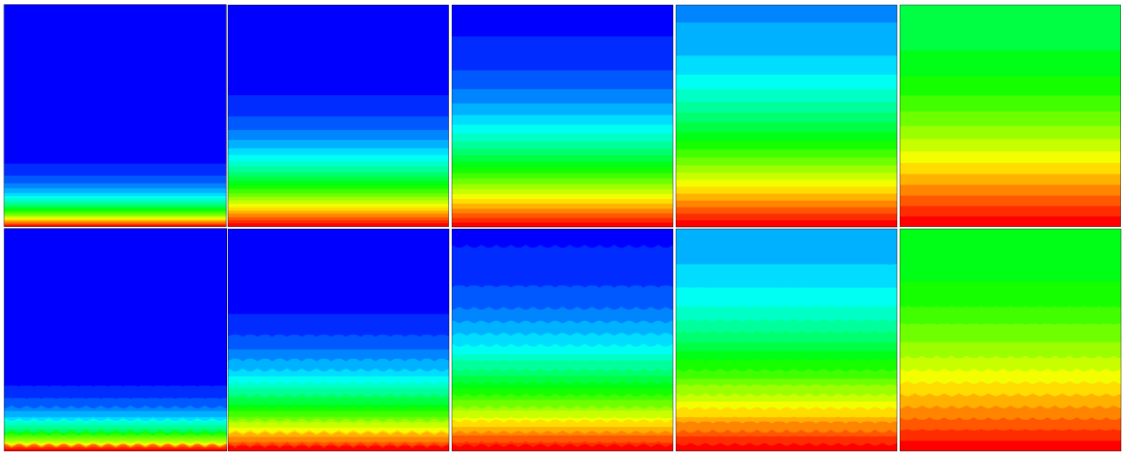

1s 5s 10s 20s 40s

V_f = 75% (TRANS)

Figure 4.3 Continued

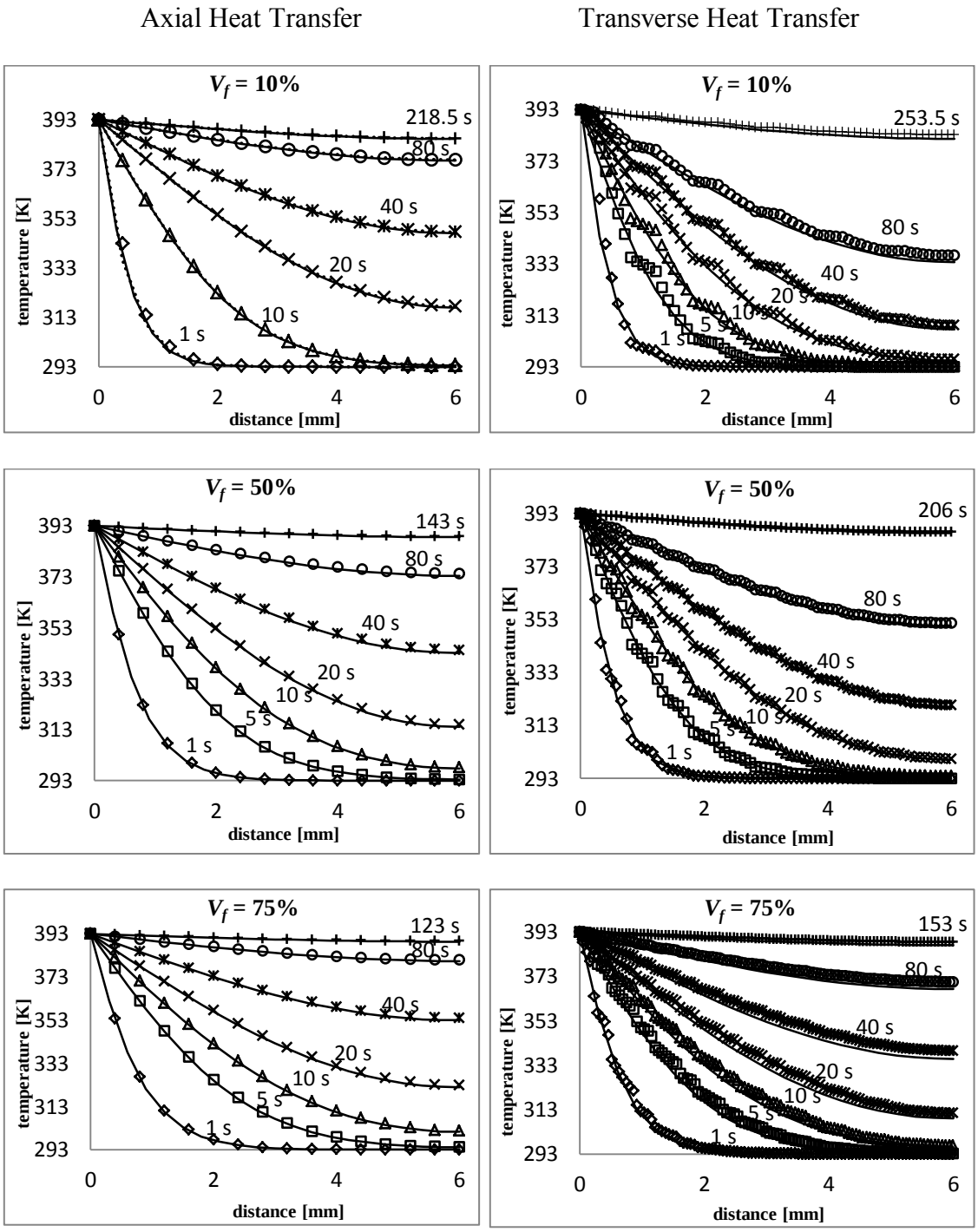

Line : Unit-Cell Model; Symbols : Detailed FE Model

Figure 4.4 Temperature profiles in the composite medium

4.2 Micromechanical Model for Thermo-mechanical Analyses of FRP Composites

The four-cell micromechanical (unit-cell) model derived previously in Chapter III is now extended for analyzing the overall thermo-mechanical responses of composites that include the effect of thermal stresses. This micromechanical model is also used to determine the effective coefficient of thermal expansion (CTE) of the unidirectional FRP composite, having nonlinear time-stress-temperature dependent properties of the constituents. The incremental micromechanical formulation is described in terms of the average strains and stresses in the subcells, as discussed in Chapter III.

For the linearized thermo-elastic constitutive relation, the effective stress and strain of the FRP composites are written as:

$$\Delta\bar{\sigma}_{ij} = \bar{C}_{ijkl}\Delta\bar{\varepsilon}_{kl} = \bar{C}_{ijkl}[\Delta\bar{\varepsilon}_{kl}^{M} - \Delta\bar{\varepsilon}_{kl}^{T}] = \bar{C}_{ijkl}[\Delta\bar{\varepsilon}_{kl}^{M} - \bar{\alpha}_{kl}(\bar{T} - \bar{T}_0)] \tag{4.11}$$

where $\bar{C}_{ijkl}$ are the effective elastic stiffness tensors and $\bar{\alpha}_{ij}$ are the effective CTE. The field variables $\bar{\varepsilon}_{ij}^{M}$ and $\bar{\varepsilon}_{ij}^{T}$ are the effective mechanical and thermal strains, respectively. The parameters $\bar{T}$ and $\bar{T}_0$ are the effective current and reference temperatures, respectively. The micromechanical model formulation is obtained in terms of the constitutive relations in each constituents and microstructural geometry, i.e. RVE. The linear thermo-elastic constitutive relations in each constituent or subcell (m) are related by the following relation:

$$\Delta\sigma_{ij}^{(m)} = C_{ijkl}^{(m)}\Delta\varepsilon_{kl}^{(m)} = C_{ijkl}[\Delta\varepsilon_{kl}^{(m)} - \Delta\varepsilon_{kl}^{(m)}] = C_{ijkl}[\Delta\varepsilon_{kl}^{(m)} - \alpha_{kl}^{(m)}(T - T_0)] \tag{4.12}$$

The average stresses and strains in the FRP composites are obtained through a volume averaging scheme, as discussed in Chapter III. This study considers thermo-viscoelastic (-viscoplastic) response of the polymeric matrix, which violates the linearized thermo-mechanical relations in Eqs. (4.11) and (4.12). In order to obtain solutions to thermo-viscoelastic (-viscoplastic) boundary value problems in FRP composites, an incremental formulation is considered. The linearized relation is first used to obtain trial solution at each time increment followed by iterative schemes to minimize errors from linearizing the nonlinear responses.

The incremental form of total stresses and mechanical and thermal strains are:

$$
\begin{aligned}
&\overline{\sigma}_{ij}^{t} = \overline{\sigma}_{ij}^{t-\Delta t} + \Delta\overline{\sigma}_{ij}^{t} \\
&\sigma_{ij}^{(m),t} = \sigma_{ij}^{(m),t-\Delta t} + \Delta\sigma_{ij}^{(m),t} \\
&\overline{\varepsilon}_{ij}^{M,t} = \overline{\varepsilon}_{ij}^{M,t-\Delta t} + \Delta\overline{\varepsilon}_{ij}^{M,t} \\
&\varepsilon_{ij}^{M(m),t} = \varepsilon_{ij}^{M(m),t-\Delta t} + \Delta\varepsilon_{ij}^{M(m),t} \\
&\overline{\varepsilon}_{ij}^{T,t} = \overline{\varepsilon}_{ij}^{T,t-\Delta t} + \Delta\overline{\varepsilon}_{ij}^{T,t} \\
&\varepsilon_{ij}^{T(m),t} = \varepsilon_{ij}^{T(m),t-\Delta t} + \Delta\varepsilon_{ij}^{T(m),t}
\end{aligned}
\tag{4.13}
$$

The superscript, $t - \Delta t$, denotes quantities at the previous converged time, and prefix, Δ, denotes an incremental quantity at the current time increment. The material parameters in the constitutive models for the fiber and matrix constituents are temperature dependent, thus it is necessary to quantify the current temperature or incremental temperature in each subcell. Since it is assumed that the RVE's length scale (micro-scale) is much smaller than the structural scale, in each unit-cell (material point of a composite) the steady state condition is reached in a relatively short period compared to the macroscopic conduction time. The transient heat transfer analysis within a unit-cell is

ignored and temperatures are assumed to vary at the material points. The current incremental temperature and total temperature in each subcell are evaluated as follows:

$$\Delta T^{t,(m)} = \Delta \overline{T}^{t} \tag{4.14}$$

$$T^{t,(m)} = T^{t-\Delta t,(m)} + \Delta T^{t,(m)} \tag{4.15}$$

The micromechanical model is designed to be compatible with displacement based FE structural analyses in which the effective mechanical strains ($\Delta \overline{\varepsilon}_{ij}^{M,t}$) are the independent variables. Hill (1965) proposed the average stresses and strains in each subcell can be expressed in terms of the effective stress and strain by defining a concentration tensor. In this study, a strain interaction tensor ($\mathbf{B}^{(m),t}$) that relates the effective incremental mechanical strain, $\Delta \overline{\varepsilon}_{kl}^{M,t}$, to the incremental average mechanical strains in each subcell, $\Delta \varepsilon_{ij}^{M,(m),t}$ is defined:

$$\Delta \varepsilon_{ij}^{M,(m),t} = \mathbf{B}_{ijkl}^{(m),t} \Delta \overline{\varepsilon}_{kl}^{M,t} \tag{4.16}$$

Using the linearized incremental strain in Eq. (10), the incremental stress in the subcell (m) is:

$$\Delta \sigma_{ij}^{(m),t} = C_{ijkl}^{(m),t} \mathbf{B}_{klpq}^{(m),t} \Delta \overline{\varepsilon}_{pq}^{M,t} \tag{4.17}$$

Substituting Eq. (11) into the incremental form of Eq. (5) gives the effective incremental stresses:

$$\Delta \overline{\sigma}_{ij}^{t} = \frac{1}{V} \sum_{m=1}^{N} V^{(m)} C_{ijkl}^{(m),t} \mathbf{B}_{klpq}^{(m),t} \Delta \overline{\varepsilon}_{pq}^{M,t} \tag{4.18}$$

The unit-cell effective tangent stiffness matrix $\overline{C}_{ijpq}^{t}$ is then defined by:

$$\overline{C}_{ijpq}^{t} = \frac{1}{V}\sum_{m=1}^{N} V^{(m)} C_{ijkl}^{(m),t} \mathbf{B}_{klpq}^{(m),t} \tag{4.19}$$

The fourth order tensor, $\mathbf{B}_{ijkl}^{(m),t}$, is derived by satisfying the micromechanical relations and the constitutive equations, as discussed in Chapter III. The homogenized incremental strain relations by satisfying the displacement compatibility along the longitudinal fiber direction (x_1) in the subcells are given as:

$$\begin{aligned} \Delta\overline{\varepsilon}_{ij}^{t} &= \Delta\overline{\varepsilon}_{ij}^{M,t} + \Delta\overline{\varepsilon}_{ij}^{T,t} = \Delta\varepsilon_{ij}^{M(1),t} + \Delta\varepsilon_{ij}^{T(1),t} = \Delta\varepsilon_{ij}^{M(2),t} + \Delta\varepsilon_{ij}^{T(2),t} \\ &= \Delta\varepsilon_{ij}^{M(3),t} + \Delta\varepsilon_{ij}^{T(3),t} = \Delta\varepsilon_{ij}^{M(4),t} + \Delta\varepsilon_{ij}^{T(4),t} \qquad , \quad i,j = 1 \end{aligned} \tag{4.20}$$

The homogenized incremental strain relations by satisfying the displacement compatibility for the transverse fiber directions (x_2) and (x_3) are given as:

$$\begin{aligned} \Delta\overline{\varepsilon}_{ij}^{(12),t} &= \Delta\overline{\varepsilon}_{ij}^{M,(12),t} + \Delta\overline{\varepsilon}_{ij}^{T,(12),t} = \frac{1}{V^{(1)}+V^{(2)}}[V^{(1)}\Delta\varepsilon_{ij}^{M(1),t} + V^{(2)}\Delta\varepsilon_{ij}^{M(2),t}] \\ &\quad + \frac{1}{V^{(1)}+V^{(2)}}[V^{(1)}\Delta\varepsilon_{ij}^{T(1),t} + V^{(2)}\Delta\varepsilon_{ij}^{T(2),t}] \end{aligned} \tag{4.21}$$

$$\begin{aligned} \Delta\overline{\varepsilon}_{ij}^{(34),t} &= \Delta\overline{\varepsilon}_{ij}^{M,(34),t} + \Delta\overline{\varepsilon}_{ij}^{T,(34),t} = \frac{1}{V^{(3)}+V^{(4)}}[V^{(3)}\Delta\varepsilon_{ij}^{M(3),t} + V^{(4)}\Delta\varepsilon_{ij}^{M(4),t}] \\ &\quad + \frac{1}{V^{(3)}+V^{(4)}}[V^{(3)}\Delta\varepsilon_{ij}^{T(3),t} + V^{(4)}\Delta\varepsilon_{ij}^{T(4),t}] \end{aligned} \tag{4.22}$$

$$, \quad i,j = 2$$

$$\Delta\overline{\varepsilon}_{ij}^{(13),t} = \Delta\overline{\varepsilon}_{ij}^{M,(13),t} + \Delta\overline{\varepsilon}_{ij}^{T,(13),t} = \frac{1}{V^{(1)}+V^{(3)}}[V^{(1)}\Delta\varepsilon_{ij}^{M(1),t} + V^{(3)}\Delta\varepsilon_{ij}^{M(3),t}]$$

$$+\frac{1}{V^{(1)}+V^{(3)}}[V^{(1)}\Delta\varepsilon_{ij}^{T(1),t}+V^{(3)}\Delta\varepsilon_{ij}^{T(3),t}] \tag{4.23}$$

$$\Delta\overline{\varepsilon}_{ij}^{(24),t}=\Delta\overline{\varepsilon}_{ij}^{M,(24),t}+\Delta\overline{\varepsilon}_{ij}^{T,(24),t}=\frac{1}{V^{(2)}+V^{(4)}}[V^{(2)}\Delta\varepsilon_{ij}^{M(2),t}+V^{(4)}\Delta\varepsilon_{ij}^{M(4),t}]$$

$$+\frac{1}{V^{(2)}+V^{(4)}}[V^{(2)}\Delta\varepsilon_{ij}^{T(2),t}+V^{(4)}\Delta\varepsilon_{ij}^{T(4),t}] \tag{4.24}$$

$$, \quad i,j=3$$

The homogenized incremental stresses by satisfying the traction continuity for loading along the fiber direction are expressed as:

$$\Delta\overline{\sigma}_{ij}^{t}=\sum_{m=1}^{4}V^{(m)}\Delta\sigma_{ij}^{(m),t} \qquad i,j=1;\ k,l=1,2,3 \tag{4.25}$$

$$\Delta\overline{\sigma}_{ij}^{t}=\overline{C}_{ijkl}^{t}\Delta\overline{\varepsilon}_{kl}^{t}=\overline{C}_{ijkl}^{t}\Delta\overline{\varepsilon}_{kl}^{M,t}-\overline{C}_{ijkl}^{t}\Delta\overline{\varepsilon}_{kl}^{T,t} \tag{4.26}$$

$$=\overline{C}_{ijkl}^{t}\Delta\overline{\varepsilon}_{kl}^{M,t}-\frac{1}{V}\sum_{m=1}^{4}V^{(m)}C_{ijkl}^{(m),t}\Delta\varepsilon_{kl}^{T(m),t}$$

$$=\overline{C}_{ijkl}^{t}\Delta\overline{\varepsilon}_{kl}^{M,t}-\frac{1}{V}\sum_{m=1}^{4}V^{(m)}C_{ijkl}^{(m),t}\alpha_{kl}^{(m),t}\Delta T$$

$$\Delta\overline{\sigma}_{ij}^{t}=\overline{C}_{ijkl}^{t}[\Delta\overline{\varepsilon}_{kl}^{t}-\overline{\alpha}_{kl}^{t}\Delta T] \tag{4.27}$$

$$\overline{C}_{ijkl}^{t}\overline{\alpha}_{kl}^{t}\Delta T=\frac{1}{V}\sum_{m=1}^{4}V^{(m)}C_{ijkl}^{(m),t}\alpha_{kl}^{(m),t}\Delta T \tag{4.28}$$

The effective consistent tangent CTE for fiber direction of orthotropic nonlinear response is then described as:

$$\bar{\alpha}_{ij}^{t} = \bar{\alpha}^{t}\delta_{ij} = \bar{C}_{ijkl}^{-1,t}\frac{1}{V}\sum_{m=1}^{4}V^{(m)}C_{ijkl}^{(m),t}\alpha_{kl}^{(m),t} \qquad i,j=1;\ k,l=1,2,3 \tag{4.29}$$

$$\bar{C}_{ijkl}^{t} = \bar{S}_{ijkl}^{-1,t} \tag{4.30}$$

$$\bar{S}_{ijkl}^{t} = \frac{1}{V}\sum_{m=1}^{4}V^{(m)}C_{ijkl}^{(m)-1,t} \tag{4.31}$$

The traction continuity along the transverse fiber direction (x_2) are expressed as:

$$\Delta\sigma_{ij}^{(1),t} = \Delta\sigma_{ij}^{(2),t} \qquad i,j=2;\ k,l=1,2,3 \tag{4.32}$$

$$\Delta\sigma_{ij}^{(3),t} = \Delta\sigma_{ij}^{(4),t} \tag{4.33}$$

$$\Delta\bar{\sigma}_{ij}^{t} = \bar{C}_{ijkl}^{t}\Delta\bar{\varepsilon}_{kl}^{t} = \bar{C}_{ijkl}^{t}\Delta\bar{\varepsilon}_{kl}^{M,t} - \bar{C}_{ijkl}^{t}\Delta\bar{\varepsilon}_{kl}^{T,t} \tag{4.34}$$

$$= \bar{C}_{ijkl}^{t}\Delta\bar{\varepsilon}_{kl}^{M,t} - \frac{1}{V}[V^{(12)}C_{ijkl}^{(12),t}\Delta\varepsilon_{kl}^{T(12),t} + V^{(34)}C_{ijkl}^{(34),t}\Delta\varepsilon_{kl}^{T(34),t}]$$

$$= \bar{C}_{ijkl}^{t}\Delta\bar{\varepsilon}_{kl}^{M,t} - \frac{1}{V}[V^{(12)}C_{ijkl}^{(12),t}\alpha_{kl}^{(12),t} + V^{(34)}C_{ijkl}^{(34),t}\alpha_{kl}^{(34),t}]\Delta T$$

$$\Delta\bar{\sigma}_{ij}^{t} = \bar{C}_{ijkl}^{t}[d\bar{\varepsilon}_{kl}^{t} - \bar{\alpha}_{kl}^{t}\Delta T] \tag{4.35}$$

$$\bar{C}_{ijkl}^{t}\bar{\alpha}_{kl}^{t}\Delta T = \frac{1}{V}[V^{(12)}C_{ijkl}^{(12),t}\alpha_{kl}^{(12),t} + V^{(34)}C_{ijkl}^{(34),t}\alpha_{kl}^{(34),t}]\Delta T \tag{4.36}$$

The effective consistent tangent CTE for transverse fiber direction of orthotropic nonlinear response is then described as:

$$\bar{\alpha}_{ij}^{t} = \bar{\alpha}^{t}\delta_{ij} = \bar{C}_{ijkl}^{-1,t}\frac{1}{V}[V^{(12)}C_{ijkl}^{(12),t}\alpha_{kl}^{(12),t} + V^{(34)}C_{ijkl}^{(34),t}\alpha_{kl}^{(34),t}] \tag{4.37}$$

$$V^{(12)} = V^{(1)} + V^{(2)}, \qquad V^{(34)} = V^{(3)} + V^{(4)}$$

$$\alpha_{ij}^{(12),t} = \frac{1}{V^{(12)}}[V^{(1)}\alpha_{ij}^{(1),t} + V^{(2)}\alpha_{ij}^{(2),t}], \qquad \alpha_{ij}^{(34),t} = \frac{1}{V^{(34)}}[V^{(3)}\alpha_{ij}^{(3),t} + V^{(4)}\alpha_{ij}^{(4),t}]$$

$$S_{ijkl}^{(12),t} = \frac{1}{V^{(12)}}[V^{(1)}C_{ijkl}^{(1)-1,t} + V^{(2)}C_{ijkl}^{(2)-1,t}], \qquad C_{ijkl}^{(12),t} = S_{ijkl}^{(12)-1,t}$$

$$S_{ijkl}^{(34),t} = \frac{1}{V^{(34)}}[V^{(3)}C_{ijkl}^{(3)-1,t} + V^{(4)}C_{ijkl}^{(4)-1,t}], \qquad C_{ijkl}^{(34),t} = S_{ijkl}^{(34)-1,t}$$

$$\overline{C}_{ijkl}^{t} = \frac{1}{V}[V^{(12)}C_{ijkl}^{(12),t} + V^{(34)}C_{ijkl}^{(34),t}]$$

The traction continuity for the transverse fiber direction (x_3) is:

$$\Delta\sigma_{ij}^{(1),t} = \Delta\sigma_{ij}^{(3),t} \qquad i, j = 3;\ k, l = 1, 2, 3 \tag{4.38}$$

$$\Delta\sigma_{ij}^{(2),t} = \Delta\sigma_{ij}^{(4),t} \tag{4.39}$$

$$\Delta\overline{\sigma}_{ij}^{t} = \overline{C}_{ijkl}^{t}\Delta\overline{\varepsilon}_{kl}^{t} = \overline{C}_{ijkl}^{t}d\overline{\varepsilon}_{kl}^{M,t} - \overline{C}_{ijkl}^{t}\Delta\overline{\varepsilon}_{kl}^{T,t} \tag{4.40}$$

$$= \overline{C}_{ijkl}^{t}\Delta\overline{\varepsilon}_{kl}^{M,t} - \frac{1}{V}[V^{(13)}C_{ijkl}^{(13),t}\Delta\varepsilon_{kl}^{T(13),t} + V^{(24)}C_{ijkl}^{(24),t}\Delta\varepsilon_{kl}^{T(24),t}]$$

$$= \overline{C}_{ijkl}^{t}\Delta\overline{\varepsilon}_{kl}^{M,t} - \frac{1}{V}[V^{(13)}C_{ijkl}^{(13),t}\alpha_{kl}^{(13),t} + V^{(24)}C_{ijkl}^{(24),t}\alpha_{kl}^{(24),t}]\Delta T$$

$$\Delta\overline{\sigma}_{ij}^{t} = \overline{C}_{ijkl}^{t}[\Delta\overline{\varepsilon}_{kl}^{t} - \overline{\alpha}_{kl}^{t}\Delta T] \tag{4.41}$$

$$\overline{C}_{ijkl}^{t}\overline{\alpha}_{kl}^{t}\Delta T = \frac{1}{V}[V^{(13)}C_{ijkl}^{(13),t}\alpha_{kl}^{(13),t} + V^{(24)}C_{ijkl}^{(24),t}\alpha_{kl}^{(13),t}]\Delta T \tag{4.42}$$

The effective consistent tangent CTE for transverse fiber direction of orthotropic nonlinear response is then described as:

$$\overline{\alpha}_{ij}^{t} = \overline{\alpha}^{t}\delta_{ij} = \overline{C}_{ijkl}^{-1,t}\frac{1}{V}[V^{(13)}C_{ijkl}^{(13),t}\alpha_{kl}^{(13),t} + V^{(24)}C_{ijkl}^{(24),t}\alpha_{kl}^{(24),t}] \tag{4.43}$$

$$V^{(13)} = V^{(1)} + V^{(3)}, \qquad V^{(24)} = V^{(2)} + V^{(4)}$$

$$\alpha_{ij}^{(13),t} = \frac{1}{V^{(13)}}[V^{(1)}\alpha_{ij}^{(1),t} + V^{(3)}\alpha_{ij}^{(3),t}], \qquad \alpha_{ij}^{(24),t} = \frac{1}{V^{(24)}}[V^{(2)}\alpha_{ij}^{(2),t} + V^{(4)}\alpha_{ij}^{(4),t}]$$

$$S_{ijkl}^{(13),t} = \frac{1}{V^{(13)}}[V^{(1)}C_{ijkl}^{(1)-1,t} + V^{(3)}C_{ijkl}^{(3)-1,t}], \qquad C_{ijkl}^{(13),t} = S_{ijkl}^{(13)-1,t}$$

$$S_{ijkl}^{(24),t} = \frac{1}{V^{(24)}}[V^{(2)}C_{ijkl}^{(2)-1,t} + V^{(4)}C_{ijkl}^{(4)-1,t}], \qquad C_{ijkl}^{(24),t} = S_{ijkl}^{(24)-1,t}$$

$$\overline{C}_{ijkl}^{t} = \frac{1}{V}[V^{(13)}C_{ijkl}^{(13),t} + V^{(24)}C_{ijkl}^{(24),t}]$$

4.3 Numerical Implementation and Verification

The coupled thermo-mechanical problem for unidirectional FRP composite is sequentially done in a 3D continuum element by using subroutines UMATHT, UMAT, and UEXPAN of ABAQUS FE code. It is assumed that the deformation in the FRP composite depends on the temperature field, but the heat conduction process is independent on the deformation, i.e., the effect of energy dissipation due to the viscous deformation is ignored and its contribution to the heat generation is assumed negligible as this study focuses on small deformation gradient problems. In this study, the transient heat transfer analysis is performed and subroutine UMATHT is used for determining the effective thermal properties. The outcome from the heat transfer analysis is the time varying temperature profiles, sampled at nodes. These temperature profiles with or without external mechanical stimulus will be used as inputs to analyze the deformation in the FRP composite structures. The user subroutine UMAT and UEXPAN are used to

incorporate the nonlinear material parameters related to the deformation in FRP composites.

4.3.1 Effective CTE of glass fiber/epoxy composite

In order to validate the effective CTE obtained from the UC model, available analytical solutions, experimental data for glass/epoxy composites, and the micromechanical model with detailed microstructures are used. Figure 4.5 illustrates an example of FE meshes of an FRP microstructure with detailed fiber arrangements, for a composite with nearly 20% fiber volume content. The red color indicates the fibers and the blue color is for the matrix medium. The size of the FRP microstructure is $1\times1\times1\ \text{mm}^3$. The diameter of fibers for all FRP composites with different fiber volume contents is kept constant. The overall CTEs for FRP composites with different fiber volume contents at room temperature are first determined. The linear elastic and CTE properties of the E-glass fiber and epoxy at room temperature are shown in Table 4.4. These values are obtained from the date available in Karadeniz and Kumlutas (2007).

Table 4.4 Mechanical and thermal properties

Material	E [GPa]	G [GPa]	v	α [10^{-6}/K]
Glass fiber	72	40	0.2	5
Epoxy	3.5	3.89	0.35	52.5

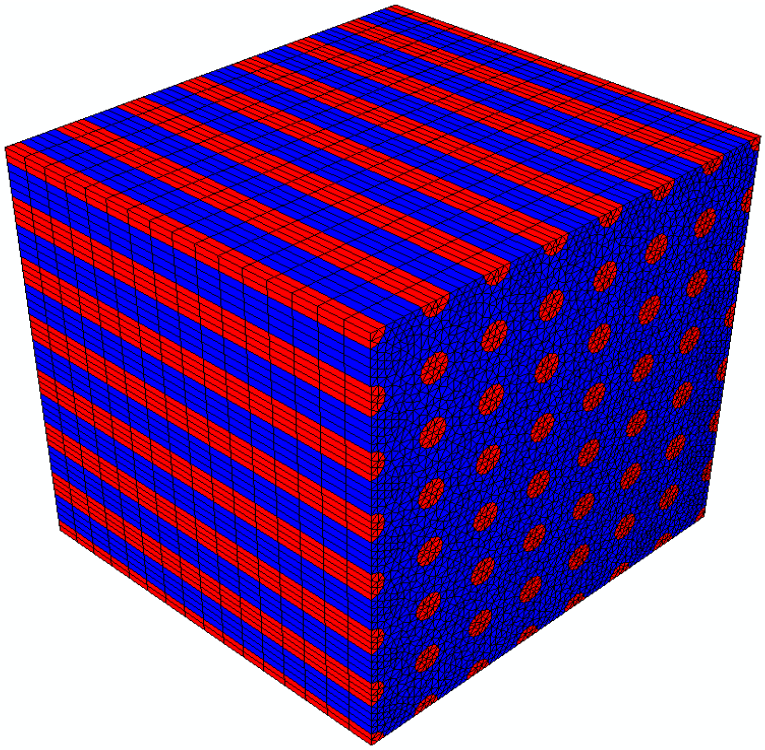

Figure 4.5 Detailed FE model for coupled mechanical and thermal analysis (V_f = 19.6%)

Figures 4.6 and 4.7 illustrate the effective CTEs of unidirectional FRP composites along the fiber and transverse to the fiber directions, respectively. The results obtained from the UC model are in a reasonably good agreement with available experimental data and analytical micromechanical models, especially for the overall CTEs along the fiber direction. Some mismatches with the experimental data are observed for the overall CTEs in the transverse fiber directions, especially for composites with low fiber volume contents. The reason of these mismatches could be due to the variation of the thermal stresses, i.e., localized thermal stresses are shown near the interface between fibers and matrix, while the UC model is limited in capturing such

variations. It is also seen in Figure 4.7 that the UC model shows similar results as other analytical models, except for the Schapery's model (Schapery, 1968), which is shown to be in a good agreement with the experimental data, and micromechanical models with detailed fiber arrangements. The effective CTEs of a unidirectional FRP composite from the Schapery's model are: $\alpha_1 = \frac{\overline{E\alpha}}{\overline{E}} = \frac{E_f \alpha_f V_f + E_m \alpha_m V_m}{E_f V_f + E_m V_m}$ for the axial fiber direction and $\alpha_2 = (1+\nu_f)\alpha_f V_f + (1+\nu_m)\alpha_m V_m - \alpha_1(\nu_f V_f + \nu_m V_m)$ for the transverse fiber direction.

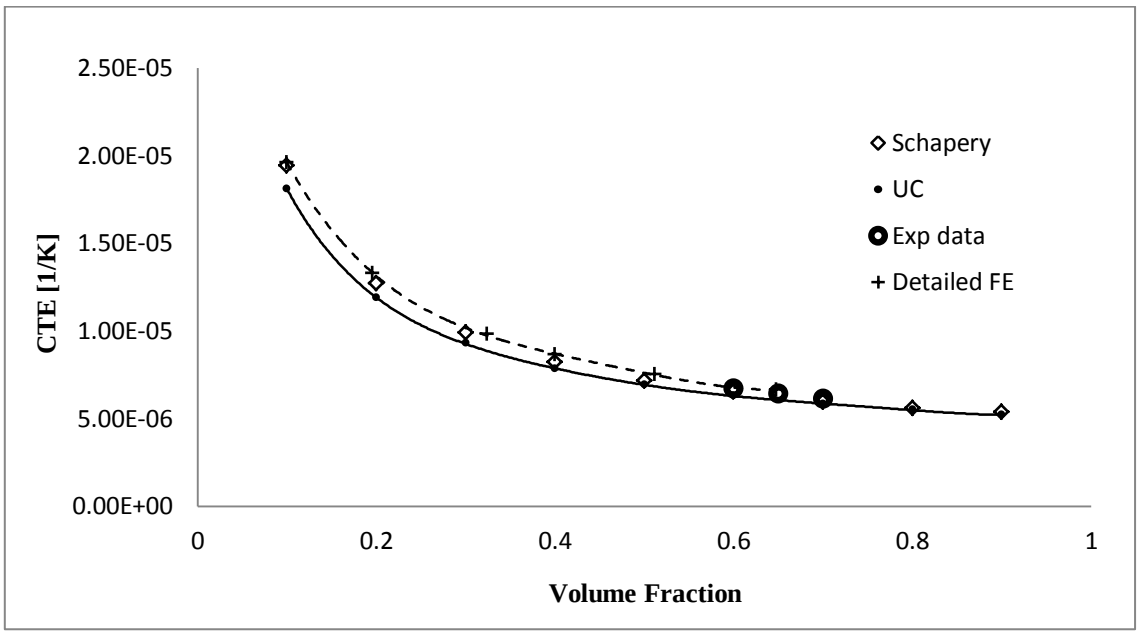

Figure 4.6 CTE of glass fiber/epoxy composite of axial fiber direction for different volume fractions

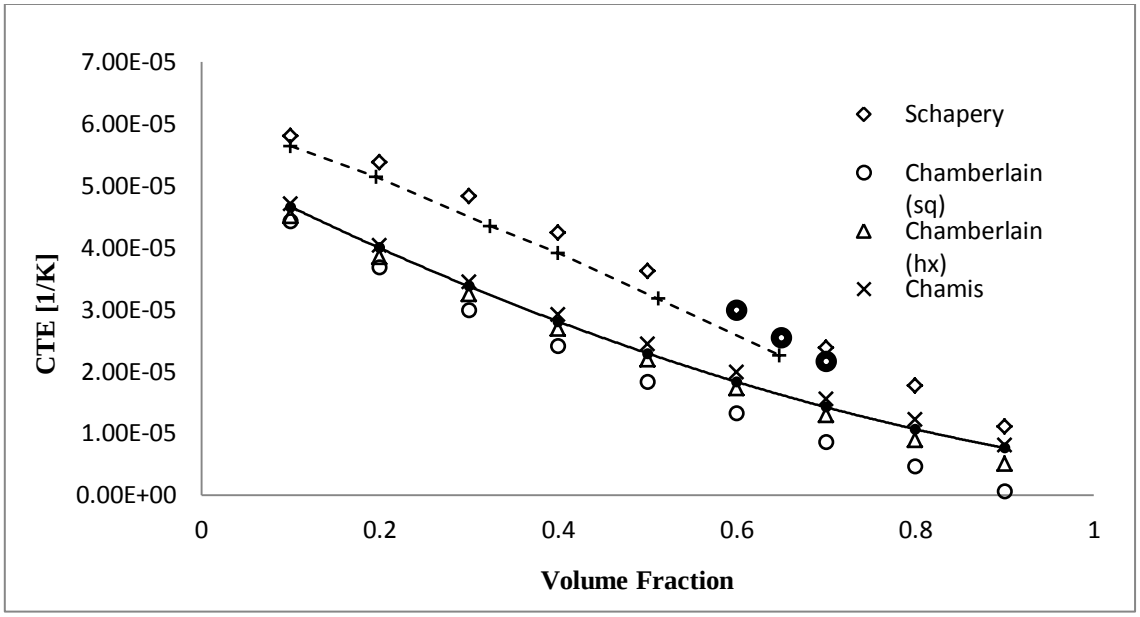

Figure 4.7 CTE of glass fiber/epoxy composite of transverse fiber direction for different volume fractions

4.3.2 Sequentially coupled thermo-mechanical analysis

The effect of temperature changes due to heat conduction on the deformation of viscoelastic-viscoplastic FRP composites is studied using the UC model and micromechanical models with microstructural details. Transient heat conduction analysis is first conducted and the temperature profiles at each instant of time are used as input variables in the deformation analysis of FRP composites. The size of the FRP samples is $1\times1\times1\ \text{mm}^3$; the small size is considered in order to accelerate the heat conduction analyses. The FRP composite is initially at room temperature (293K) and elevated temperature 393K is prescribed on the surfaces of the FRP composite. The initial and boundary conditions of the heat conduction analysis are presented in Figure 4.1. The

FRP composites are made of E-glass fiber and epoxy matrix. The physical and thermal properties for the fiber and matrix are given in Tables 4.1, 4.2, and the mechanical properties and CTE is given in Table 4.4. The viscoelastic-viscoplastic properties of epoxy matrix which are calibrated from experimental data in Chapter III are used for the time-dependent response.

Heat conduction along the axial fiber direction is considered. Table 4.5 summarizes the steady state times for FRP composites at different fiber contents determined from the UC model and micromechanical models with detailed fiber arrangements. The steady state is reached in relatively short time compared to the results in Table 4.3, which is due to the small size FRP samples. The corresponding temperature profiles at several times for FRP composites with different fiber volume contents are illustrated in Figure 4.8. As expected higher fiber volume contents accelerate the heat conduction.

Table 4.5 Steady state time of axial heat conduction for UC model and detailed FE model

V_f [%]		10	19.6	32.4	51.2	64.8
Steady State Time [s]	UC Model	18.2	15.4	13.0	11.0	10.0
	Detailed FE Model	19.2	16	13.4	11.4	10.4
% Difference		5.2	3.8	3.0	3.5	3.8

Next, the micromechanical models are used to determine the deformation in the viscoelastic FRP composites due to the conduction of heat. The thermal stresses, which are mainly due to the mismatches in the CTEs of the fibers and matrix at the steady state condition, are examined for FRP composites with different fiber volume contents. It is noted that the thermal stresses vary with time during the transient heat conduction. Since the steady state time is reached in a relatively short period, the effect of viscoelastic matrix due to the thermal stresses is rather insignificant. Figures 4.9 and 4.10 illustrate the axial and transverse thermal stresses at steady state. The responses are shown for FRP composites with different fiber volume contents determined from the micromechanical models with detailed fiber arrangements. It is seen that non-uniform and discontinuities in the thermal stress fields are observed. For comparisons, the thermal stress profiles obtained from the simplified UC models are also presented for the FRP composite with 51.2% fiber volume content, which show a uniform temperature profile. This is because the UC model treats the composites as homogenized media. As seen from the thermal stress profiles, higher magnitude of stresses are experienced by the stiffer fibers, which is expected. The thermal stresses in the matrix are generally small, although some higher values are observed close to the interface between fibers and matrix. High stresses in the matrix could lead to plastic (viscoplastic) deformation.

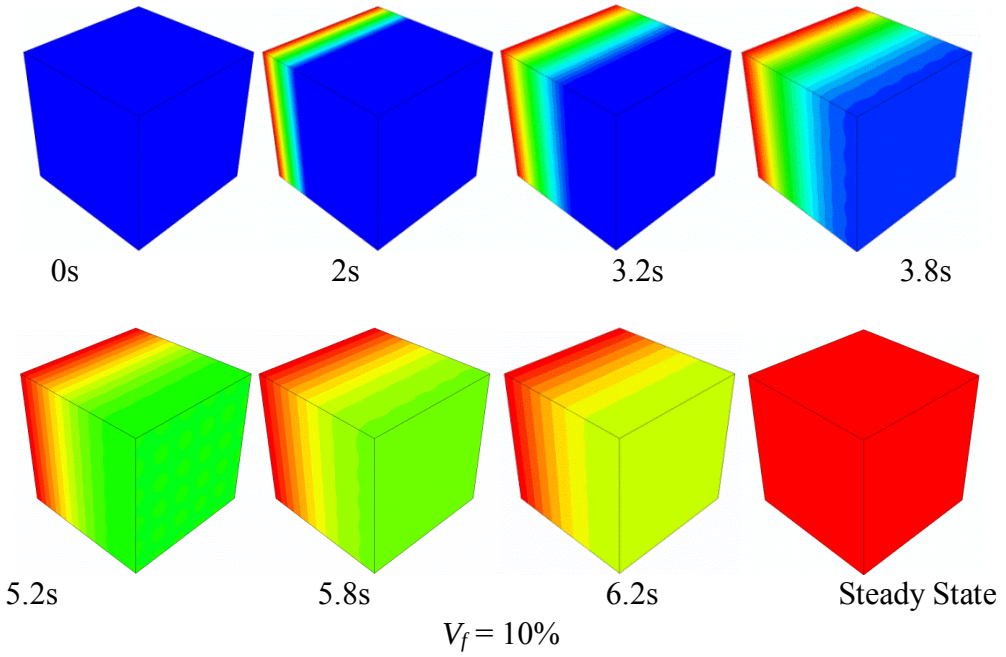

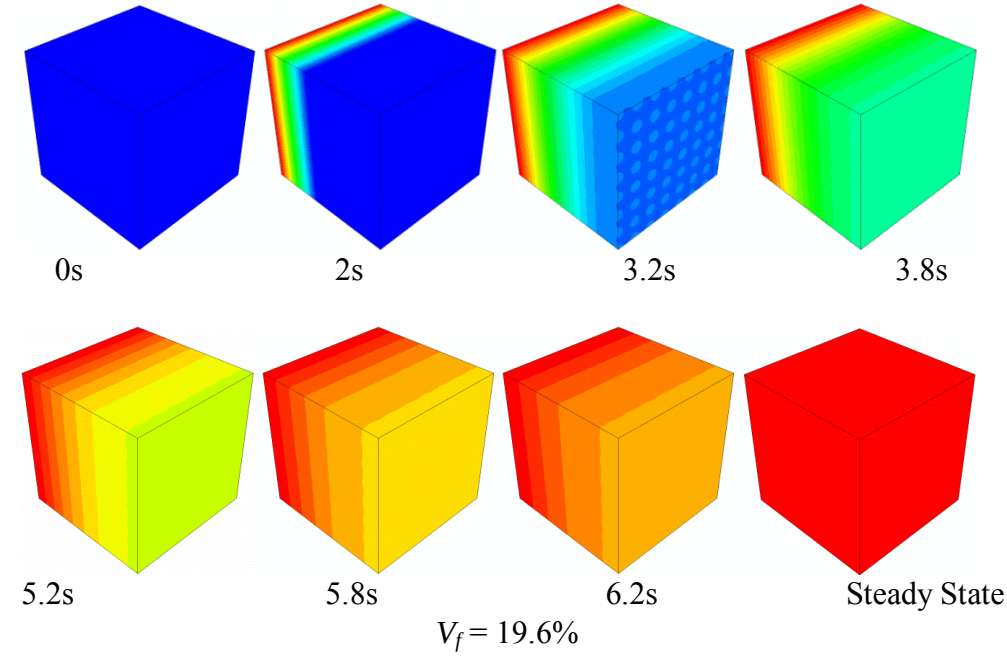

Figure 4.8 Temperature contours for axial direction during heat conduction

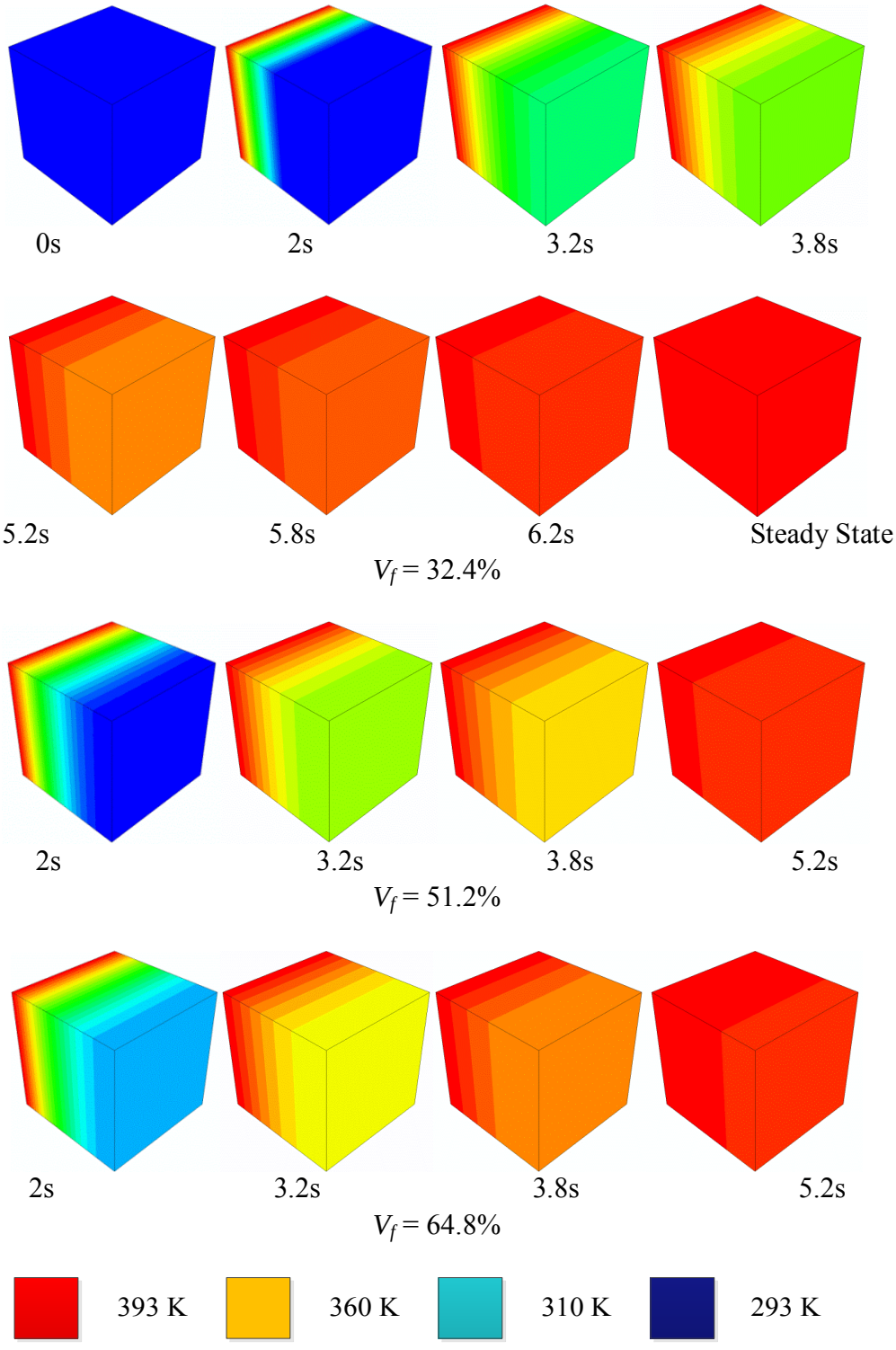

Figure 4.8 Continued

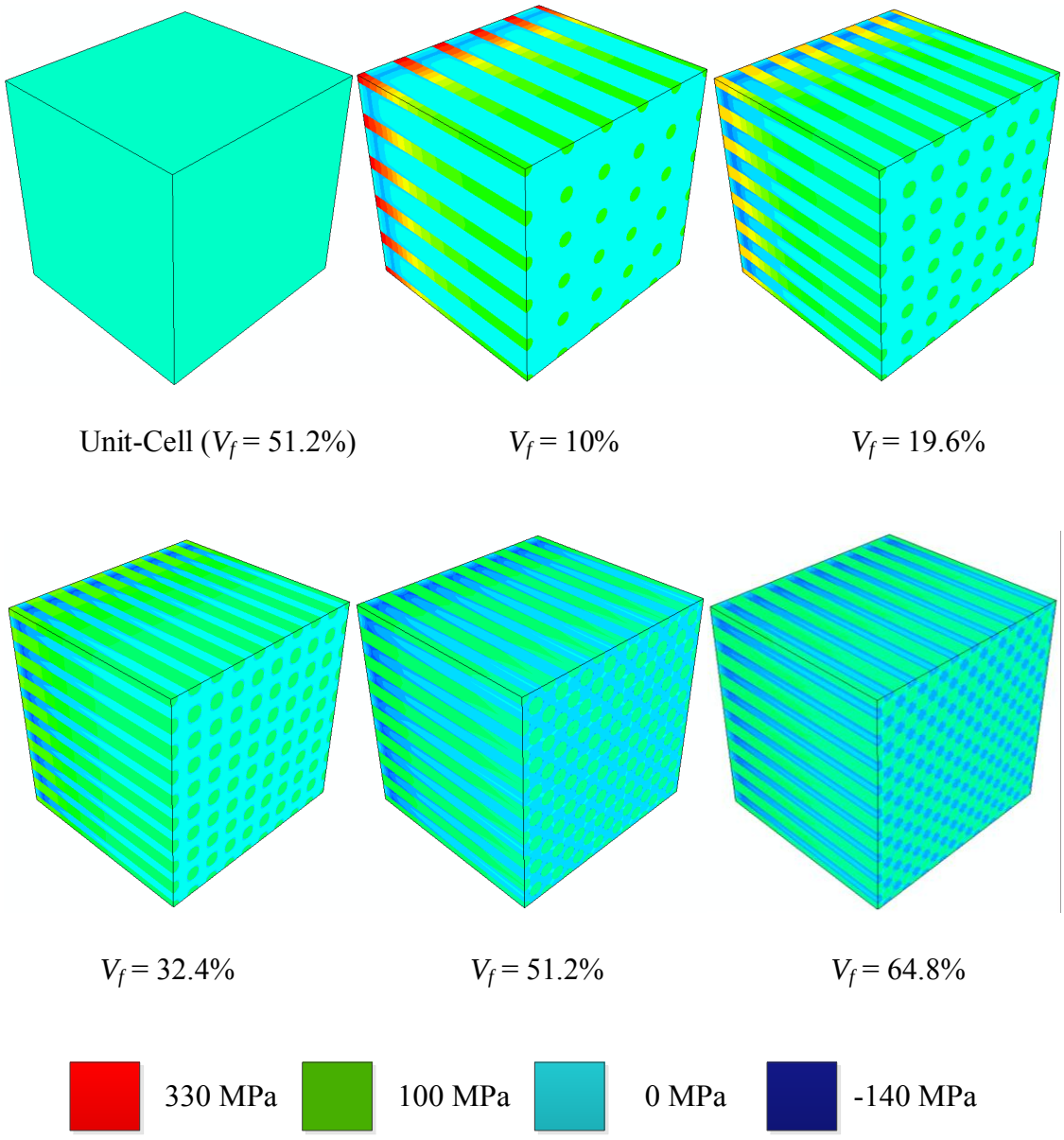

Figure 4.9 Thermal stresses in the axial fiber direction (σ_{11}) at steady state conditions

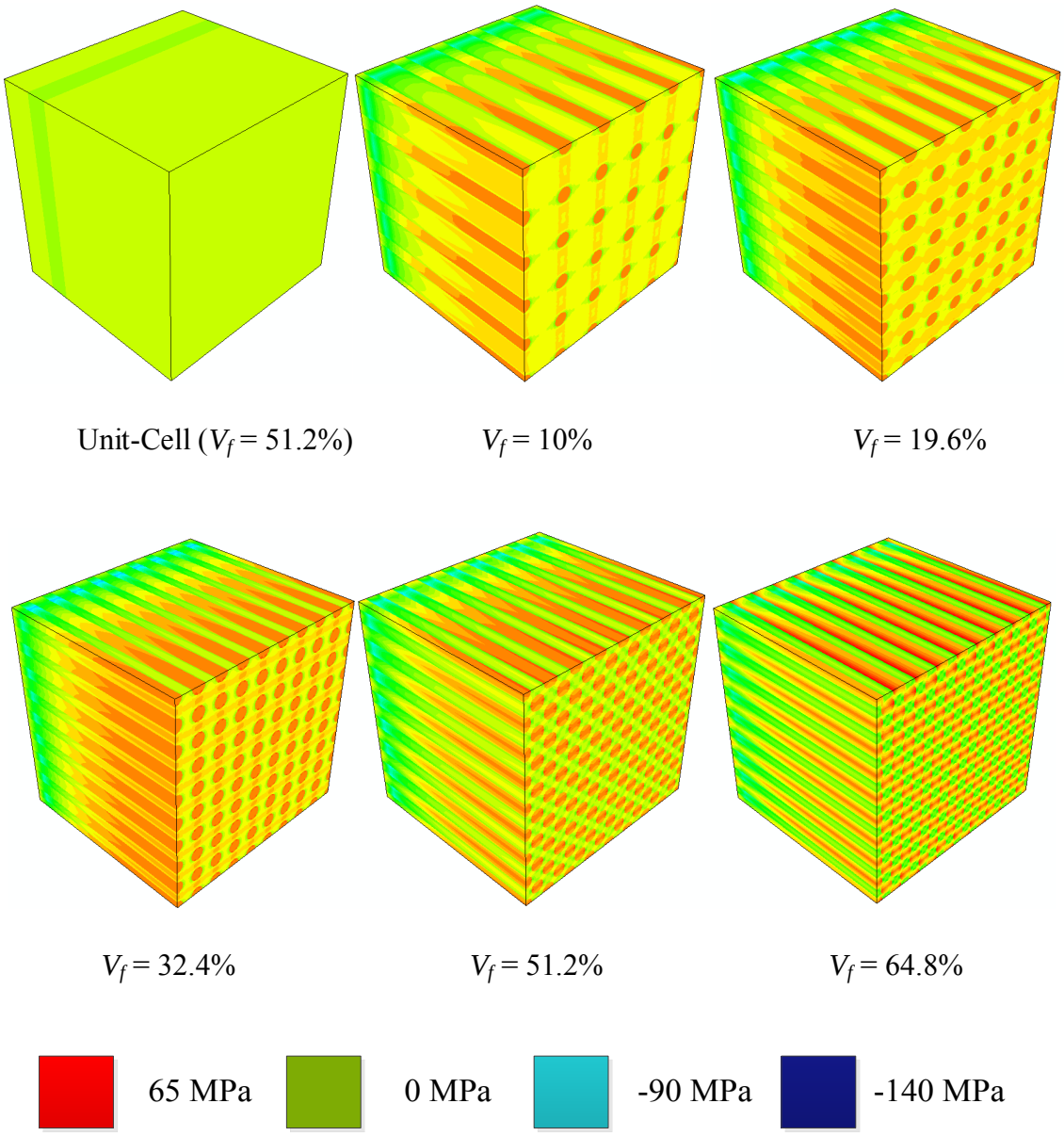

Figure 4.10 Thermal stresses in the transverse fiber direction (σ_{22}) at steady state conditions

In order to study the effect of coupled thermo-mechanical loading, FRP composite with 64.8% fiber volume content is now subjected to a mechanical stress once it reaches steady state temperature 393K. The steady state time of the FRP composite 64.8% fiber volume content is around 10 seconds, as shown in Table 4.5. The external loading is applied on the FRP along the transverse fiber direction with stress 10MPa. The creep-recovery of VE-VP response is performed for 3600 seconds, and the external stress is unloaded at 1800 seconds while temperature still remains at 393K for the remaining period. The corresponding stress contours of detailed micromechanical model and UC model are shown in Figure 4.11. For the detailed micromechanical model, the largest value of the von Mises stress is around 33-43MPa in the small region which is slightly beyond the yield stress of the matrix, 27.876MPa. Thus, there might be some effects of plastic deformations on the overall response of the composite. On the other hand, the UC model, which cannot capture the localized stress concentration effect, shows the stress contours close to the prescribed mechanical stresses with small variations due to the thermal stress effects. In order to examine the effect of the thermal and mechanical inputs in the UC model, thermal and mechanical boundary conditions are prescribed separately and stress fields in the UC model due to thermal and mechanical boundary conditions are monitored for 1800 seconds due to the possible stress relaxation effect from the viscoelastic(-plastic) matrix. The stress variation in the UC model is shown due to thermal expansion effect during the transient heat conduction while the UC model subjected to pure mechanical loading remains at a constant 10MPa, as depicted in Figures 4.12 and 4.13. After the heat conduction reaches steady state, after

10 seconds, the thermal stress varies with time, although the variation is relatively small, which is due to the viscoelastic matrix. This explains the variation in the stress contours from the coupled thermo-mechanical boundary conditions in Figure 4.11. Figures 4.14 and 4.15 present the creep-recovery curve for detailed micromechanical model and UC model of FRP composites with 64.8% fiber volume content, which highlight the effect of VE and VP deformations. The strains in Figures 4.14(a) and 4.15(a) are due to the thermo-mechanical effect, along the loading and transverse to the loading directions, respectively. For detailed micromechanical model, higher strains are due to the thermal expansion and some plastic deformations. The VP deformation shows 0.38% higher value than VE deformation at 3600 seconds. For the comparison of the creep-recovery responses in the two models, the creep-recovery strains of the transverse fiber direction shows a significant discrepancy during thermo-mechanical loading. In the recovery state, thermal strain remains due to thermal expansion and the percent difference between two models are similar to the difference in the creep strains of the two models. It is seen that this discrepancy is due to the CTE difference of the transverse fiber direction as shown in Figure 4.7. The corresponding creep-recovery strain in the axial fiber direction presents small percent difference since the CTEs in the axial fiber direction of the two models are in good agreement, as shown in Figure 4.6. The percent difference of the creep strains is shown in Table 4.6.

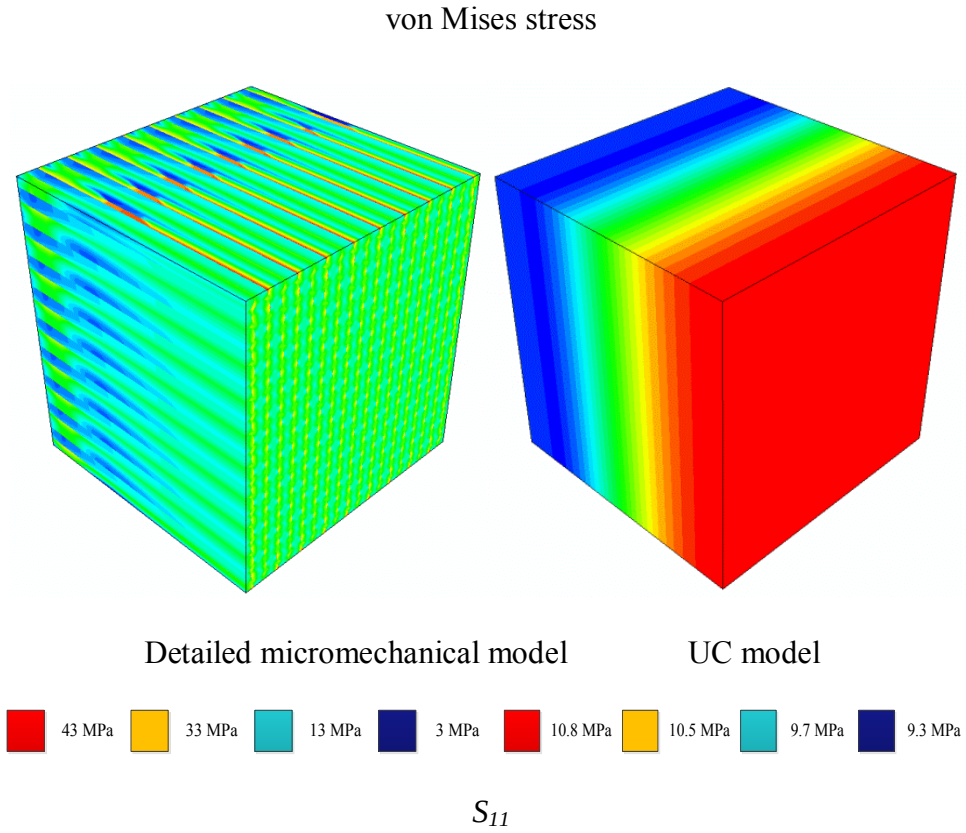

Figure 4.11 Stress contours of FRP composites in creep-recovery response with 64.8% fiber volume content under mechanical loading at 1800 seconds. The matrix in the detailed micromechanical model is assumed undergoing viscoelastic and viscoplastic deformation.

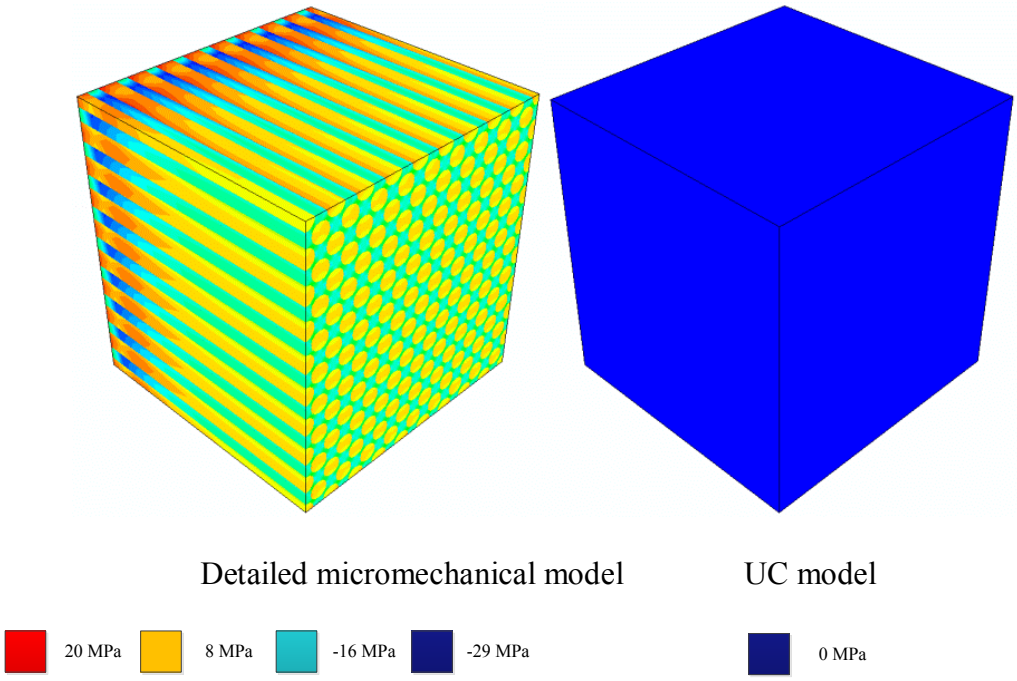

Figure 4.11 Continued

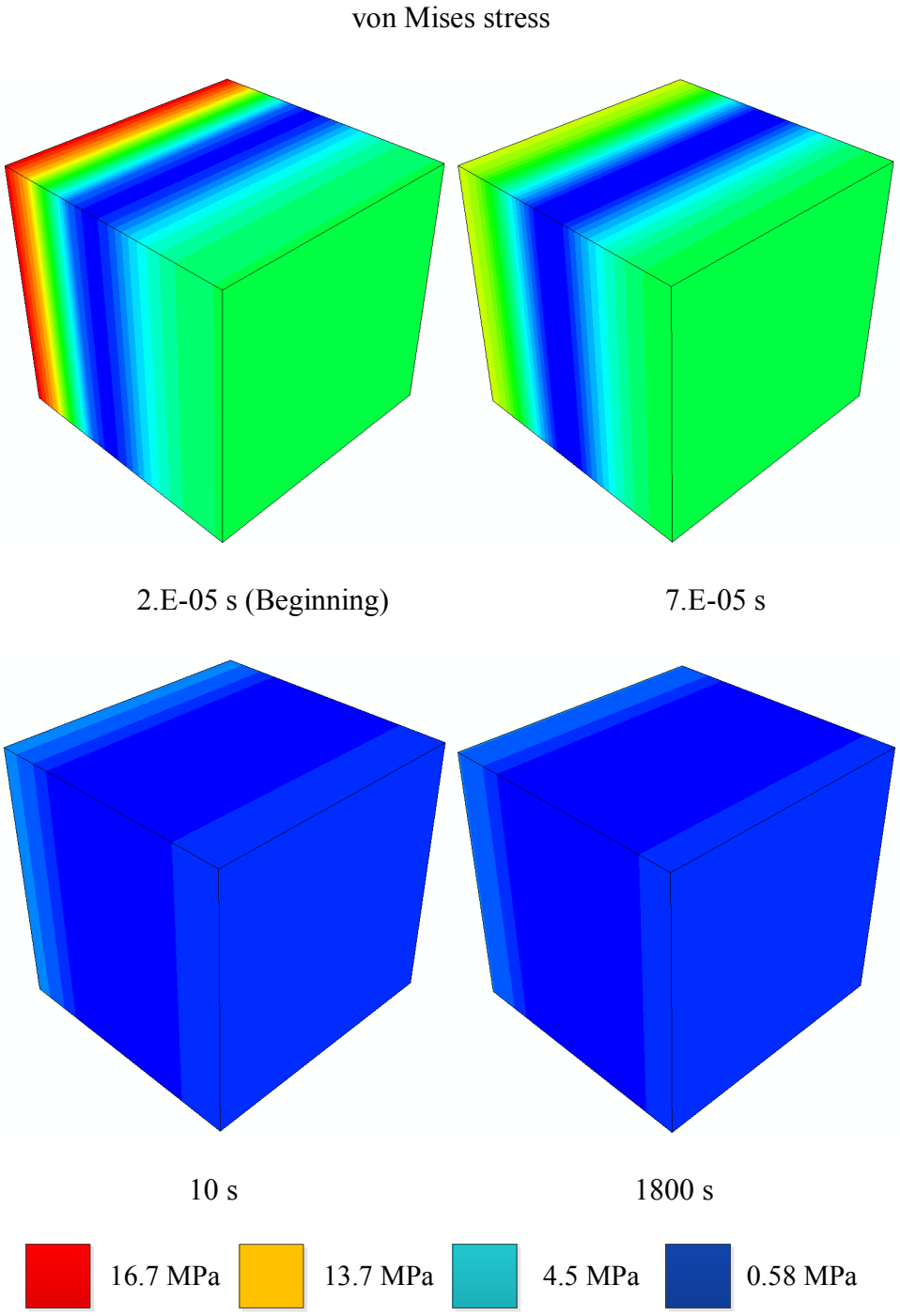

Figure 4.12 Stress contours of UC model with 64.8% fiber volume content under thermal boundary condition (during and after heat conduction).

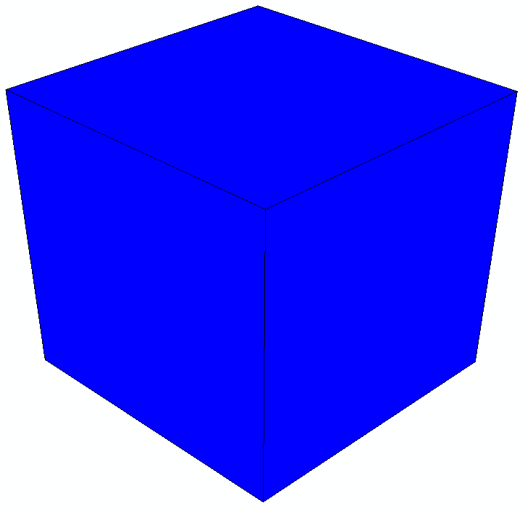

Constant during 1800s

10 MPa

Figure 4.13 Stress contours of UC model in creep-recovery response with 64.8% fiber volume content under mechanical loading only.

Table 4.6 Percent difference of viscoelastic creep strain for detail FE model and UC model

	VE creep strain of transverse direction at 1800 s				VE creep strain of axial fiber direction at 1800 s	
	Expansion + Mechanical loading		Only Expansion		Expansion + Mechanical loading	
Strain	ε_{22}	ε_{11}	ε_{22}	ε_{11}	ε_{11}	ε_{22}
detailed FE model	3.83E-03	5.69E-04	2.32E-03	6.22E-04	7.08E-04	1.69E-03
UC model	2.71E-03	5.60E-04	1.60E-03	6.12E-04	7.01E-04	1.24E-03
% difference	29.3	1.5	31	1.6	1.0	26.8

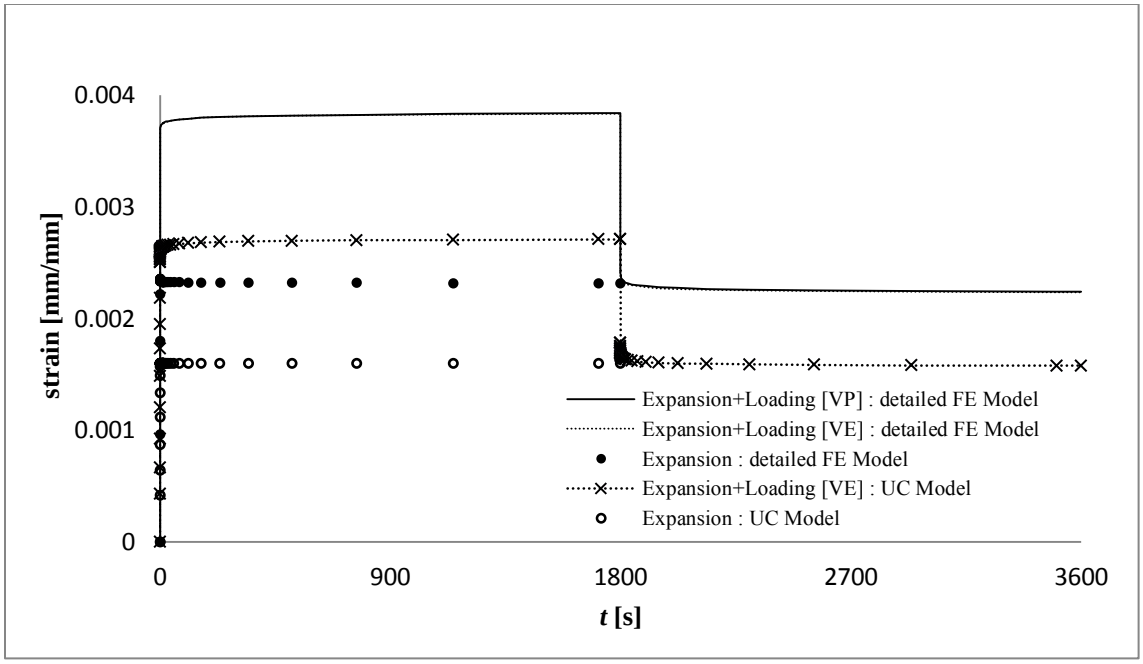

(a)

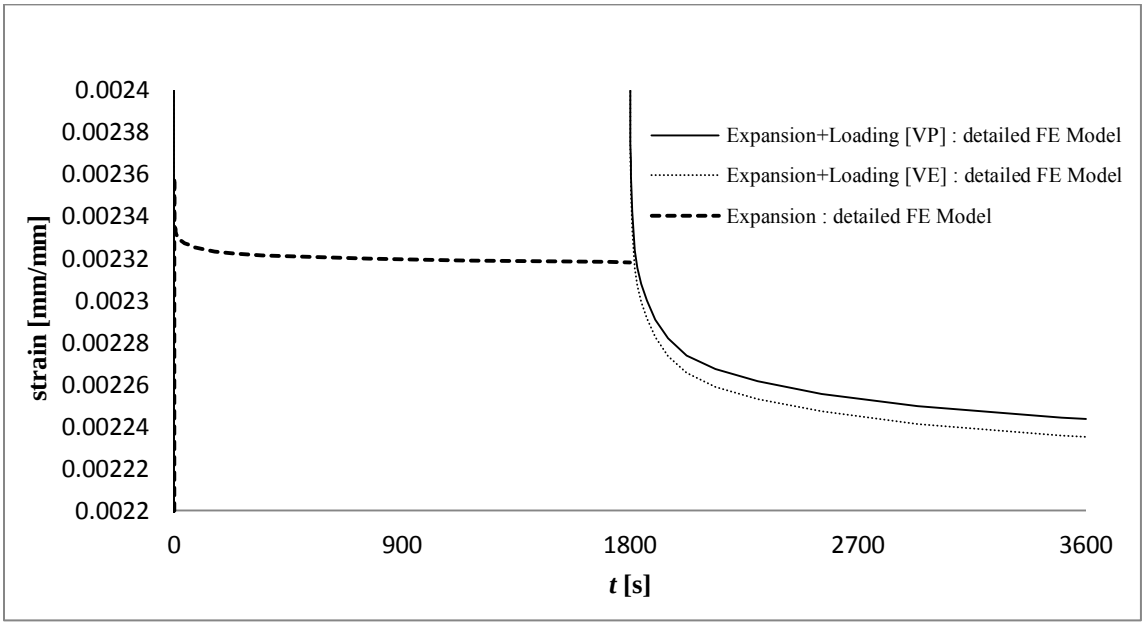

(b)

Figure 4.14 Creep-Recovery for thermal expansion and transverse loading (transverse direction)

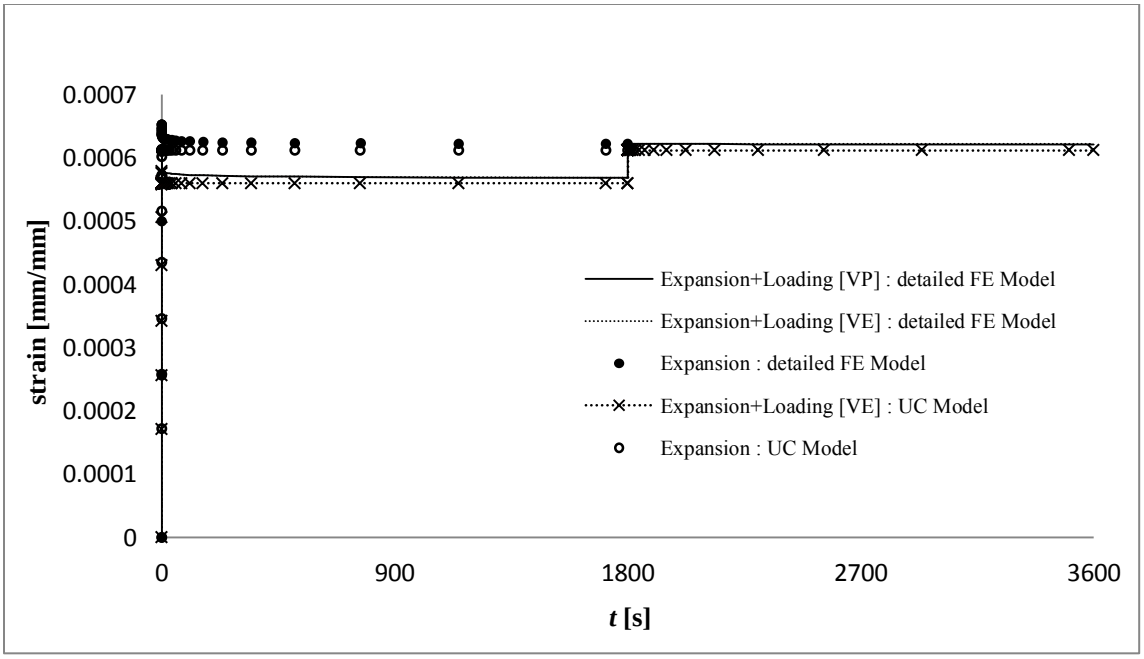

(a)

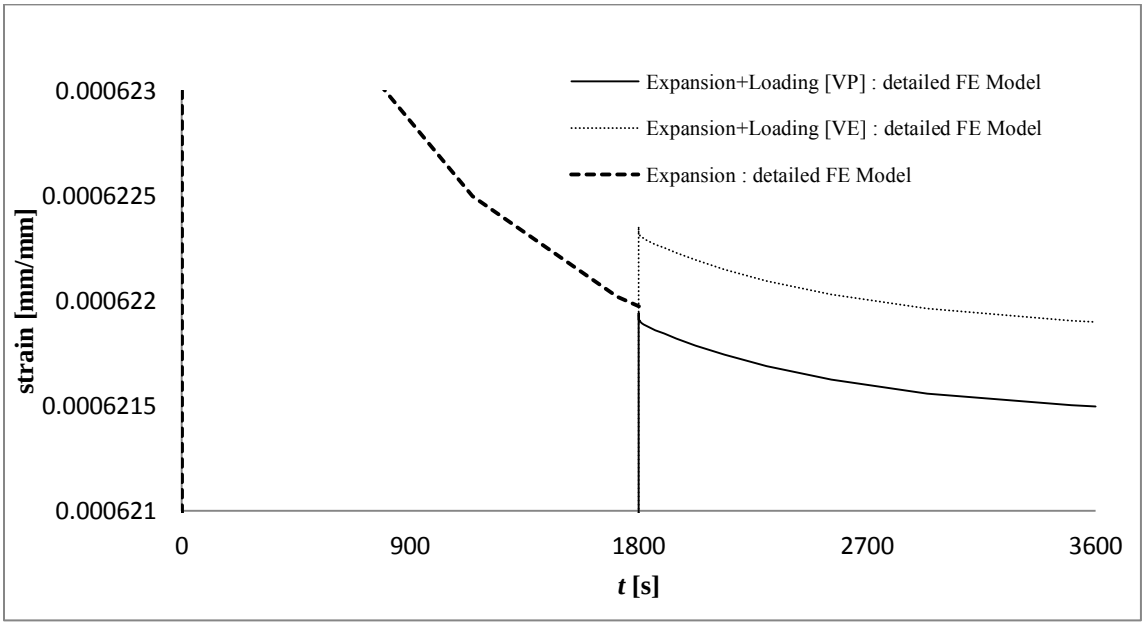

(b)

Figure 4.15 Corresponding creep-recovery response for thermal expansion and transverse loading

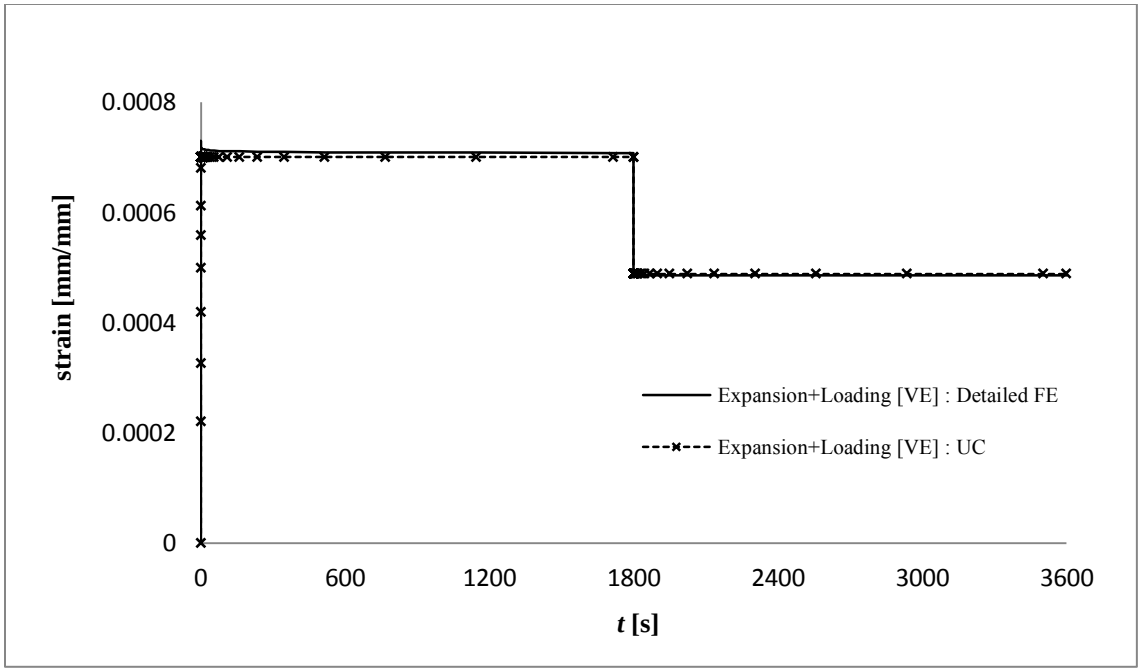

(a)

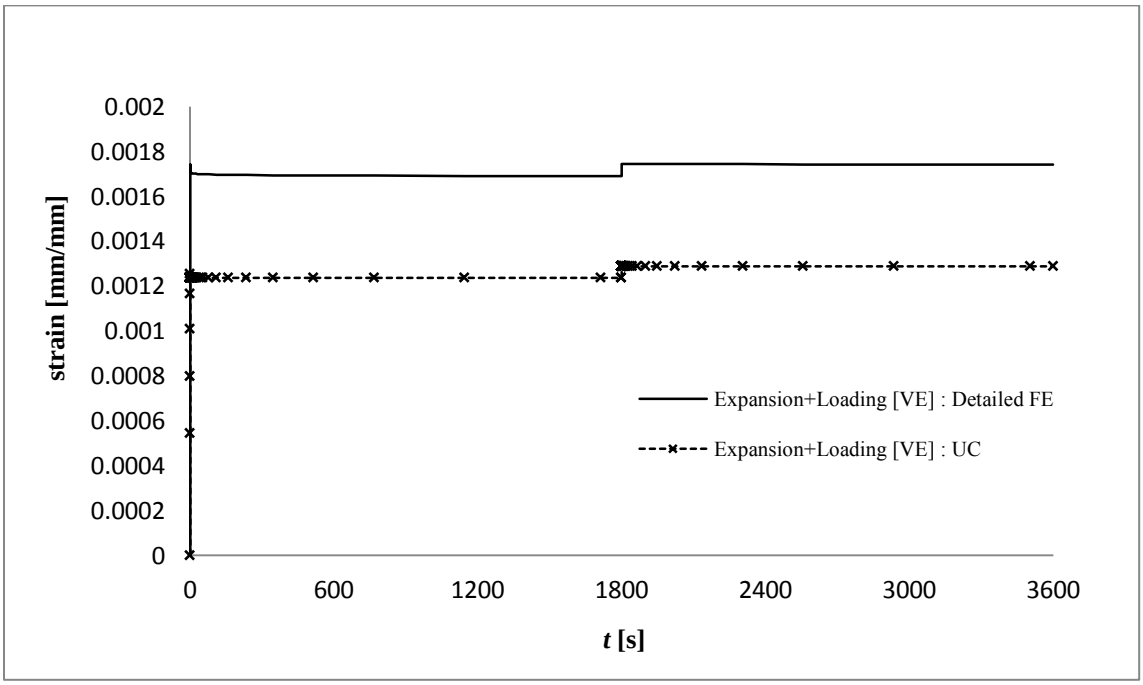

(b)

Figure 4.16 Creep-Recovery for thermal expansion and axial loading (fiber direction)

CHAPTER V

THERMO-MECHANICAL STRUCTURAL ANALYSIS OF SANDWICH COMPOSITES

The proposed UC models for heat conduction and deformation analyses of viscoelastic-viscoplastic FRP composites are implemented in FE and used for analyzing and designing FRP structural components. This chapter presents time-dependent analyses of polymeric sandwich composite beams due to transient heat conduction and mechanical loading as examples of structural analyses. The studied sandwich composites comprise of FRP skins and polymeric foam core. Lead Zirconia Titanate (PZT) sensors are also integrated within the FRP skins, which are usually used for monitoring life performance of the polymeric sandwich constructions. The ability to monitoring life performance of sandwich structures and each constituent in the sandwich composite can avoid catastrophic failures in sandwich structures and leads to more reliable sandwich constructions. Prior to designing smart sandwich composites, it is necessary to understand the performance of these composites under various boundary conditions, such as coupled mechanical and thermal effects. Since composites involve different constituents and various microstructural geometries, it is then important to quantify variations in field variables in the composites such as stress discontinuities or stress concentrations at the interfaces of different constituents in order to detect possible debonding/delamination.

Sandwich composites have been used in load-bearing components in buildings, spacecraft, aircraft, wind blades and naval structures. Some applications of sandwich composites are shown in Figure 5.1. The multilayered FRP laminated composite skins, which consist of strong and stiff fibers, and the low density thick foam core provide a relatively strong, stiff, and lightweight structural component. The polymer matrix in the FRP skins and foam core can experience pronounced time-dependent (viscoelastic or combined viscoelastic and viscoplastic) response when subjected to mechanical loadings. Hostile environmental conditions such as extreme temperature changes, humid environment, and UV exposure can significantly change the properties of the constituents in the sandwich composites. For example rates of creep deformations in polymers increase at elevated temperatures. On the other hand, the stiff fibers in the FRP skins and PZT components generally exhibit linear elastic behavior within working temperatures of polymeric sandwich composites.

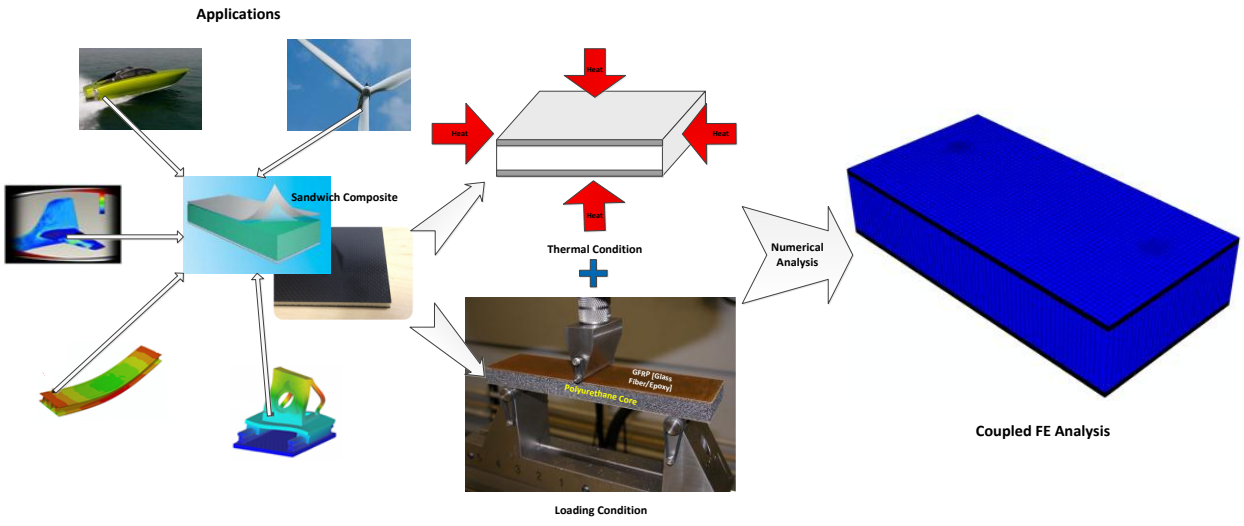

Figure 5.1 Applications of sandwich composites and analysis methods

Despite many advantages of using polymeric sandwich composites, one of the common failures in sandwich composites is delamination between skins and foam core and also within layers in the laminated skins. This delamination is due to stress discontinuities (or stress concentrations) at the interfaces/interphases of dissimilar materials. In addition, there might be non-negligible stress concentrations at the interfaces between the PZT and FRP layers. Thus, it is necessary to monitor time-dependent changes in the field variables (stress, strains, and displacements) in the sandwich composites under various loading histories. This can be achieved through the use of time-dependent multi-scale analyses.

5.1 Smart Sandwich Composites with PZT Wafers

This chapter analyzes time-dependent response of a sandwich composite beam under three-point bending at elevated temperatures, as an example of structural analysis. The schematic representation of smart sandwich composite structures is shown in Figure 5.2. The smart sandwich composites consist of different constituents: multilayered glass fiber reinforced polymer (GFRP) skin, polyurethane foam core, and lead zirconate titanate (PZT) wafers that are placed within the bottom layers of the GFRP skin. The PZT wafer is used to monitor life performance of sandwich structures. Detailed information on this sandwich composite can be found in Kim et al. (2011). The constitutive models of each constituent of the sandwich composites are shown in Figure 5.2. The polymeric matrix and foam core are considered as viscoelastic materials, and the glass fiber and PZT wafers are treated as linear elastic materials. The simplified UC

models, discussed in Chapter III and IV, are used for obtaining the effective time-dependent response of the GFRP skins. The multi-scale model is incorporated with ABAQUS FE code. The heat conduction throughout the composite body due to heating to testing temperature 80^{o}C (353K) is analyzed first and the temperature profiles obtained from the heat transfer analysis are used to study the effects of thermal stresses and prescribed mechanical loadings on the overall performance of sandwich structures.

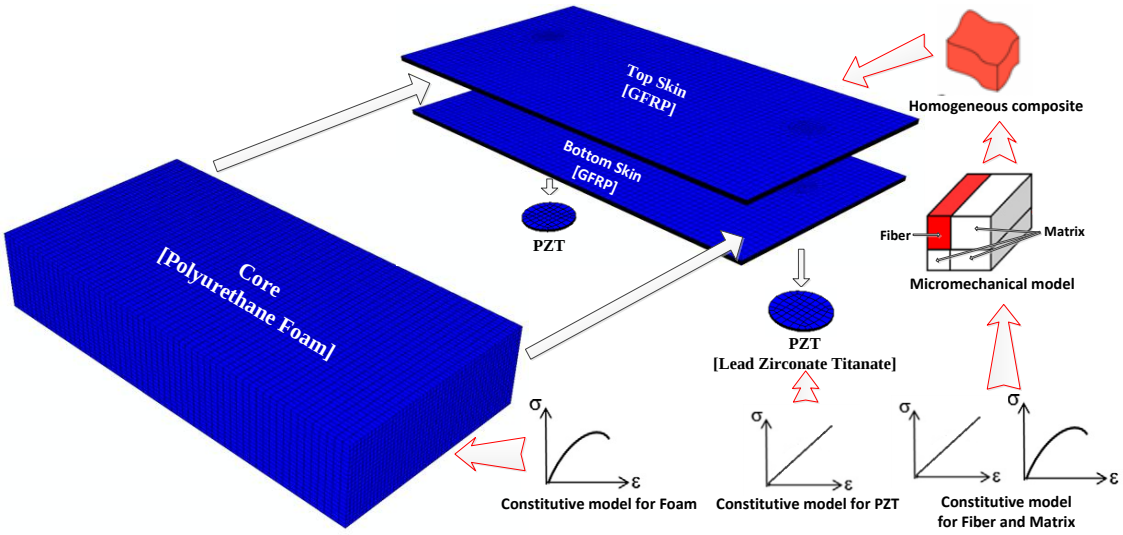

Figure 5.2 A multi-scale frameworks of smart sandwich composite

5.2 Computational Modeling for Smart Sandwich Composites

The dimensions of the sandwich composites are shown in Figure 5.3. Total 168200 elements are generated in the sandwich beams, which are C3D8 continuum elements. The components of sandwich composites are: (a) polyurethane foam core with

thickness 19.05 mm and density 4.1 kg/m^3; (b) unidirectional E-glass and epoxy resin with thickness of 1.524mm, consisting of 8 layers $[90°/0°]_8$ in total for each top and bottom layers; and (c) two PZT wafers with 7 mm diameters and 0.254 mm thickness. The two PZT wafers are inserted in the lay-ups between the 4^{th} and the 5^{th} layers of the bottom skin, which experiences tension under the three-point bending load. The top and bottom E-glass/epoxy skins in the sandwich composites consist of eight layers of each E-glass/epoxy composites. Each ply consists of the weaving fiber yarns perpendicular to the unidirectional fiber layers with relatively low reinforcements in the transverse fiber direction (Kim et al., 2011). In this study, the effective properties of each ply are modeled by assuming a stack of $[90°/0°]$ fiber layup with the different thickness of each fiber direction, which follows the actual thickness of the fiber yarns, and different fiber volume fractions are considered for the $0°$ and $90°$ fiber directions. In Figure 5.3 (b), each $[90°/0°]$ layer is modeled using three elements through the thicknesses, one element is for the 90^o fiber direction and two elements are for the 0^o fiber direction. A total of 24 elements through the thickness is considered for the eight $[90°/0°]_8$ layers. The $90°$ fiber directions have one element thickness due to the low reinforcement and thinner layer in the transverse fiber directions. The fiber volume contents and thickness of each layer in a single ply of the GFRP skins are determined by matching the overall elastic properties of GFRP skins with $0°$ and $90°$ off-axis angles; see Kim et al. (2011) for a detailed discussion. The elastic properties for the isotropic epoxy resin at room temperature are determined from the tensile tests on a bulk epoxy specimen. The

mechanical properties for $0°$ and $90°$ E-glass/epoxy layers at room temperature are determined by using the simplified micromechanical model of unidirectional composites. The mechanical properties of each constituent and component are shown in Table 5.1. The time-dependent properties for epoxy matrix and polyurethane foam core are shown in Table 5.2. These properties are obtained from Kim et al. (2011). Tables 5.3 and 5.4 present the thermal properties for the constituents of the sandwich composites.

Table 5.1 Elastic properties for constituents of the sandwich composites at room temperature

Constituents	$E_{11} = E_{22}$ [MPa]	v_{12}
E-glass fiber	72,000	0.25
Epoxy matrix	3020	0.2977
Polyurethane foam	22.78	0.3
Lead Zirconia Titanate (PZT) wafer	80,000	0.34

Table 5.2 Time-dependent compliance for epoxy matrix and polyurethane foam core

n	λ_n [S^{-1}]	D_n (Epoxy) [MPa^{-1}]	D_n (Foam) [MPa^{-1}]
1	1	2×10^{-6}	5×10^{-4}
2	1×10^{-1}	3×10^{-6}	5×10^{-4}
3	1×10^{-2}	7×10^{-6}	1×10^{-3}
4	1×10^{-3}	2×10^{-5}	2×10^{-2}
5	1×10^{-4}	2×10^{-5}	1.3×10^{-2}
6	1×10^{-5}	3×10^{-5}	1.5×10^{-2}
7	1×10^{-6}	–	2×10^{-2}
8	1×10^{-7}	–	2×10^{-2}

Table 5.3 thermal conductivity for smart sandwich composites

Thermal Conductivity [W/m K]	k_{11} (longitudinal)	$k_{22}=k_{33}$ (transverse)
E-glass fibers	1.1	1.1
epoxy matrix	0.188	
polyurethane foam	0.029	
Lead Zirconia Titanate (PZT) wafer	1.1	

Table 5.4 CTE of smart sandwich composite constituents

CTE	E-glass	Epoxy	Polyurethane foam	PZT
α [10^{-6}/K]	5	52.5	76.2	50

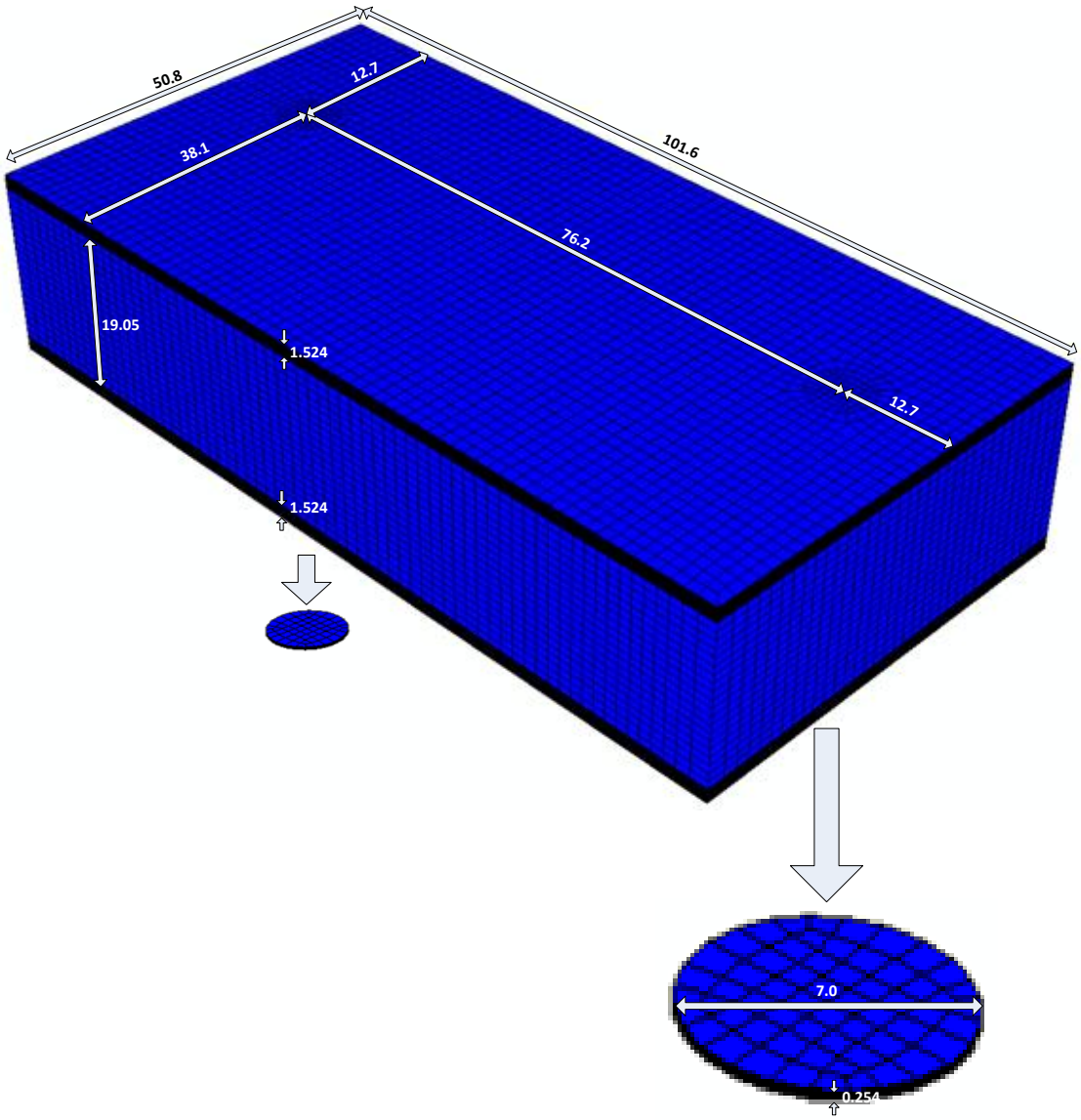

Figure 5.3 (a) Dimensions of sandwich composites with PZT

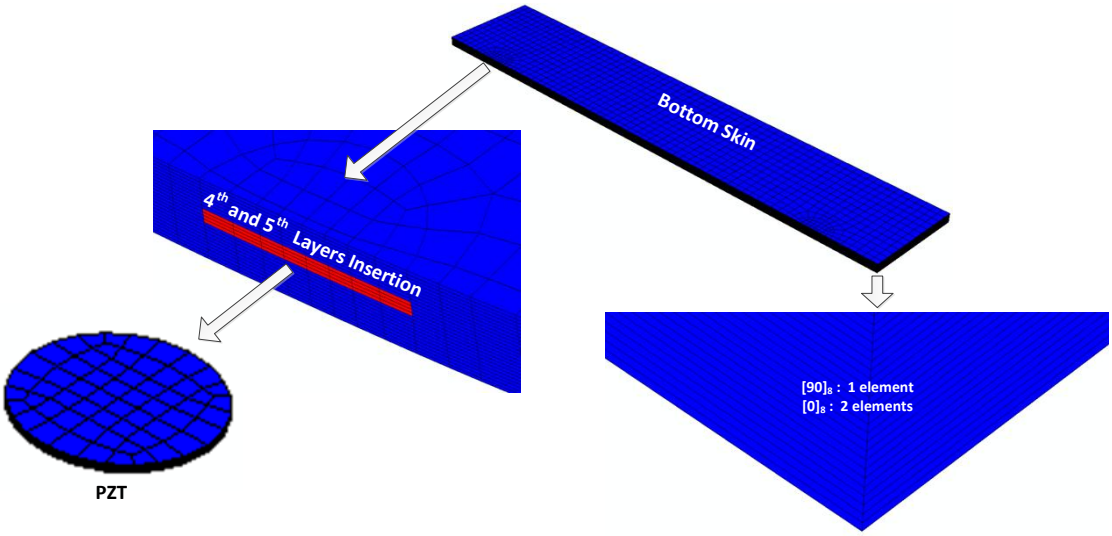

Figure 5.3 (b) Bottom skin of E-glass/epoxy with PZT insertion

For the thermo-mechanical analysis of the smart sandwich beam, two analyses are performed sequentially. First, the heat conduction analysis in the sandwich composite is performed to determine the temperatures at nodal points. Second, the thermo-mechanical three-point bending analysis is performed to determine the deformations and stresses in the sandwich beam subjected to coupled thermo-mechanical effects. The boundary conditions for the heat conduction are shown in Figure 5.4. For the transient heat conduction, the composite is initially at 293K and then subjected to 353K on its surfaces. The transient heat conduction analysis continues within the temperature gradient tolerance (0.05), which reaches around 306.5 seconds. The boundary conditions of the thermo-mechanical analysis are shown in Figure 5.5. The sandwich composite structure experiences thermal expansion due to increase in

temperature during the heat conduction process. The mechanical loading of 186.6 N is then applied on the mid-section of the beam for 1200 seconds, as shown in Figure 5.5.

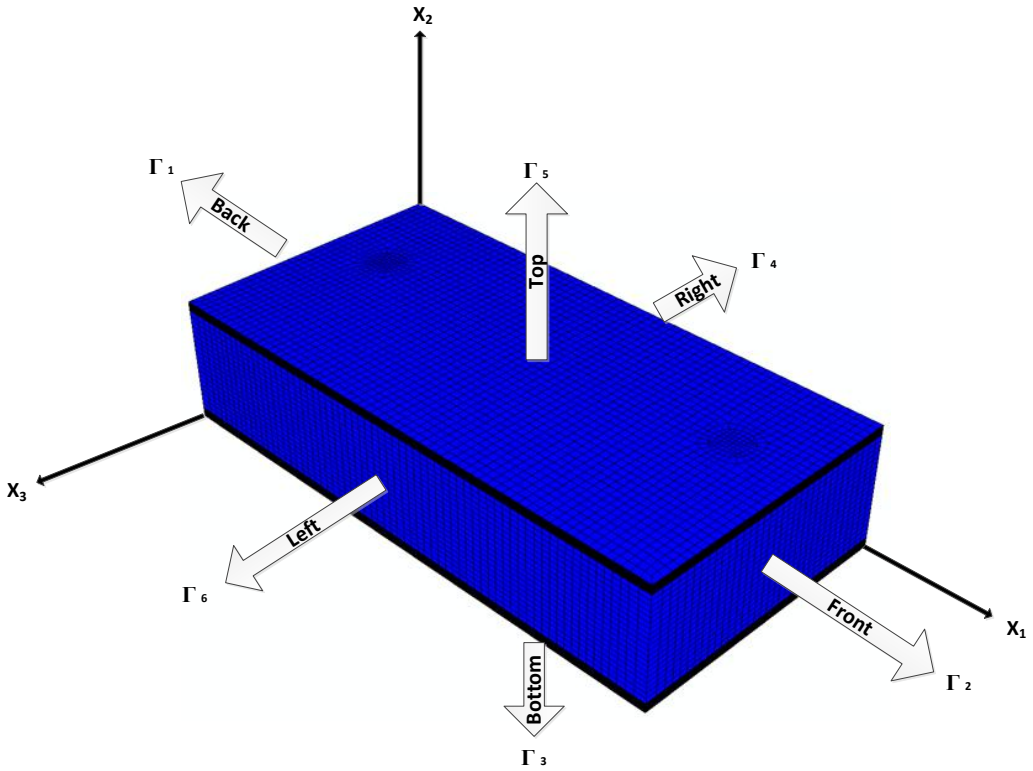

$$\text{B.C.}: T(x_1, x_2, x_3, t) = 353\text{K} \text{ on } \Gamma_1, \Gamma_2, \Gamma_3, \Gamma_4, \Gamma_5, \Gamma_6$$

$$\text{I.C.}: T(x_1, x_2, x_3, 0) = 293\text{K}$$

$$\text{,where } 0 \le x_1 \le \Gamma_2,\ 0 \le x_2 \le \Gamma_5,\ 0 \le x_3 \le \Gamma_6$$

Figure 5.4 Boundary conditions of heat conduction in the sandwich composites

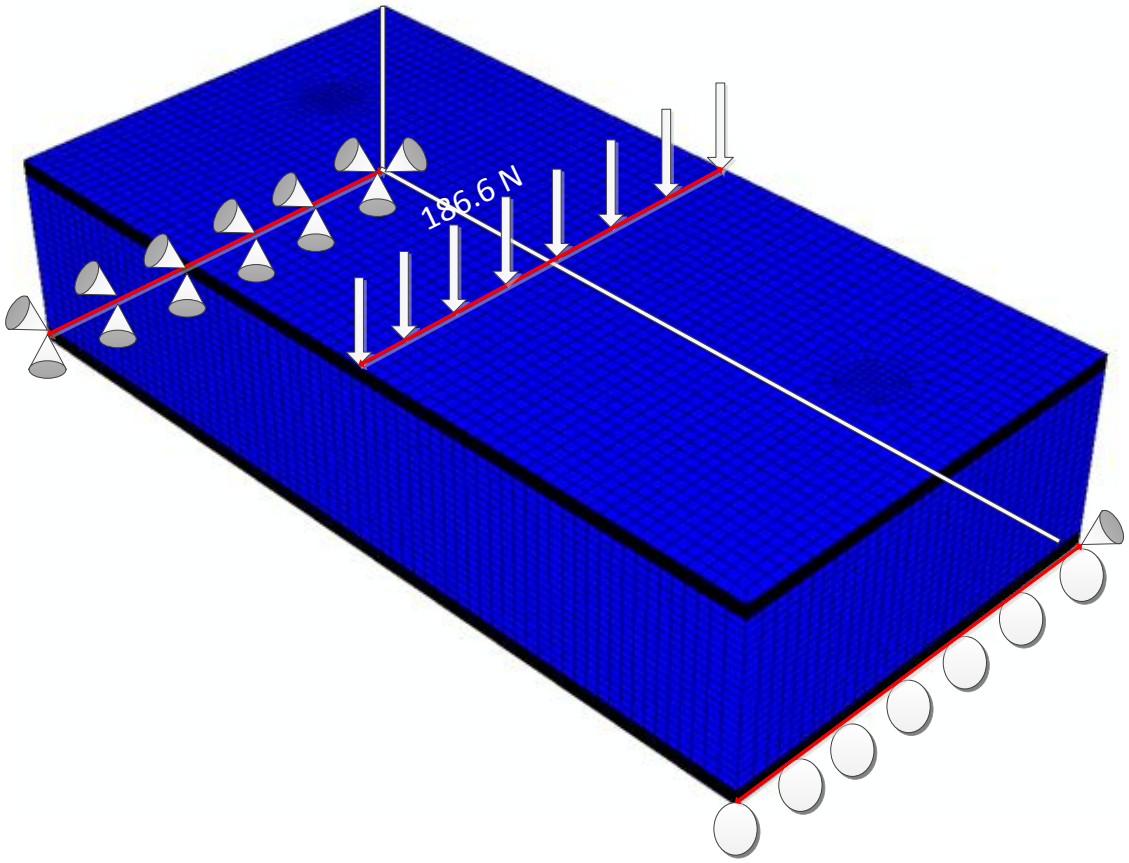

Figure 5.5 Boundary conditions of three-point bending in the sandwich composites

5.3 Analyses of Coupled Heat Conductions and Thermo-mechanical Loading in Sandwich Beams

The temperature profiles during the heat conduction analysis are shown in Figure 5.6. The temperatures are reported at several instants of time till reaching at 306.5 seconds which is within the tolerance (0.05). Figure 5.6 (a) shows heat conduction within FRP skins, which reaches steady state at 29 seconds. The half of the smart

sandwich beams is presented in Figure 5.6 (b), and the progress of heat conduction until steady state is shown.

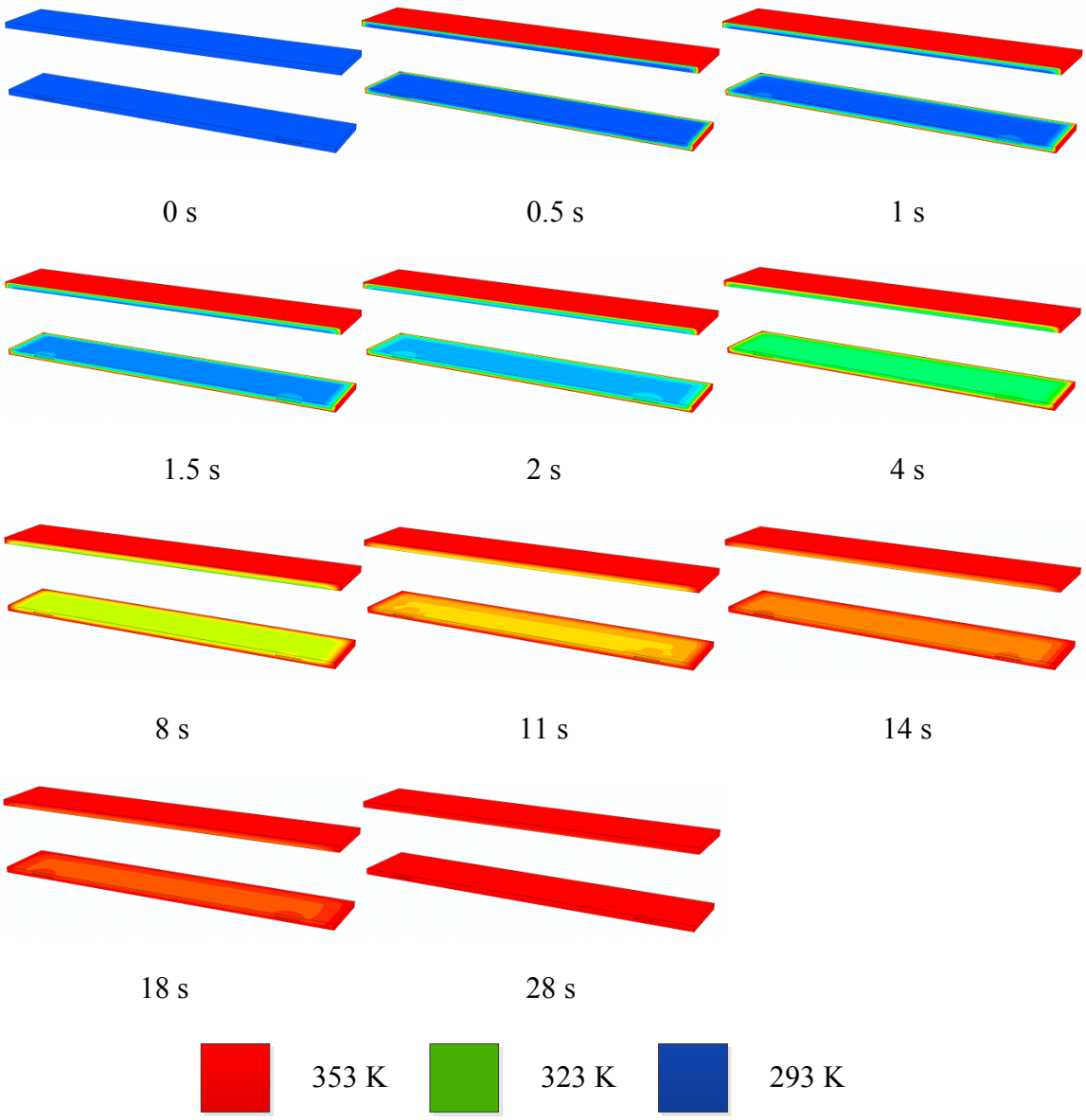

Figure 5.6 (a) Temperature contours of top and bottom skins in heat conduction analysis

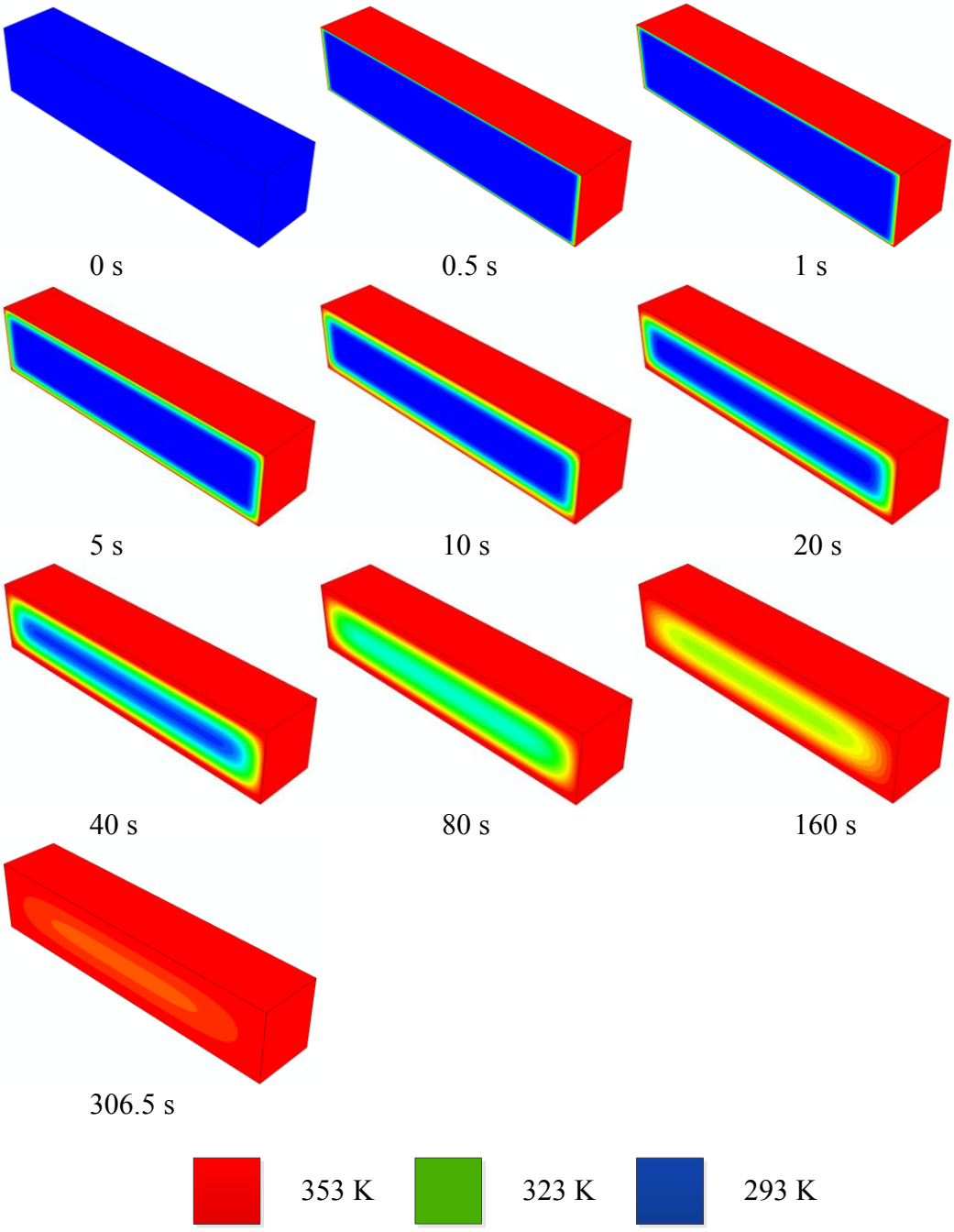

Figure 5.6 (b) Temperature contours of the sandwich structure in heat conduction analysis

Next, a thermo-mechanical analysis is performed. The thermal expansion and temperature-dependent material properties result in the thermo-mechanical coupling response. The smart sandwich composites comprise of polymer components so that it is expected to show the time-dependent response during the thermo-mechanical analysis. The embedded PZT sensors have an important role in monitoring the life performance of the structure under histories of loadings. The stress analysis of the smart sandwich structure is important because the embedded PZT wafers within plies of the skins result in discontinuous materials and geometry, so that stress concentrations may occur around the regions where the discontinuities exist. Due to the different thermal expansion coefficients, the interfaces of each component present the stress concentration shown in Figures 5.8 and 5.9 during the transient heat conduction. The polyurethane foam core experiences compressive stress along the longitudinal (x_1) direction, as shown in Figure 5.7 (a) due to the constrained from the top and bottom skins. The compressive stresses are due to higher thermal expansion coefficient of the foam core compared to the one of the skins. High stress concentrations are also generated the around PZT. Figure 5.8 presents the stress distribution in E-glass/epoxy skins with PZT. The PZT wafers are extremely compressed due to the thermal expansion of E-glass/epoxy (-172MPa). The PZT wafers are trapped in E-glass/epoxy skins and each component has a different thermal expansion yielding different directional stress. On the other hand, the FRP skins surroundings the PZT wafers experience tensile stress (66MPa). The localize stresses may cause the debonding of layers or fracture within the layers. The lateral deflections in the foam and skins at both top and bottom regions during the transient heat conduction

are also monitored, as shown in Figure 5.10. The deformation shows mainly elastic behaviors, which are dominated by the E-glass fibers. The thermal stresses show negligible creep deformation.

After steady state temperature is reached, the sandwich beam is subjected to a concentration load of 186.6 N for about 108 hours. In the bending simulation, the top and bottom skins presents stress concentration between 66MPa and -10MPa, as shown in Figure 5.9 (a). The overall lateral displacement of the sandwich beam during three-point bending creep analysis is presented in Figure 5.11. The FE simulation is performed with two different element types, linear (C3D8) and quadratic (C3D20) elements. The number of linear elements is 24080 and the number of quadratic elements is 168232. The number of quadratic elements is approximately seven times larger than that of linear elements. The quadratic elements present around 2% more deflection than the linear elements. However, the predictions of the creep responses of the smart sandwich composite from the two element types show a good agreement with the experimental data reported by Kim et al. (2011), as shown in Fig. 5.11.

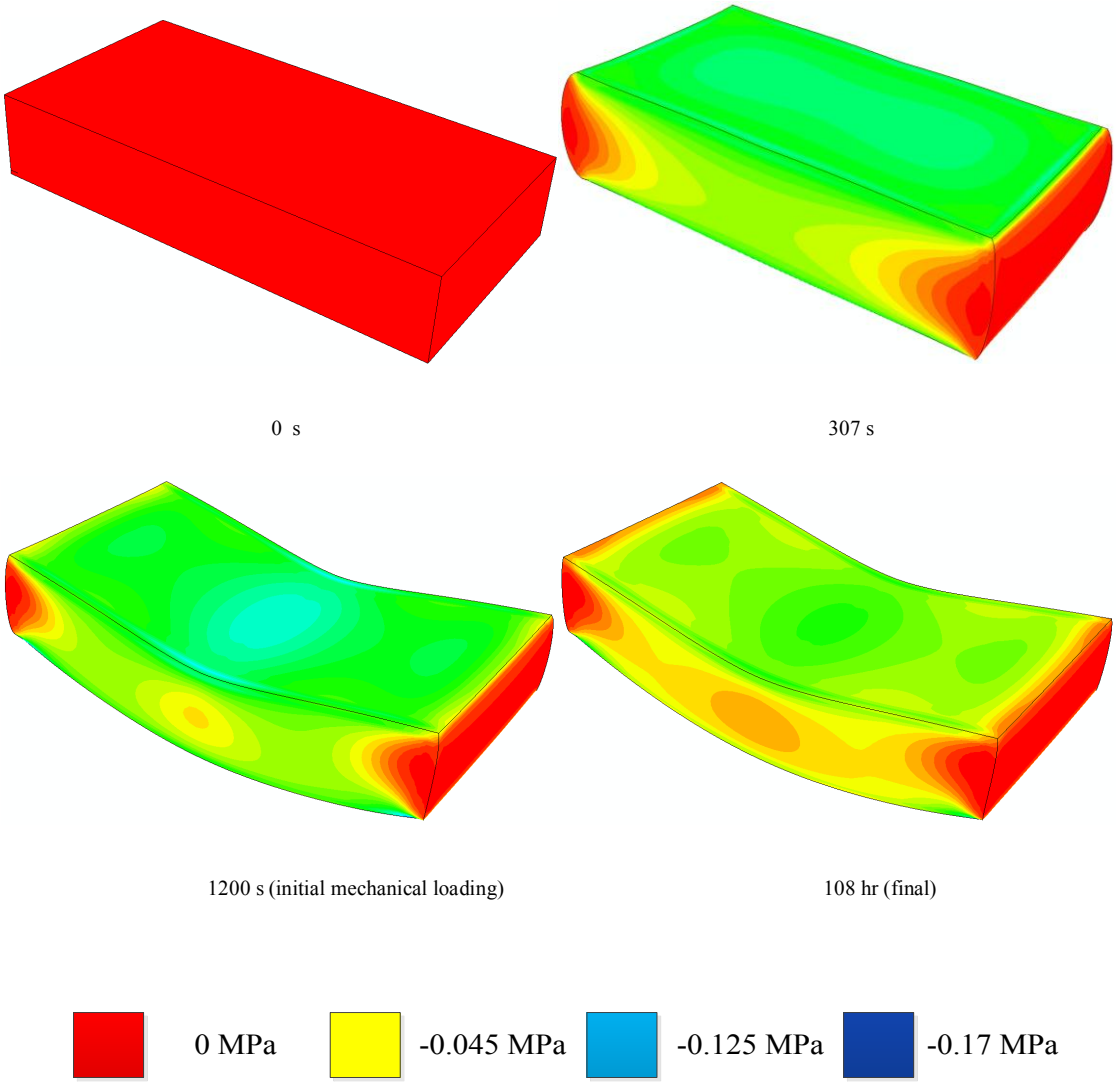

Figure 5.7 (a) Stress contours (S_{11}) of polyurethane core

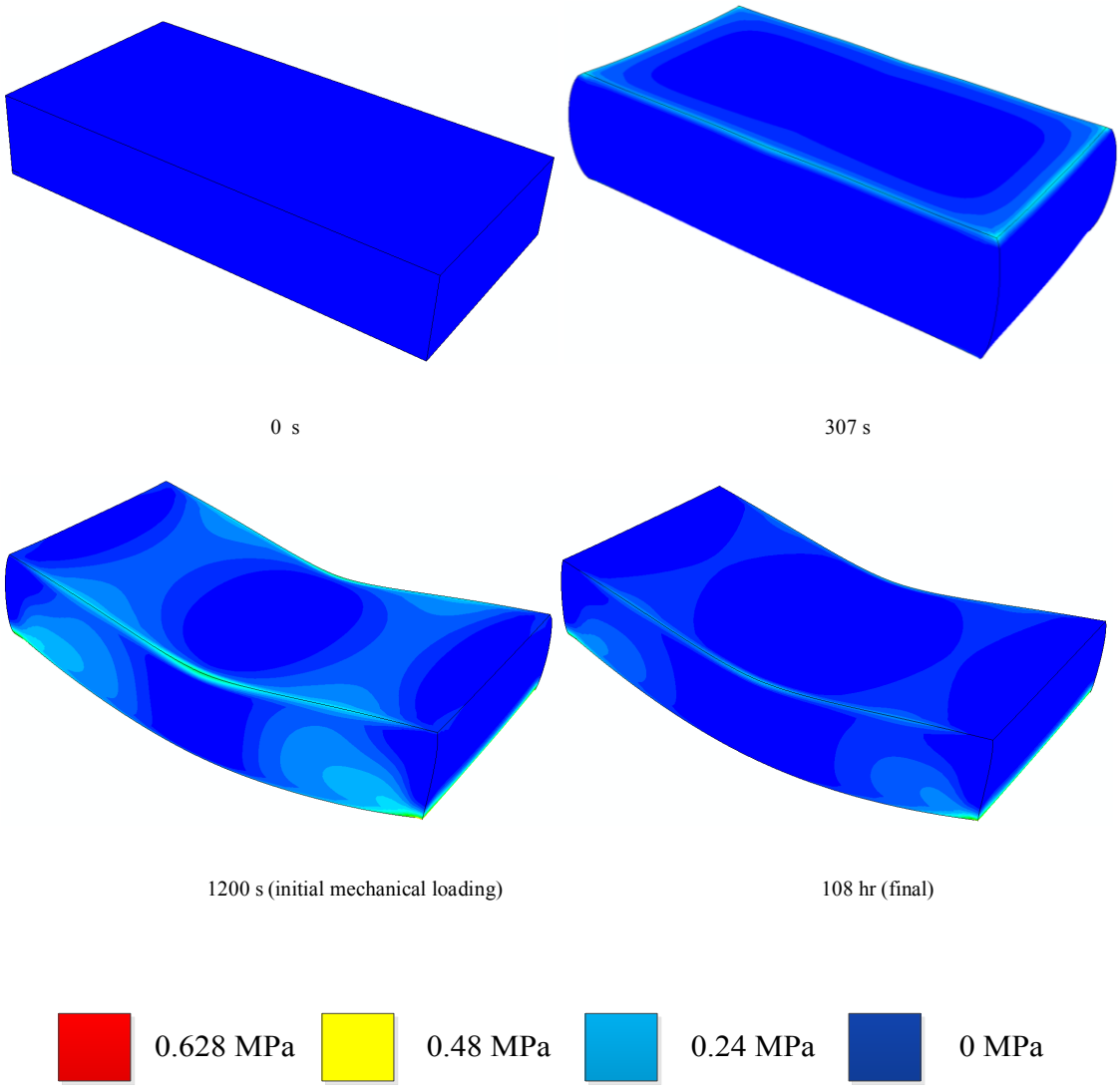

Figure 5.7 (b) Stress contours (von Mises) of polyurethane core

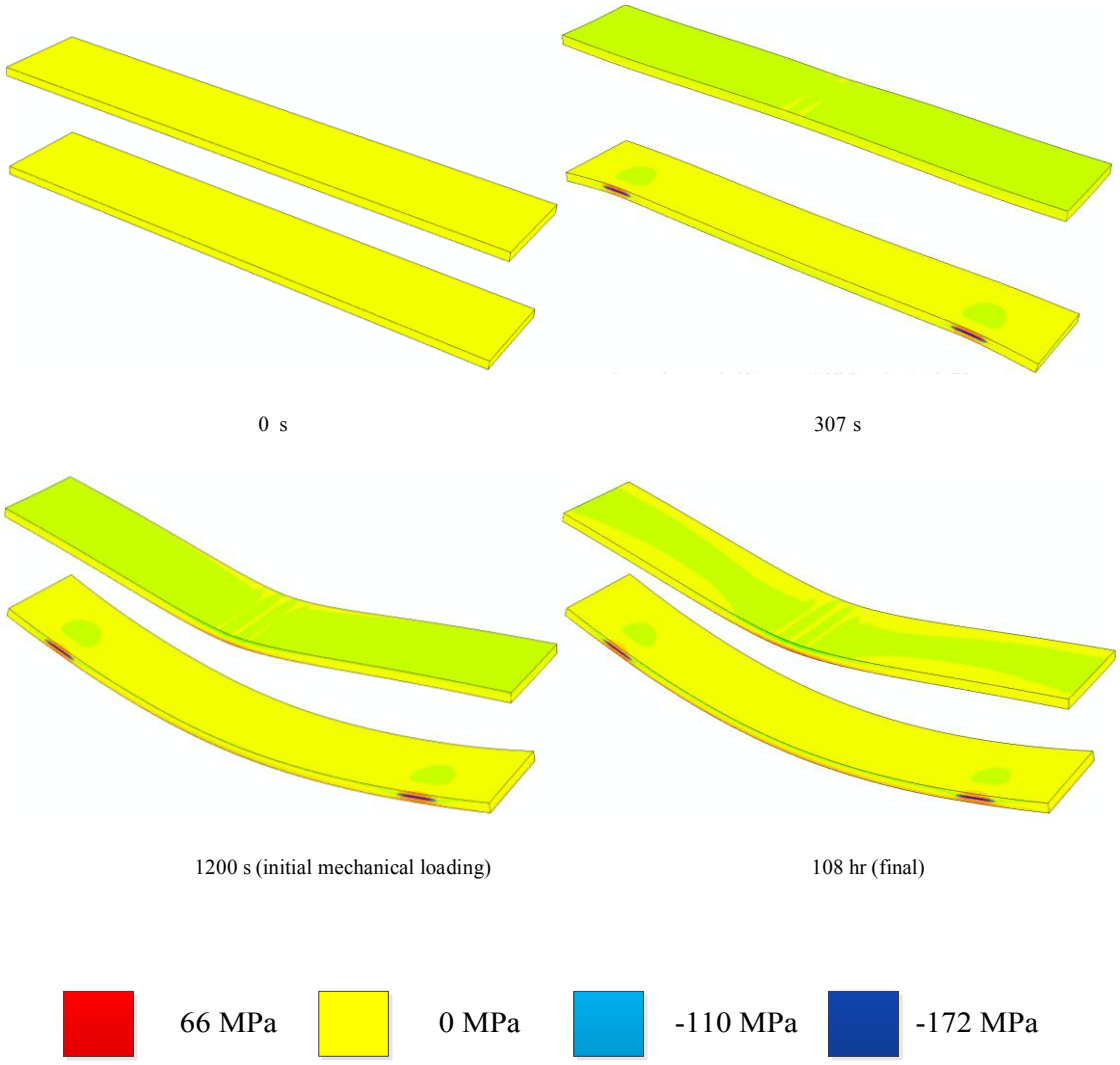

Figure 5.8 (a) Stress contours (S_{11}) of E-glass/epoxy skins

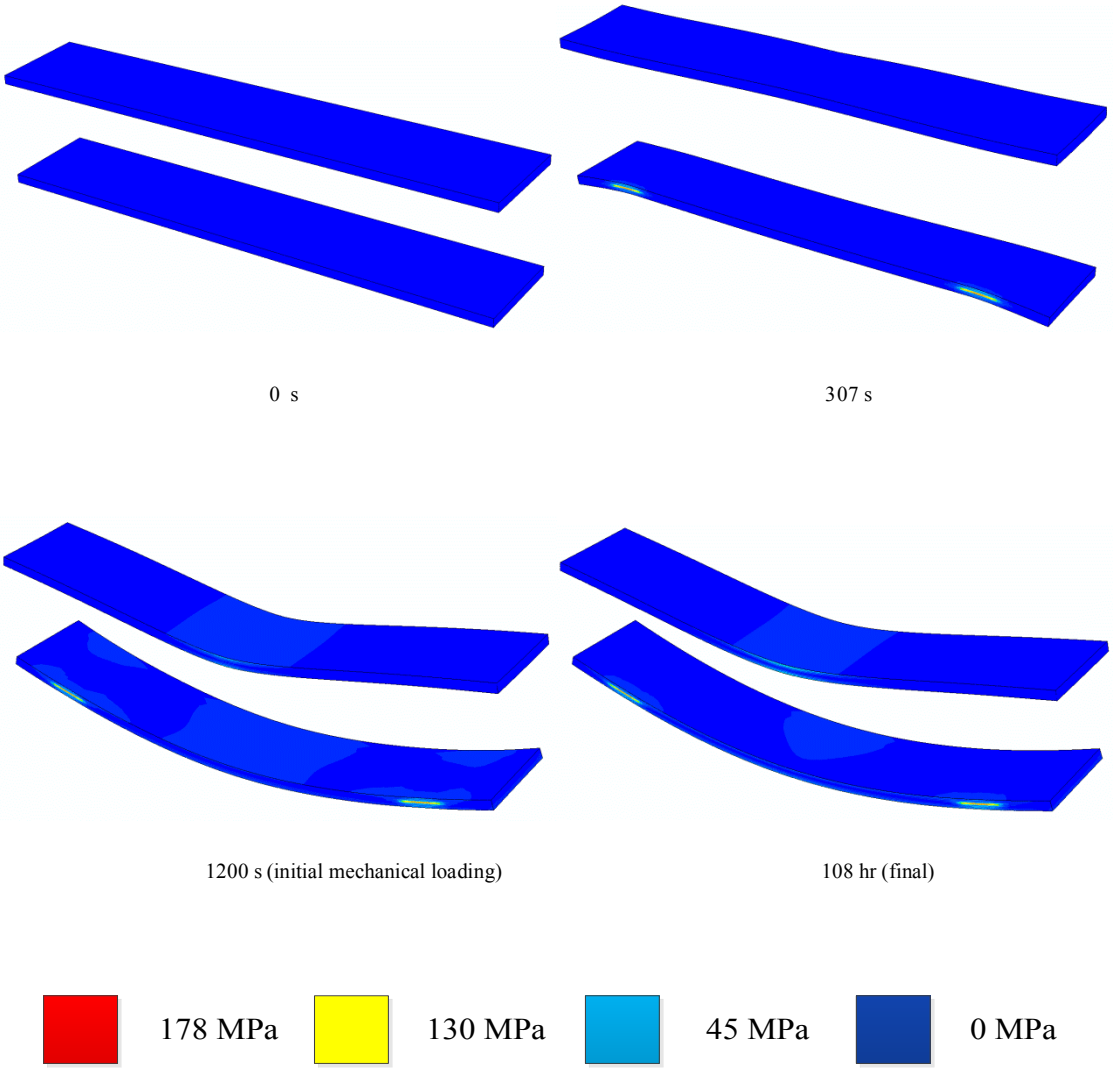

Figure 5.8 (b) Stress contours (von Mises) of E-glass/epoxy skins

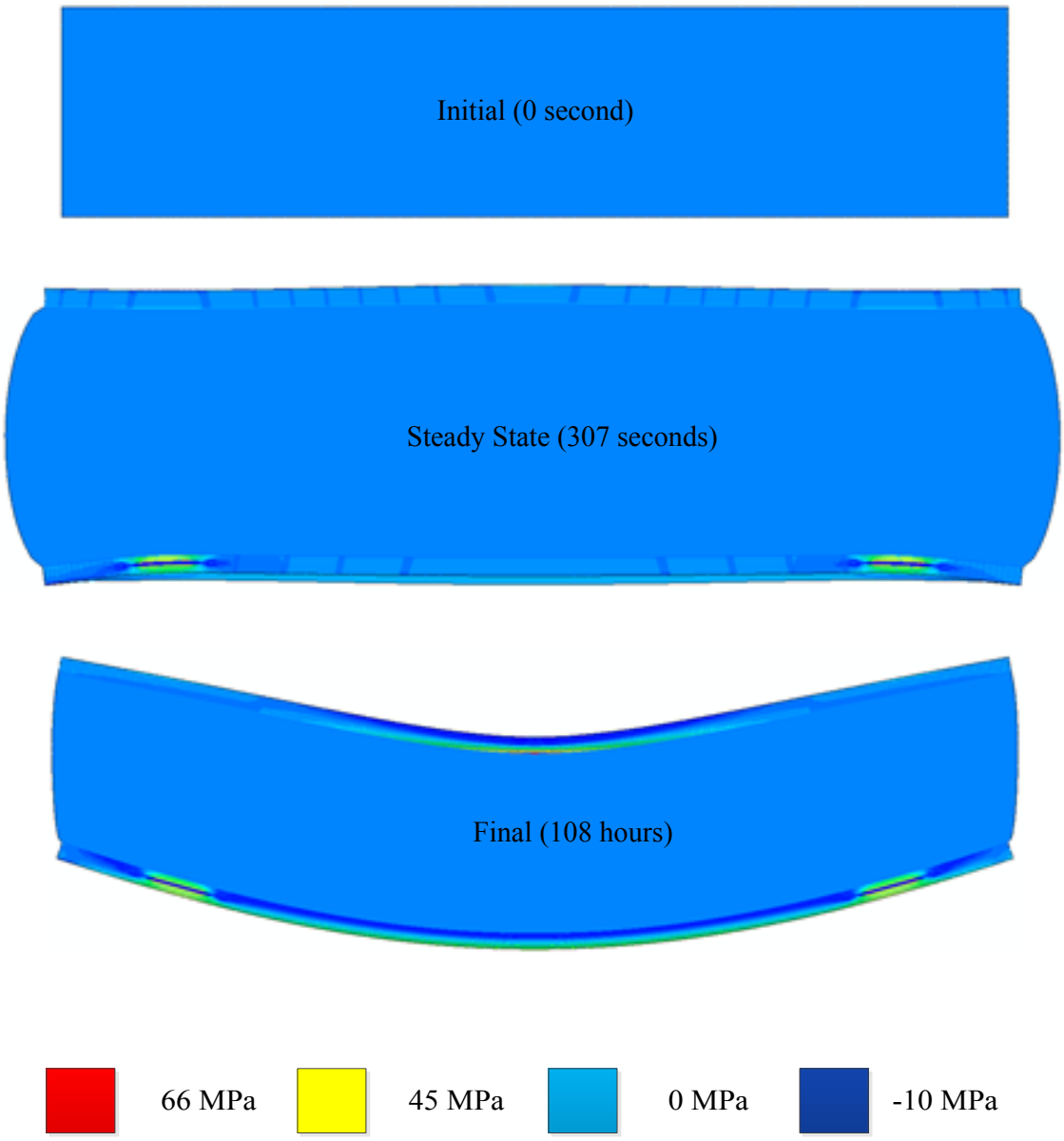

Figure 5.9 (a) Stress contours (S_{11}) of smart sandwich composites

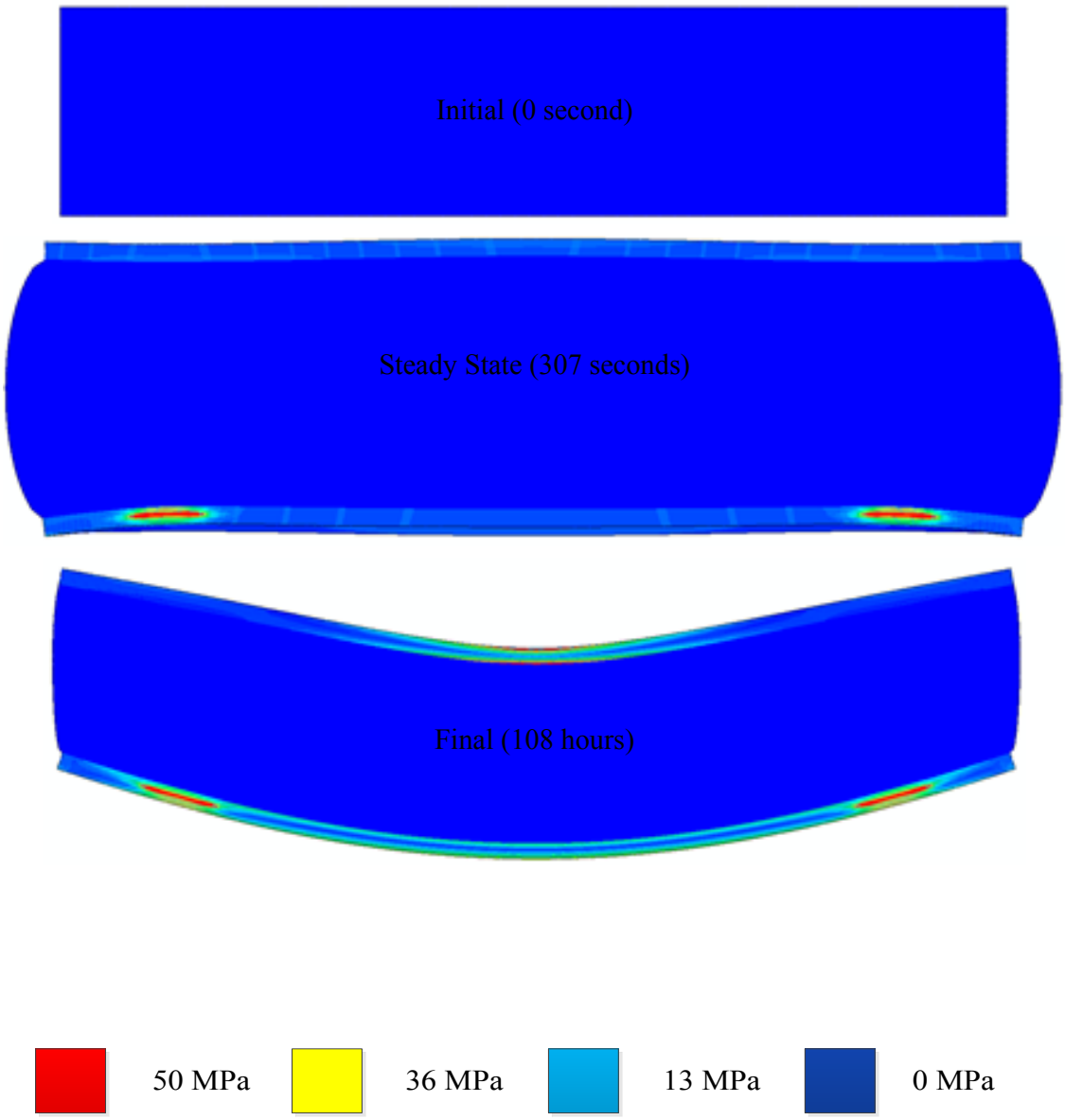

Figure 5.9 (b) Stress contours (von Mises) of smart sandwich composites

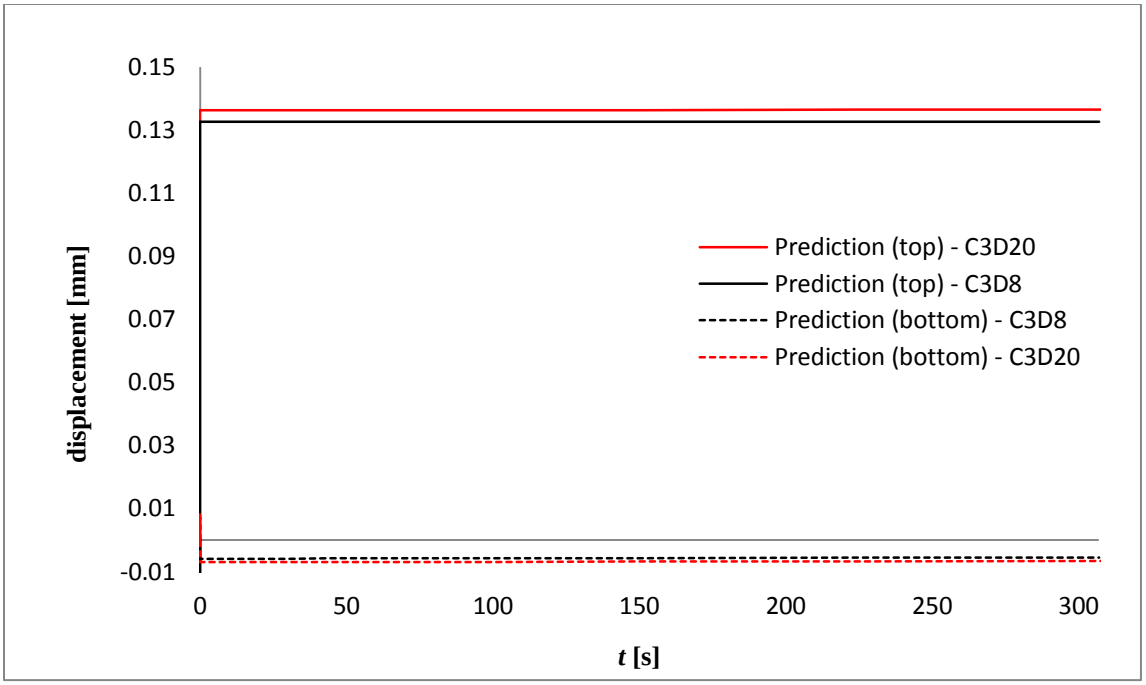

Figure 5.10 The elastic response of thermal expansion during transient time

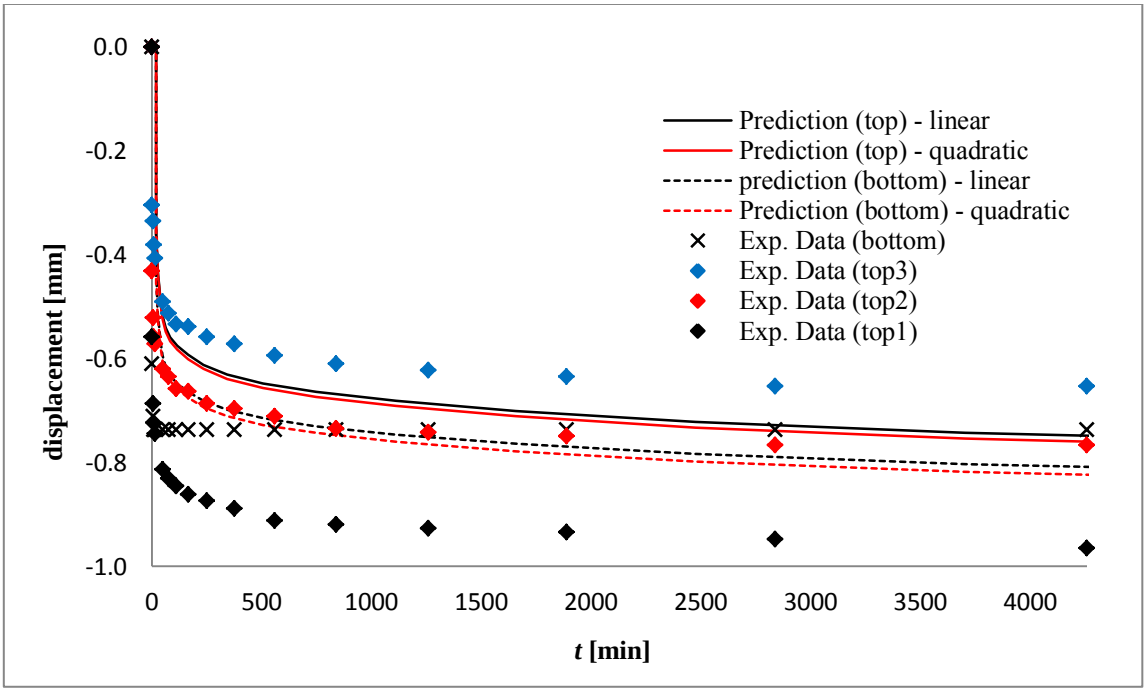

Figure 5.11 The creep response of three point bending

CHAPTER VI

CONCLUSION AND FUTURE RESEARCH

6.1 Conclusions

An integrated micromechanical and FE framework has been developed for analyzing heat conduction and thermo-mechanical deformation of FRP composite materials and structures. The studied FRP composite consists of polymeric matrix that experiences combined viscoelastic-viscoplastic behaviors and elastic fiber reinforcements. A simplified micromechanical model, which is a unit-cell (UC) model comprising of four subcells, has been formulated for analyzing time-dependent response of FRP composites subjected to coupled mechanical loading and thermal effect. A nested time-integration algorithm has been developed for analyzing the overall heat conduction and thermo-mechanical deformation response of FRP composites, having viscoelastic-viscoplastic constitutive model for isotropic polymeric constituents. The UC model results in orthotropic homogenized properties, i.e., the effective thermal conductivity, effective heat capacity, effective coefficient of thermal expansion, effective elastic moduli, and time-dependent responses of the composites. The time integration algorithm and micromechanical models are implemented in user material subroutines (UMAT, UMATHT, UEXPAN) in commercial FE software, ABAQUS, and used for analyzing coupled heat conduction and deformation of FRP composite structures. The research findings from each chapter are discussed as follows:

1) In Chapter II, a time integration algorithm is formulated to solve for a viscoelastic-viscoplastic constitutive equation of polymers with temperature

effect. The polymers are assumed to be isotropic and the constitutive model is derived based on continuum mechanics theory for materials undergoing small deformation gradients. A total strain is decomposed into the viscoelastic, viscoplastic, and thermal strain components. The Schapery's single integral equation is used for the 3D isotropic nonlinear viscoelastic responses. The Perzyna model is used for the viscoplastic response. In addition, parametric studies have been done in order to understand the effects of temperatures on the combined viscoelastic and viscoplastic response. The material parameters in the constitutive models are allowed to vary with temperatures, i.e., higher temperature accelerates the creep deformations, soften the material response, and increase the plastic deformations.

2) In Chapter III, a simplified micromechanical model consisting of four-cells, a UC model, is formulated to predict the time-dependent behavior of heterogeneous FRP composites. A representative volume element is chosen from a periodic array of square fibers dispersed in polymeric matrix. The simplified micromechanical model consists of unidirectional elastic fiber for one sub-cell and viscoelastic-viscoplastic matrix for other three sub-cells. The average stresses and strains of the FRP composite are formulated by using a volume-averaging scheme. Linearized micromechanical relations are derived by satisfying traction continuity and displacement compatibility. Two integrated iteration algorithms are performed to minimize errors from linearizing the nonlinear responses. The first iteration is done at the matrix subcells for the time

dependent polymer matrix and the second iteration is used for the micromechanical relations of an orthotropic medium. For verification of the UC model, experimental data available in literature on combined viscoelastic-viscoplastic response are compared to the time-dependent response obtained from the UC model. Furthermore, micromechanical models of FRP composites with detailed fiber arrangements have been generated using FE, termed as detailed FE microstructures, for composites with several fiber volume contents. The mechanical responses obtained from the UC model are compared to the ones of the detailed FE microstructures. The detailed FE microstructures can capture the stress concentrations in the FRP composite, which the UC model is not capable of. The overall responses predicted from the two models are relatively in good agreements.

3) In Chapter IV, a coupled heat conduction and thermo-mechanical analysis is performed for FRP composites using the integrated micromechanical model and FE framework. The UC model in Chapter III is modified to determine the effective thermal conductivity and heat capacity of FRP composites. Fourier's law is considered for the heat conduction and the volume-averaging scheme is used for obtaining the effective heat flux and temperature gradient. In order to verify the heat conduction analysis from the UC model, FRP microstructures with detailed fiber arrangements are generated using FE, for composites with various fiber volume fractions. The transient heat transfer analyses along the fiber axis and transverse to the fiber axis from the two models are compared. The

temperature profiles determined from the two models are relatively in good agreements. The thermo-mechanical behavior of FRP composite due to temperature changes is investigated and the effect of thermal stresses due to the mismatches in the thermal expansion coefficients of the fibers and matrix is also studied. Furthermore, the effective thermal expansion coefficients of FRP composites having glass fibers obtained from the UC model are compared to experimental data and other analytical solutions available in literature. Finally, the possible plastic deformation due to existence of high thermal stresses in the FRP composites is examined using the two micromechanical models. Localized thermal stresses are observed at various locations near the interfaces between fibers and matrix, which are captured in the micromechanical model with detailed fiber arrangements. However, the effect of plastic deformation due to thermal stresses on the overall time-dependent response of FRP composites is relatively small.

4) In Chapter V, thermo-mechanical analysis of composite structures is conducted on a polymeric sandwich beam under creep bending at elevated temperature using the integrated micromechanical model and FE framework. The studied sandwich beam consists of polyurethane foam core, GFRP skins, and PZT wafers, which exhibit different thermo-mechanical behaviors. The UC model is used to provide homogenized properties and response of the GFRP skins. The transient heat conduction analysis is performed to simulate heating the sandwich composite from room temperature to the testing temperature (80^{o}C). High

thermal stress concentrations are presented near the PZT wafers. Next, a concentrated load is applied at the mid-span of the sandwich beam in order to simulate three-point creep bending. The creep deflection shows a good agreement with experimental data.

6.2 Future Research

The current research can be extended as follows:

1) Localized stresses and long-term exposures to elevated temperatures could degrade the properties of the constituents in the FRP composites, such as oxidation in the polymeric matrix at high temperatures. The micromechanical models can be modified to incorporate the degradation in the constituents and/or chemical reaction such as oxidation due to temperature changes.
2) Polymers and FRP composites experience significant creep deformations under high mechanical loadings and at elevated temperatures. These creep deformations could lead to progressive deformations (tertiary creep stage) and material failures. Thus, the viscoelastic-viscoplastic constitutive model and micromechanical model can be extended to include damage and progressive crack propagation in the polymers and FRP composites.
3) Besides external loadings and temperature changes, other environmental effects such as humidity and ultraviolet exposure can cause the deterioration in the polymers and FRP composites. These factors should be studied and

coupled to the thermo-viscoelastic-viscoplastic models in order to better predict life performance of polymers and FRP composites.

4) Finally, the time-dependent thermo-mechanical study of polymers and FRP composites can be extended to understand fatigue failures in polymer and FRP composites due to various cycles of mechanical loading and temperatures, and other environmental effects.

REFERENCES

Aboudi, J. (1991), "Mechanics of composite materials: a unified micromechanical approach," Amsterdam, Elsevier.

Aboudi, J. (2005), "Micromechanically established constitutive equations for multiphase materials with viscoelastic–viscoplastic phases," Mech. Time-Depend. Mater, Vol. 9, 121-145.

Bhargava, P. (2007), "High temperature properties of HFPE-II-52 polyimide resin and composites," Ph.D. Dissertation, Cornell University.

Bodner, S.R., Partom, Y. (1975), "Constitutive equation for elasto-viscoplastic strain hardening material," ASME J. Al. Mech, 385-389.

Bradshaw, R. D., Brinson, L. C. (1999), "Mechanical response of linear viscoelastic composite laminates incorporating non-isothermal physical aging effects," Composite Science and Technology, Vol. 59, 1411-1427.

Budiansky, B. (1965), "On the elastic moduli of some heterogeneous materials," J. Mech. Phys. Solids, Vol. 13, 223-227.

Budiansky, B., Wu (1962), Proc. 4th U.S. Nat. Congr. Appl. Mech. (1962), 1175.

Cai, H., Miyano, Y., Nakada, M. (2010), "Prediction of long term flexural fatigue strength of honeycomb sandwich composites," Journal of Reinforced Plastics and Composites, Vol. 29, No. 2, 266-277.

Caruthers, J., Cohen, R. (1980), "Consequences of thermo-rheological complexity in viscoelastic materials," Rheol. Acta, Vol. 19, 606-613.

Chailleux, E., Davies, P. (2003), "Modeling the nonlinear viscoelastic–viscoplastic behavior of aramid fiber yarns," Mech. Time-Depend. Mater, Vol. 7, 291-301.

Chailleux, E., Davies, P. (2005), "A nonlinear viscoelastic–viscoplastic model for the behavior of polyester fibers," Mech. Time-Depend. Mater, Vol. 9, 147-160.

Chien, L.S., Tzeng, J.T. (1993), "The analysis of viscoelastic stress of thick laminated composite cylinders at an elevated temperature," Proc. 34th AIAA Structural Dynamics and Materials Conf, La Jolla, CA, AIAA, Washington, DC.

Christensen, R. M. and Lo, K. H. (1979), "Solutions for effective shear properties in three phase sphere cylinder models," Journal Mechanics Physics Solids, Vol. 27, 315-330.

Colak, O.U. (2005), "Modeling deformation behavior of polymers with viscoplasticity theory based on overstress," Int. J. Plasticity, Vol. 21, 145-160.

Coleman, B. D. (1964), "Thermodynamics of materials with memory," Arch. Ratl Mechanics Anal., Vol. 17, 1.

Dillard, D. A., Straight, M. R., Brinson, H. F (1987), "The nonlinear viscoelastic characterization of graphite/epoxy composites," Polymer Engineering and Science, Vol. 27, No. 2, 116-123.

Drozdov, A. (1999), "A constitutive model in viscoelasto plasticity of glassy polymers," Polymer, Vol. 40, No. 13, 3711-3727.

Drozdov, A.D., Christiansen, J. C. (2008), "Thermo-viscoelastic, viscoplastic behavior of high-density polyethylene," Int. J. of Solids and Structures, Vol. 45, 4274-4288.

Dvorak, G. J., Bahei-El-Din, Y. A., (1979) "Elastic–plastic behavior of fibrous composites," Journal of Mechanics and Physics of Solids, Vol. 27, 51-72.

Eshelby, J.D. (1957), "The determination of the elastic field of an ellipsoidal inclusion, and related problem," Proc. Roy. Soc. Lond, A, Vol. 241, No. 1226, 376-396.

Falcone, C.M., Ruggles-Wrenn, M.B. (2009), "Rate dependence and short-term creep behavior of a thermoset polymer at elevated temperature," J. Pressure Vessel Technol., 1-8.

Findley, W.N., Lai, J.S.Y. (1967), "A modified superposition principle applied to creep and nonlinear viscoelastic material under abrupt changes in state of combined stress," Trans. Soc. Rheol. Vol. 11, 361.

Fisher, F.T., Brinson, L.C. (2001), "Viscoelastic interphases in polymer matrix composites: Theoretical models and finite element analysis," Composites Science and Technology, Vol. 61, 731-748.

Frank, G.J. (1998), "A constitutive model for the mechanical responses of glassy polymers," PhD. Dissertation, University of Dayton, Dayton, Ohio.

Frank, G.J., Brockman, R.A. (2001), "A viscoelastic–viscoplastic constitutive model for glassy polymers," Int. J. Solids Struct, Vol. 38, 5149-5164.

Green, A.E., Rivlin, R. S (1957), "The mechanics of nonlinear materials with memory, part I" Arch. Ratl Mechanics Anal., Vol. 1, 1.

Guedes, R. M., Marques, A. T., Cardon, A. H. (1998), "Analytical and experimental evaluation of nonlinear viscoelastic-viscoplastic composite laminates under creep, creep-recovery, relaxation and ramp loading," Mechanics of Time-Dependent Materials, Vol. 2, 113-128.

Haj-Ali, R. M., Muliana, A. H. (2003), "Micromechanical models for the nonlinear viscoelastic behavior of pultruded composite materials," Int. J. Solids and Structures, Vol. 40, 1037-1057.

Haj-Ali, R. M., Muliana, A. H. (2004), "Numerical finite element formulation of the schapery nonlinear viscoelastic material model," Int. Journal of Numerical Method in Engineering, Vol. 59, No. 1, 25-45.

Haj-Ali, R. M., Pecknold, D. A. (1996), "Hierarchical material models with microstructure for nonlinear analysis of progressive damage in laminated composite structures," Structural Research Series No. 611, UILU-ENG-96-2007, Department of Civil Engineering, University of Illinois at Urbana-Champaign.

Hall, R.B. (2005), "A thermodynamic framework for viscoplastic based on overstress," ASME J. Eng. Mater. Technol, Vol. 127, 369-373.

Harper, B.D., Weitsman, Y. (1985), "Characterization method for a class of thermorhelogically complex materials," Journal of Rheology, Vol. 29, No.1, 49-66.

Hashin, Z., Rosen, B. W. (1964), "The elastic moduli of fiber reinfoced materials," journal applied mechanics, Vol. 31, 223-232.

Heeres, O.M., Suiker, A.S. J., de Borst, R. (2002), "A comparison between the Perzyna viscoplastic model, the consistency viscoplastic model," European J. Mech. A, Vol. 21, 1-12.

Henriksen, M. (1984), "Nonlinear viscoelastic stress analysis - a finite element approach," Computer and Structures, Vol. 18, No. 1, 133-139.

Hershey, A.V. (1954), "The elasticity of an isotropic aggregate of anisotropic cubic crystals," J. Appl. Mech., Vol. 21, 226–240.

Hill, R. (1964), "Theory of mechanical properties of fiber-strengthened materials: I elastic behavior," Journal Mechanics Physics Solids, Vol. 12, 192-212.

Hill, R., (1965), "A self-consistent mechanics of composite materials," J. Mech. Phys. Solids, Vol. 12, 213-222.

Hirsekorn, M., Petitjean, F., Deramecourt, A. , "A semi-analytical integration method for the numerical simulation of nonlinear visco-elasto-plastic materials," Mechanics of Time-Dependent Materials, Vol. 15, 139-167.

Karadeniz Z. H., Kumlutas D. (2007), "A numerical study on the coefficients of thermal expansion of fiber reinforced composite materials," Composite Structures, Vol. 78, 1-10.

Kennedy, T.C. (1998), "Nonlinear viscoelastic analyses of composite plates and shells," Composite Structures, Vol. 41, 265-272.

Kim, J.S., Muliana, A.H. (2009) "A time-integration method for the viscoelastic-viscoplastic analyses of polymers and finite element implementation," Int. J. Numer. Mech. Eng, Vol. 79, 550-575.

Kim, J.S., Arronche, L., Farrugia, A., Muliana, A., La Saponara, V. (2011), "Multi-scale modeling of time-dependent response of smart sandwich constructions," Composite Structures, Vol. 93, 2196-2207.

Kouznetsova, V., Brekelmans, W.A.M., Baaijens, F.P.T. (2001), "An approach to micro-macro modeling of heterogeneous materials," Computational Mechanics, Vol. 27, 37-48.

Krempl, E., Ho, K. (2000), "An overstress model for solid polymer deformation behavior applied to Nylon 66," ASTM STP 1357, 118-137.

Kroner, E. (1958), "Berechnung der elastischen konstanten des vielkristalls aus den konstanten des einkristalls," A. Phys., Vol. 151, 504-518.

Lai, J., Bakker, A. (1995), "An integral constitutive equation for nonlinear plasto-viscoelastic behavior of high-density Polyethylene," Polymer Eng. Sci., Vol. 35, 1339-1347.

Lai, J. S., Bakker, A. (1996), "3-D Schapery representation for nonlinear viscoelasticity and finite element implementation," Computational Mechanics, Vol. 18, 182-191.

Lai, J.S., Findley, W.N. (1973), "Creep of Polyurethane under varying temperature for nonlinear uniaxial stress," Transactions of The Society of Rheology, Vol. 17, No. 1, 63-87.

Landau, H.H., Weiner, J.H., Zwicky, E.E. (1960), "Thermal stress in a viscoelastic-plastic plate with temperature dependent yield stress," J. Applied Mechanics, Trans. ASME, Vol. 27, 297-302.

Laws, N. (1973), "On the thermostatics of composite materials," J. Mech. Phys. Solids, Vol. 21, 9-17.

Laws, N., McLaughlin, J.R. (1978), "Self-consistent estimates for the viscoelastic creep compliances of composites materials," Proc. R. Soc. Lond, Vol. 39, 627-649.

Leaderman, H., (1943), "Elastic and creep properties of filamentous materials and other high polymers," The Textile Foundation, Washington DC.

Lou, Y. C., Schapery, R. A. (1971), "Viscoelastic characterization of a nonlinear fiber-reinforced plastic," Journal of Composite Materials, Vol. 5, 208-234.

Martienssen, W., Warlimont, H. (2005), "Handbook of condensed matter and material data," 483.

Matsuda, T., Ohno, N., (2011), "Predicting the elastic-viscoplastic and creep of polymer matrix composites using homogenization theory," Creep and Fatigue in Composites, ed. R. M. Guedes, Woodhead Publishing, Cambridge, UK, 70-112.

Matweb (1997), "http://www.matweb.com," retrieved Sep 17, 2011.

Megnis, M., Varna, J. (2002), "Nonlinear viscoelastic, viscoplastic characterization of unidirectional GF/EP composite," Mechanics of Time-Dependent Materials, Vol. 7, 269-290.

Megnis, M., Varna, J. (2003), "Micromechanics based modeling of nonlinear viscoplastic response of unidirectional composite," Composites Science and Technology, Vol. 63, 19-31.

Mivehchi, H., Varvani-Farahani, A. (2011), "Temperature dependence of stress–fatigue life data of FRP composites," Mechanics of Composite Materials, Vol. 47, No. 3, 369-376.

Miyagawa, H., Sato, C., Mase, T., Drown, E., Drzal, L.T., Ikegami, K. (2005), "Transverse elastic modulus of carbon fibers measured by Raman spectroscopy," Materials Science and Engineering A, Vol. 412, 88-92.

Miyano, Y., Nakada, M., Cai, H. (2008), "Formulation of long-term creep and fatigue strengths of polymer composites based on accelerated testing methodology," Journal of Composite Materials, Vol. 42, No. 18, 1897-1919.

Mori, T., Tanaka, K. (1973), "Average stress in matrix, average elastic energy of materials with misfitting inclusions," Acta Metall, Vol. 21, 571-574.

Muddasani, M., Sawant, S., Muliana, A. (2010), "Thermo-viscoelastic responses of multilayered polymer composites: experimental and numerical studies," Composite Structures, Vol. 92, No. 11, 2641-2652.

Muliana, A.H., Khan, A. K. (2008), "A time integration scheme for stress-temperature dependent behaviors of adhesive polymer," Computational Materials Science, Vol. 41, 576-588.

Muianan, A.H., Kim, J.S. (2010), "A two-scale homogenization framework for nonlinear effective thermal conductivity of laminated composites," Acta Mechanica, Vol. 212, 319-347.

Muliana, A.H., Sawant, S. (2009), "Viscoelastic responses of polymer composites with temperature and time dependent constituents," Acta Mechanica, Vol. 204, 155-173.

Naghdi, P.M., Murch S.A. (1963), "On the mechanical behavior of viscoelastic/plastic solids," J. Appl. Mech., 321-328.

Nakada, M., Miyada, Y. (2009), "Accelerated testing for long term fatigue strength of various FRP laminates for marine use," Composites Science and Technology, Vol 69, 805-813.

Peretz, D., Weitsman, Y. (1982), "Nonlinear viscoelastic characterization of FM-73 adhesives," Journal of Rheology, Vol. 26, No. 3, 245-261.

Peretz, D., Weitsman, Y. (1983), "The non-linear thermo-viscoelastic characterization of FM-73 adhesives," Journal Rheology, Vol. 27, 97-114.

Perzyna, P. (1966), "Fundamental problems in viscoplasticity," Adv. Appl. Mech, Vol. 9, 243-377.

Perzyna, P. (1971), "Thermodynamic of rheological materials with internal changes," J. Mech, Vol. 10, 391-408.

Perzyna, P., Wojno, W. (1975), "Unified constitutive equations for elastic," Viscoplastic Materials, Vol. 24, 85-94.

Pipkin, A.C., Rogers, T.G. (1968), "A non-linear integral representation for viscoelastic behavior," J. Mech. Phys. Solids, Vol. 16, No.1, 59-72.

Poon, H., Ahmad, F. (1999), "A finite element constitutive update scheme for anisotropic, viscoelastic solids exhibiting non-linearity of the Schapery type," International Journal of Numerical Method in Engineering, Vol. 46, 2027-2041.

Reuss, A. (1929). “Berechnung der fließgrenze von mischkristallen auf grund der plastizitätsbedingung für einkristalle”. Journal of Applied Mathematics and Mechanics, Vol. 9, 49-58.

Rosen, B.W., Hashin, Z. (1970), “Effective thermal expansion coefficients and specific heats of composite materials,” Int. J. Engrg Sci., Vol. 8, 157-173.

Sadkin, Y., Aboudi, J. (1989), “Viscoelastic behavior of thermo-rheologically complex resin matrix composites,” Composites Science and Technology, Vol. 36, 351-365.

Sawant, S., Muliana A.H. (2008), “A thermo-mechanical viscoelastic analysis of orthotropic media,” Composite Structures, Vol. 83, 61-72.

Schapery, R.A. (1969), “On the characterization of nonlinear viscoelastic materials,” Polymer Engineering and Science, Vol. 9, No. 4, 295-310.

Schapery, R.A. (1969), “Thermal expansion coefficients of composite materials based on energy principles,” J. Composites Material, Vol. 2, No. 3, 380-404.

Schapery, R. A. (1997), “Nonlinear viscoelastic and viscoplastic constitutive equations based on thermodynamics,” Mechanics of Time-Dependent Materials, Vol. 1, 209.

Shan, Z., Gokhale, A.M. (2002), “Representative volume element for non-uniform microstructure,” Comp. Mat. Sci., Vol. 24, 361-379.

Simo, J.C., Hughes, T.J.R. (1998), “Computational inelasticity,” New York, Springer, Verlag.

Suquet, P (1985),”Local and global aspect in the mathematical theory of plasticity,” Plasticity today: modeling, methods, and application, 279-310.

Schwarz, F., Staverman, A.J. (1952), “Higher approximations of relaxation spectra,” Physica, Vol. 18, Issue 10, 791-798.

Tamrakar S., Lopez-Anido R.A., Kiziltas, A., Gardner D.J. (2011), “Time and temperature dependent response of a wood–polypropylene composite,” Composites part A: Applied Science and Manufacturing, Vol. 42, No. 7, 834-842.

Tuttle, M.E., Brinson, H.F. (1986), “Prediction of the long-term creep compliance of general composite laminates,” Experimental Mechanics, 89-102.

Tuttle, M.E., Pasricha, A., Emery, A.F. (1995), "The nonlinear viscoelastic-viscoplastic behavior of IM7/5260 composites subjected to cyclic loading," Journal of Composite Materials, Vol. 29, No. 15, 2025-2046.

Tuttle, M.E., Pasricha, A., Emery, A.F. (1993), "Time-temperature behavior of IM7/5260 composites subjected to cyclic loads and temperatures," ASME, Vol. 159, 343-357.

Valanis, K.C. (1971), "A theory of viscoplasticity without a yield surface. Part 1, general theory," Arch. Mech, Vol. 23, 517-533.

Varna, J., Akshantala, N.V., Talreja, R. (1997), "Stiffness changes in laminates caused by intralaminar cracks and shear deformation," ASME International Mechanical Engineering Congress, Dallas, TX, MD-Vol. 80, T.S. Srivatsan et al. (eds.), ASME, New York, 1997, 165-168.

Varna, J., Joffe, R., Akshantala, N.V., Talreja, R. (1999), "Damage in composite laminates with off-axis plies," Composites Science and Technology, Vol. 59, 2139-2147.

Voigt, W. (1887), "Theoretische studien über die elasticitätsverhältnisse der krystalle". Abh.Kgl.Ges.Wiss.Göttingen, Math.Kl, Vol. 34, 3-51.

Walpole, L.J. (1969), "On the overall elastic moduli of composite materials," J. Mech. Phys. Solids, Vol. 17, 235-251.

Wang, W.M., Sluys, W. J., de Borst, R. (1997), "Viscoplasticity for instabilities due to strain softening, strain-rate softening," Int. J. Numer. Meth. Eng, Vol. 40, 3839-3864.

Ward, I.M., Onat, E.T. (1963), "Nonlinear mechanical behavior of oriented polypropylene," J. of Mechanics and Physics of Solids, Vol. 11, 217-228.

Wineman, A.S., Rajagopal K.R. (2000), "Mechanical response of polymers: an introduction," London, Cambridge University Press.

Zapas, L.J., Crissman, J.M. (1984), "Creep and recovery behavior of ultra-high molecular weight polyethylene in the region of small uniaxial deformations," Polymer, Vol. 25, 57-62.

Zhang, Hartwig (1997), "Relation of damping and fatigue damage of unidirectional fiber composites," International Journal of Fatigue, Vol. 24, Issue 7, 713-718.

Zienkiewicz, O.C., Cormeau, I.C. (1972) "Viscoplasticity solution by finite element process," Arch. Mech, Vol. 25, 873-889.

Zienkiewicz, O.C., Cormeau, I.C. (1974) “Viscoplasticity–plasticity and creep in elastic solids: a unified numerical solution approach,” Int. J. Numer. Methods. Eng, Vol. 8, 821-845.